Time-of-Flight Secondary Ion Mass Spectrometry – Fundamental Issues for Quantitative Measurements and Multivariate Data Analysis

Joanna Lee

Michaelmas Term 2011

A thesis submitted for the degree of

Doctor in Philosophy at the University of Oxford

Time-of-Flight Secondary Ion Mass Spectrometry – Fundamental Issues for Quantitative Measurements and Multivariate Data Analysis

Joanna Lee, Trinity College.

A thesis submitted for the degree of Doctor of Philosophy at the University of Oxford

Michaelmas Term 2011

Abstract

Time-of-flight secondary ion mass spectrometry (ToF-SIMS) is a powerful technique for the analysis of organic surfaces and interfaces for many innovative technologies. However, despite recent developments, there are still many issues and challenges hindering the robust, validated use of ToF-SIMS for quantitative measurement. These include: the lack of metrology and fundamental understanding for the use of novel cluster primary ion beams such as C_{60}^{n+} and Ar_{2000}^{+}; the need for validated and robust measurement protocols for difficult samples, such as those with significant micron scale surface topography; the lack of guidance on novel data analysis methods including multivariate analysis which have the potential to simplify many time-consuming and intensive analyses in industry; and the need to establish best practice to improve the accuracy of measurements. This thesis describes research undertaken to address the above challenges. Sample topography and field effects were evaluated experimentally using model conducting and insulating fibres and compared with computer simulations to provide recommendation to diagnose and reduce the effects. Two popular multivariate methods, principal component analysis (PCA) and multivariate curve resolution (MCR), were explored using mixed organic systems consisting of a simple polymer blend and complex hair fibres treated with a multi-component formulation to evaluate different multivariate and data preprocessing methods for the optimal identification, localisation and quantification of the chemical components. Finally, cluster ion beams C_{60}^{n+} and $Ar_{500\text{-}2500}^{+}$ were evaluated on an inorganic surface and an organic delta layer reference material respectively to elucidate the fundamental metrology of cluster ion sputtering and pave the way for their use in organic depth profiling. These studies provide the essential metrological foundation to address frontier issues in surface and nanoanalysis and extend the measurement capabilities of ToF-SIMS.

Acknowledgments

I would like to thank the following people without whom the completion of this thesis would not have been possible. It is an honour for me to work with so many brilliant and distinguished colleagues in the Nanoanalysis Group at the National Physical Laboratory (NPL). First and foremost, I owe my deepest gratitude to Prof Ian Gilmore, my supervisor at NPL, for his steadfast encouragement, motivation, insight and guidance throughout my career. His tireless enthusiasm for the science, practical approach to research and a deep understanding of the industrial requirements have altogether kept my research strongly focused, and I would not have achieved everything without his leadership. I am particularly indebted to Dr Martin Seah for his unrivalled experience and intuition and his rigorous critique of the work. I am grateful to Dr Alex Shard for many valuable discussions and advice throughout my study, which are too numerous to mention. My sincere thanks are due to Dr Felicia Green, for being an inspiration and a role model for me.

I wish to express my gratitude for Prof Chris Grovenor, my supervisor at Oxford University, and Dr Adrian Taylor, the Director of Studies at Oxford Materials, for making my studentship possible. I gratefully acknowledge the funding for this work provided by the National Measurement System (NMS) of the UK Department of Business, Innovation and Skills (BIS) under the Chemical and Biological Metrology Programme. This work is also supported by the BIS Micro and Nano Technology programme. I am thankful to NPL for the generous sponsorship of my DPhil studentship.

Many colleagues at NPL have facilitated the research and it is my pleasure to thank them here. My gratitude goes to Steve Spencer for assisting with the preparation and mounting of fibre and wire samples, Dr Felicia Green for providing a detailed SIMION model of a reflectron instrument, Bob Clarke for helpful discussions on the behaviour of dielectrics in an AC field, Dr Jian Wang for help with COMSOL simulations, Dr Martin Seah for helpful discussions on Sigmund and Claussen's thermal spike model, Dr Charles Clifford for help with the AFM measurements, and Radleigh Foster and Dr Alex Shard for the preparation of the organic delta layer reference material.

This work greatly benefited from helpful discussions with external colleagues, including but not limited to Dr Ewald Niehuis and Dr Derk Rading (ION-TOF), Dr Scott Bryan (PHI), Prof Bonnie Tyler (University of West Indies), Dr Matt Wagner (Procter & Gamble), Prof Morgan Alexander (University of Nottingham) and all the participants of the 59th IUVSTA Workshop. I would like to thank Dr Ian Fletcher (Intertek, MSG) for provision of the hair fibre ToF-SIMS image, and Prof Martin Prutton (University of York) for the anisotropically etched silicon sample. I owe my deepest gratitude to my collaborators at Kyoto University, Prof Jiro Matsuo and Dr Satoshi Ninomiya, for their warm hospitality and generous support during my secondment to Kyoto.

Finally, I must take the opportunity to thank my mum, who is always supportive and generous and to whom I owe every success and achievement. My special gratitude is due to Mike. Without his patience and support, my thesis could not have been completed. Last but not least, I would like to thank my furry companions, whose loyalty, cheerfulness and warmth keeps me looking on the bright side.

Joanna Lee

October 2011

Preface

This thesis is an account of the work carried out by the author at the National Physical Laboratory, Teddington, between 2005 and 2010, under the supervision of Prof Ian Gilmore (National Physical Laboratory) and Prof Chris Grovenor (Department of Materials, University of Oxford). No part of this work has been previously submitted for a degree at this or any other university. The work of other authors has been freely drawn upon and is duly acknowledged in the text. A list of references has been given at the end of the thesis. The majority of the research presented in this thesis has been submitted or published as articles. A list of these appears below in chronological order.

"**Quantification and methodology issues in multivariate analysis of ToF-SIMS data for mixed organic systems**", J. L. S. Lee, I. S. Gilmore, and M. P. Seah, Surface and Interface Analysis **40,** 1 (2008).

"**Topography and field effects in the quantitative analysis of conductive surfaces using ToF-SIMS**", J. L. S. Lee, I. S. Gilmore, I. W. Fletcher, and M. P. Seah, Applied Surface Science **255,** 1560 (2008).

"**The application of multivariate data analysis techniques in surface analysis**", J. L. S. Lee, and I. S. Gilmore, in *Surface Analysis – The Principal Techniques*, 2nd ed., edited by J. C. Vickerman and I. S. Gilmore (Wiley, Chichester, 2008).

"**The development of standards and guides for multivariate analysis in surface chemical analysis**", J. L. S. Lee, B. J. Tyler, M. S. Wagner, I. S. Gilmore, and M. P. Seah, Surface and Interface Analysis **41,** 76 (2009).

"**Multivariate image analysis strategies for ToF-SIMS images with topography**", J. L. S. Lee, I. S. Gilmore, I. W. Fletcher, and M. P. Seah, Surface and Interface Analysis **41,** 653 (2009).

"**Organic depth profiling of a nanostructured delta layer reference material using large Argon cluster ions**", J. L. S. Lee, S. Ninomiya, J. Matsuo, I. S. Gilmore, M. P. Seah, and A. G. Shard, Analytical Chemistry **82,** 98 (2010).

"**Topography and field effects in secondary ion mass spectrometry – Part I: Conducting samples**", J. L. S. Lee, I. S. Gilmore, M. P. Seah, and I. W. Fletcher, Journal of the American Society for Mass Spectrometry **22,** 1718 (2011).

"**Topography and field effects in secondary ion mass spectrometry – Part II: Insulating samples**", J. L. S. Lee, I. S. Gilmore, M. P. Seah, A. P. Levick, and A. G. Shard, Surface and Interface Analysis **44**, 238 (2012).

The majority of the research presented in this thesis has also previously been presented at national and international conferences, and a list of these appears below in chronological order.

5th European Workshop on Secondary Ion Mass Spectrometry, Muenster, Germany, Sept 2006, Tutorial, "A guide to the practical use of Chemometrics – with applications for Static SIMS", and Poster Presentation, "Identification and quantification of ToF-SIMS images using multivariate analysis"

Nano-Molecular Analysis for Emerging Technologies II, Teddington, UK, Oct 2006, Oral Presentation, "Identification and Quantification of ToF-SIMS Images using Multivariate Analysis"

UK Surface Analysis Forum Winter Meeting 2006, Newcastle, UK, Jan 2007, Tutorial, "A guide to the practical use of Chemometrics – with applications for Static SIMS"

American Vacuum Society 54th International Symposium, Seattle, USA, Oct 2007, Oral Presentation, "Topography and field effects in the quantitative analysis of conductive surfaces using ToF-SIMS"

16th International Conference on Secondary Ion Mass Spectrometry, Kanazawa, Japan, Nov 2007, Oral Presentation, "Topography and field effects in the quantitative analysis of conductive surfaces using ToF-SIMS"

UK Surface Analysis Forum Summer Meeting 2008, Belfast, Northern Ireland, Jul 2008, Poster Presentation, "Topography effects in the quantitative analysis of surfaces using SIMS"

Micro and Nano Scale Characterisation of Fibres, Belfast, Northern Ireland, Jul 2008, Oral Presentation, "Topography Effects in the Analysis of Insulating Microfibres using SIMS"

6th European Workshop on Secondary Ion Mass Spectrometry, Muenster, Germany, Sept 2008, Tutorial, "A guide to the practical use of Chemometrics – with applications for Static SIMS", Oral Presentation, "Topography Effects in the Quantitative Analysis of Surfaces using SIMS", and Poster Presentation, "Multivariate Image Analysis Strategies for ToF-SIMS Images Topography"

American Vacuum Society 55th International Symposium, Boston, USA, Oct 2008, Oral Presentation, "Multivariate image analysis strategies for ToF-SIMS images with topography"

17th International Conference on Secondary Ion Mass Spectrometry, Toronto, Canada, Sept 2009, Oral Presentation, "Organic depth profiling of a nanostructured delta layer reference material using large argon cluster ions: a preliminary study"

59th IUVSTA Workshop on Surface Chemical Analysis – Improving Data Interpretation by Multivariate and Informatics Techniques, Trinidad, Trinidad and Tobago, Apr 2010, Oral Presentation, "Chemometrics in ToF-SIMS: Benefits and Potential Pitfalls"

22nd Annual Workshop on SIMS, Norfolk, Virginia, USA, May 2010, Oral Presentation, "Organic Depth Profiling of a Nanostructured Delta Layer Reference Material – A Comparison of $Ar_{500\text{-}1000}^{+}$ and C_{60}^{n+}" and Oral Presentation, "VAMAS Interlaboratory Study on SIMS – (1) Linearity of the Intensity Scale (2) Organic Depth Profiling"

7th European Workshop on Secondary Ion Mass Spectrometry, Muenster, Germany, Sept 2010, Tutorial, "A guide to the practical use of Chemometrics – with applications for Static SIMS"

UK Surface Analysis Forum Winter Meeting 2011, Teddington, UK Jan 2011, Oral Presentation, "Advances in Organic Depth Profiling and 3D Imaging SIMS"

Abbreviations

AFM	Atomic force microscopy
ALS	Alternating least squares
ANN	Artificial neural networks
BIS	Department of Business, Innovation and Skills
DC	Direct current
DFA	Discriminant function analysis
DSO	DataSet standard data object
FNNLS	Fast non-negative least squares
FWHM	Full width half maximum
HCA	Hierarchical cluster analysis
ISO	International Organization for Standardization
LMIG	Liquid metal ion gun
MAF	Maximum autocorrelation factors
MALDI	Matrix assisted laser desorption ionisation mass spectrometry
MCP	Microchannel plate
MCR	Multivariate curve resolution
MD	Molecular dynamics
MSD	Molecular signal dose
NMS	National Measurement System
NPL	National Physical Laboratory
OLED	Organic light emitting diode
OPV	Organic photovoltaics
PC	Polycarbonate
PCA	Principal component analysis
PCR	Principal component regression
PDMS	Poly(dimethylsiloxane)
PEMA	Poly(ethyl methacrylate)
PET	Poly(ethylene terephthalate)
PLA	Polylactide

PLS	Partial least squares regression
PMMA	Poly(methyl methacrylate)
PTFE	Poly(tetrafluoroethylene)
PVC	Poly(vinyl chloride)
QCM	Quartz crystal microbalance
SDTF	ISO standard data transfer format
SEM	Scanning electron microscopy
SIMS	Secondary ion mass spectrometry
SNMS	Secondary neutral mass spectrometry
TOF	Time of flight
UHV	Ultra-high-vacuum
XPS	X-Ray photoelectron spectroscopy

Contents

Chapter 3 – Topography and field effects in SIMS: Insulating samples

Chapter 4 – Introduction to multivariate data analysis

Chapter 1 – Introduction

1.1 Surfaces and interfaces for industry

Time-of-flight secondary ion mass spectrometry (ToF-SIMS) is a popular surface analytical technique for characterisation and problem solving in a wide range of industries whose products are reliant on surface and interfacial chemical properties.[1] Examples include semiconductors and electronics, lacquers and paints, catalysts, medical devices, paper, pharmaceuticals, packaging and high performance coatings. For many of these products, the product performance is driven strongly by surface and interfacial chemistry, which is crucially related to important physical properties including wettability, adhesion, interaction with the external environment and product lifetime. Measurements of the surface or interfacial chemistry can aid product development, process optimisation, failure analysis and quality control in these industries, providing key input to product innovation and enhancing product competitiveness. There continues to be a strong growth in the use of organic materials in industry, including complex molecules and polymers. There are numerous products where organic surfaces and interfaces are of importance. Three examples are given below.

- *Medical devices and drug delivery systems*. For example, drug-eluting coronary stents, inserted into arteries during angioplasty, are coated with a drug polymer matrix layer. The drug is released over a period of time and reduces instances of the artery reblocking. A detailed understanding of the surface and interfacial chemistry of the drug coating and the accurate, three-dimensional localisation of the drug molecules within the coating is absolutely essential in developing high performance stents that will deliver a steady dose over the required period of time. The surface chemistries of medical devices are crucial in determining their biocompatibility and lifetime, for example affecting cell adhesion properties and biofilm formation.

- *Home and personal care products*. The development of new formulations in the personal care industry for hair and laundry applications requires good understanding of surface chemistry. The technologies behind such products are fast changing, challenging and increasingly reliant on microscale surface properties of fibres. Measurements of surface chemistry at the microscale can aid the understanding of chemical mechanisms that influence product performance. For example, hair conditioners modify the surface friction of hairs as they slide against each other. Measurements and understanding of the adsorption behaviour of active conditioning ingredients will lead to the production of more efficient and environmentally friendly products.

- *Organic electronics*. Driven by the development of conducting and semiconducting polymers and molecules, organic electronics such as organic photovoltaics (OPV) and organic LEDs (OLEDs) have the potential to revolutionise the electronics industry due to the potential for low cost fabrication, low power operation and increased efficiency. These devices rely on fabricating thin, nano-structured organic films. A major concern is the performance, lifetime and efficiency of these devices, which depends critically on the nanoscale chemistry of interfaces. Chemical analyses are important to diagnose compositional changes, phase separation, intermixing, migration, degradation, and to identify, localise and quantify contaminants.

The robust measurement of surface and interfacial chemistry is key to these complex technologies and developments in measurement techniques are urgently needed, with the requirement to achieve more chemical information or even full chemical structure at ever improving spatial and depth resolutions.

1.2 Requirements for surface analysis

The importance of surface and interfaces arises from the fact that surface and interfacial atoms are responsible for the interaction between different materials and with the external environment. Analysis of surfaces present unique challenges as the number of surface atoms

is extremely limited compared to the number of atoms in the bulk. For example, a typical silicon (100) wafer measuring 1 cm × 1 cm × 1 mm would contain 5×10^{21} silicon atoms in total, with fewer than 2×10^{15} atoms, or 0.00025%, on the surface. The challenges of surface analysis are exacerbated for organic materials. Two effects restrict the signal availability for organic surfaces. Firstly, the number of intact organic entities (e.g. organic molecules) on the outermost surface is comparatively lower because of their large size. This problem is especially acute if analyses are required at high spatial resolution. Secondly, organic materials are prone to damage during analysis. Surface analysis therefore requires a shallow information depth for ultimate surface sensitivity, an analytical probe that causes low chemical damage and extremely sensitive detection techniques.

1.3 Time-of-flight secondary ion mass spectrometry

Time-of-flight secondary ion mass spectrometry (ToF-SIMS) is a powerful and widely used technique for surface chemical analysis.[1] ToF-SIMS is useful for the identification of trace elements, organic molecules and polymers on surfaces, with better than 1 ppm sensitivity for some molecules and down to ppb sensitivity for some elements. ToF-SIMS is extremely surface sensitive, with information only coming from the top nanometres of the sample in static SIMS mode. Current instrumentation is capable of imaging with an ultimate imaging resolution of around 200 nm for organic species. When combined with cluster ion sputtering, ToF-SIMS is capable of obtaining 3-dimensional elemental or molecular information with best depth resolution of around 10 nm.

1.3.1 Principles of sputtering

In ToF-SIMS, the sample surface is bombarded by an energetic primary ion beam in an ultra-high-vacuum (UHV) environment. This desorbs surface species through a physical process called sputtering. A small fraction (typically 10^{-2} to 10^{-4}) of the desorbed species are ionised. They are referred to as secondary ions and are extracted via the application of an extraction

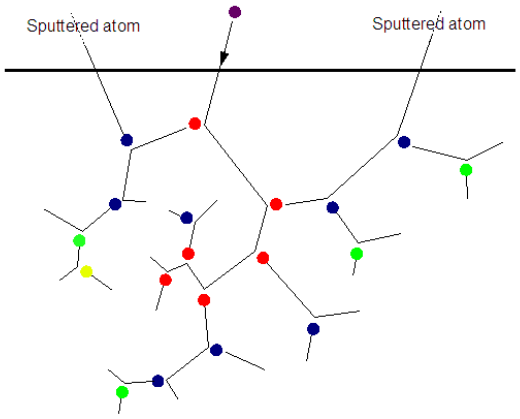

Figure 1.1 Schematic diagram of a linear collision cascade, reproduced with permission from http://upload.wikimedia.org/wikipedia/commons/9/91/Linearcollisioncascadesput.png (2011).

voltage and analysed in a time-of-flight mass spectrometer. The mass spectra show the elements, molecules and molecular fragments on the surface, and reflect the surface chemistry of the sample.

When an energetic ion hits a surface, it starts a collision cascade. A schematic diagram of a collision cascade is shown in Figure 1.1. The term 'cascade' refers to multiple quasi-elastic collisions in the target sample induced by the bombarding ions. In a simple collision cascade, the momentum exchange between the ions and atoms in the material results in a small fraction of surface atoms acquiring momentum in a direction away from the bulk. If the transferred energy is greater than the surface binding energy of the material, then the atoms can be ejected from the surface i.e. sputtered.

SIMS traditionally employs atomic primary ions such as Ga^+, Ar^+, Cs^+, and Au^+, with the impact energy range of around 0.5 – 30 keV. In this regime, the sputtering events can be successfully characterised by the linear cascade theory of Sigmund.[2-4] The linear cascade theory assumes a low density of moving atoms in the target and each recoil collides only with target atoms at rest. From this theory, the sputtering yield (the number of sputtered atoms per incident ion) can be calculated using the total energy deposited near the surface, the number

of low-energy recoil atoms in the target, the fraction of these recoil atoms that come to the surface, and the fraction that have sufficient energy to overcome surface binding forces. Since typically only atoms nearest to the surface can escape the bulk, sputtering in the linear cascade regime results in the ultrahigh surface sensitivity seen in ToF-SIMS.

Over the last decade, there has been a significant move towards using cluster ions, such as Bi_n^+, Au_n^+, SF_5^+, C_{60}^{n+}, as primary projectiles in SIMS. Cluster primary ions are associated with massive enhancements in the sputter yield beyond what is expected from Sigmund's linear cascade theory. This means the sputtering yield of cluster ion X_n, consisting of n atoms of X impacting a target with energy E, is significantly higher than n times the sputtering yield of X each with a fraction of the total impact energy of E / n. In many cases, the enhancements in the yield can be as much as two orders of magnitude.[5-8] This enhancement arises from higher energy densities deposited in the near surface region and the overlap of the collision cascades generated by individual constituent atoms of the cluster primary ion. This forms a dense collision cascade that does not satisfy the assumptions for linear cascade theory.

A molecular dynamics simulation of a cluster ion impact is shown in Figure 1.2, reproduced from Postawa *et al*.[9] Whilst the mechanism for cluster ion sputtering is not yet precisely understood, the general consensus is that atomic primary ions, such as Ga^+, implant deep into the target causing substantial sub-surface damage (i.e. displaced atoms), whilst only a small amount of material is sputtered. SIMS analyses by atomic primary ions are therefore limited by ion induced damage and restricted to the conventional static limit (of ~ 10^{16} ions/m^2). On the other hand, cluster primary ions, such as C_{60}^{n+}, deposit their energy closer to the surface and form a large impact crater from where a significant amount of material is sputtered. Importantly, C_{60}^{n+} causes less damage and displacements to the sub-surface layers and the volume of displaced materials is comparable to the sputtering yield. This allows the sputter removal of the material layer-by-layer without extensive build up of damage or mixing.[10,11] Compositional depth profiles can therefore be obtained under prolonged C_{60}^{n+} bombardment, even for delicate organic materials, and this has provided a major step change in the analytical capability of SIMS.

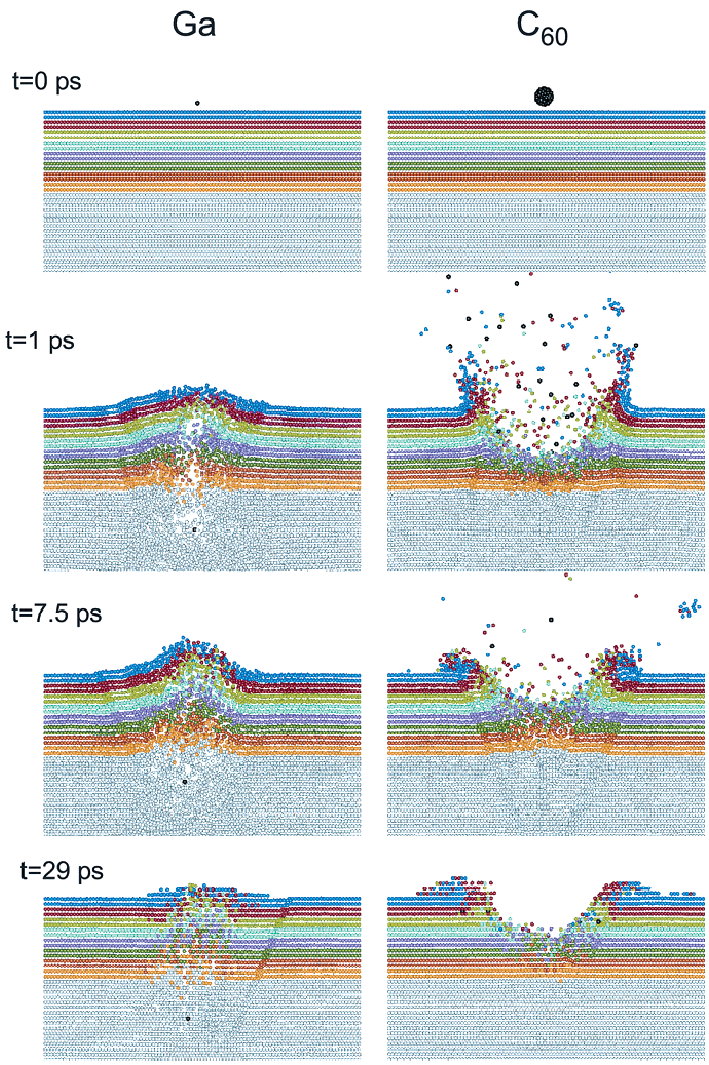

Figure 1.2 A cross-sectional view of the temporal evolution of a typical collision cascade in an Ag (1 1 1) surface due to 15 keV Ga and C_{60}^{n+} bombardment at normal incidence. Reproduced with permission from Reference 9. Copyright 2004 American Chemical Society.

1.3.2 Instrumentation

Figure 1.3 shows a schematic diagram of a typical ToF-SIMS instrument, of the pulsed primary ion beam and single stage reflectron analyser design.[12] Typically, the primary ion beam is accelerated by around 20 – 30 kV, pulsed with a typical pulse width of 25 ns and then further bunched so that it arrives at the sample within ~ 1 ns. The primary ion pulse contains several hundred primary ions which sputter secondary ions from the sample. The primary

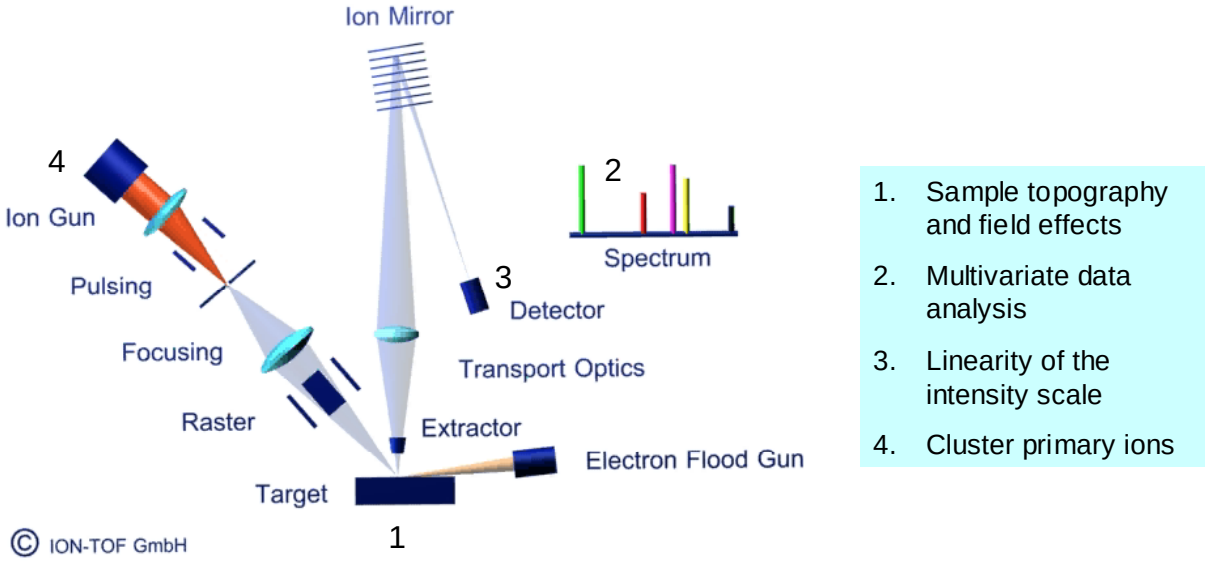

Figure 1.3 Schematic diagram of the ION-ToF ToF-SIMS IV mass spectrometer, provided by ION-TOF GmbH (Muenster, Germany). Four major aspects of the technique are explored in this thesis and these are labelled 1 – 4 on the diagram.

ion pulse provides a reference for $t = 0$ for the time-of-flight measurement of the secondary ions. The secondary ions are extracted into the time-of-flight mass analyser via the application of an extraction voltage (typically –2000 V for positive secondary ions and +2000 V for negative secondary ions). The extraction voltage determines the energy of the secondary ions as they drift through the analyser along a flight path which is roughly 2 m in length. Secondary ions are separated by their mass since heavier ions have lower velocity than lighter ions with the same kinetic energy. Some distance into the flight path, the secondary ions are reflected by an ion mirror which provides first order energy compensation. Since secondary ions are typically emitted with a small spread of kinetic energies of several eV,[13,14] the reflectron analyser provides improved time-focus at the detector for different ions of the same species. At the end of the flight path, the secondary ions are detected by a single ion counting detector, consisting of a microchannel plate (MCP) detector coupled to time-to-digital convertor (TDC) electronics. The spectrum obtained with each primary ion pulse is collected and summed over many pulses (typically 10^5 – 10^7). Finally, the spectrum is converted from a

'time-of-flight' scale into a mass scale via mass calibration using a number of known secondary ions.[15] For insulating samples, charge compensation is necessary using an electron flood gun during analysis. This delivers low energy (~ 20 eV) electrons to the sample surface to neutralise any charging by the positive primary ion beam.

ToF-SIMS is a highly versatile technique capable of generating mass spectra, images and depth profiles of the sample.[16] ToF-SIMS images are obtained by rastering the primary ion beam across the sample and collecting a mass spectrum at each pixel. The resulting image resolution depends on the primary ion beam focus and as well as the availability of signal. Using a liquid metal ion gun (LMIG), a typical focus of 3 – 5 μm is readily achievable with a bunched pulse width of 1 ns in high mass resolution mode, but the beam focus can be improved to around 100 nm by utilising longer primary ion pulses and compromising on the mass resolution of the spectrum.[16] For organic materials, the availability of molecular signal, rather than beam focus, is a major limitation to the ultimate spatial resolution achievable.[17,18,19] ToF-SIMS depth profiles are obtained by alternating mass spectrometry or imaging using a pulsed LMIG primary ion beam with the sputter removal of the sample layer-by-layer using a cluster ion beam such as C_{60}^{n+}. This allows chemical species to be analysed as a function of sputter depth. This 'dual beam' approach has the advantage of combining the high imaging resolution of the LMIG with the high sputtering rate and low damage of C_{60}^{n+}.[20] The caveat is that the ion dose delivered by the LMIG must be at least two orders of magnitude lower than the dose of C_{60}^{n+}, to ensure that C_{60}^{n+} is able to sputter away any damage to the organic samples caused by the LMIG.[21,22]

Currently, pulsed primary ion beam ToF-SIMS instruments, such as the one illustrated in Figure 1.3 and described above, are the most common instrument design. Recently, an alternative design utilising a DC cluster primary ion beam and pulsed analyser have become available.[23] This new instrument design is specifically optimised for organic depth profiling. By collecting and analysing all secondary ions sputtered by the DC cluster primary ion beam,

made possible by decoupling the sputtering event from the secondary ion time-of-flight measurement, improved sensitivities may be achieved in organic depth profiles.

Figure 1.3 also marks four major aspects of the technique which are explored in this thesis. These will be discussed in the subsequent sections.

1.4 Recent developments and challenges

ToF-SIMS have been in continual development since the early work of Professor Alfred Benninghoven's group at the University of Münster in the 1980s.[24,25] From its early applications to the surface mass spectrometry of simple organic and polymer surfaces,[26,27] ToF-SIMS has evolved into a hugely powerful technique for the analysis of complex organic and biological structures.[28,29] Figure 1.4 summarises some of these developments for the analysis of organic samples since 1990. In the last decade, the development of the technique and applications has been largely driven by advances in ion beam technologies, shown in blue on the figure. Whilst ToF-SIMS has been used for imaging since its early days,[30] the advent of small cluster primary ions such as Au_3^+ and Bi_3^+ led to an explosion in *molecular* imaging due to the orders-of-magnitude increase in molecular secondary ion yields using metal cluster primary ions compared to their atomic counterparts or Ga^+.[6] The introduction of SF_5^+, C_{60}^{n+} and the recent argon cluster primary ion beams opens up new capabilities in molecular depth profiling.[31-33] As a result, 3D organic analyses are not only possible but are fast becoming routine. The increase in imaging and 3D depth profiling analyses (shown in green on Figure 1.4) is also fuelled by the strong growth in computing and data storage capabilities which allows the raw data, consisting of a full ToF-SIMS mass spectrum at every pixel and sputter time, to be recorded and retrospective analysis of the data to be carried out efficiently. These developments are timely as they coincide with the requirement to study ever more complex organic samples, from organic multilayers (e.g. packaging) to organic devices (e.g. organic electronics or drug delivery systems) and biological systems (e.g. cells or tissues), shown in pink on Figure 1.4.

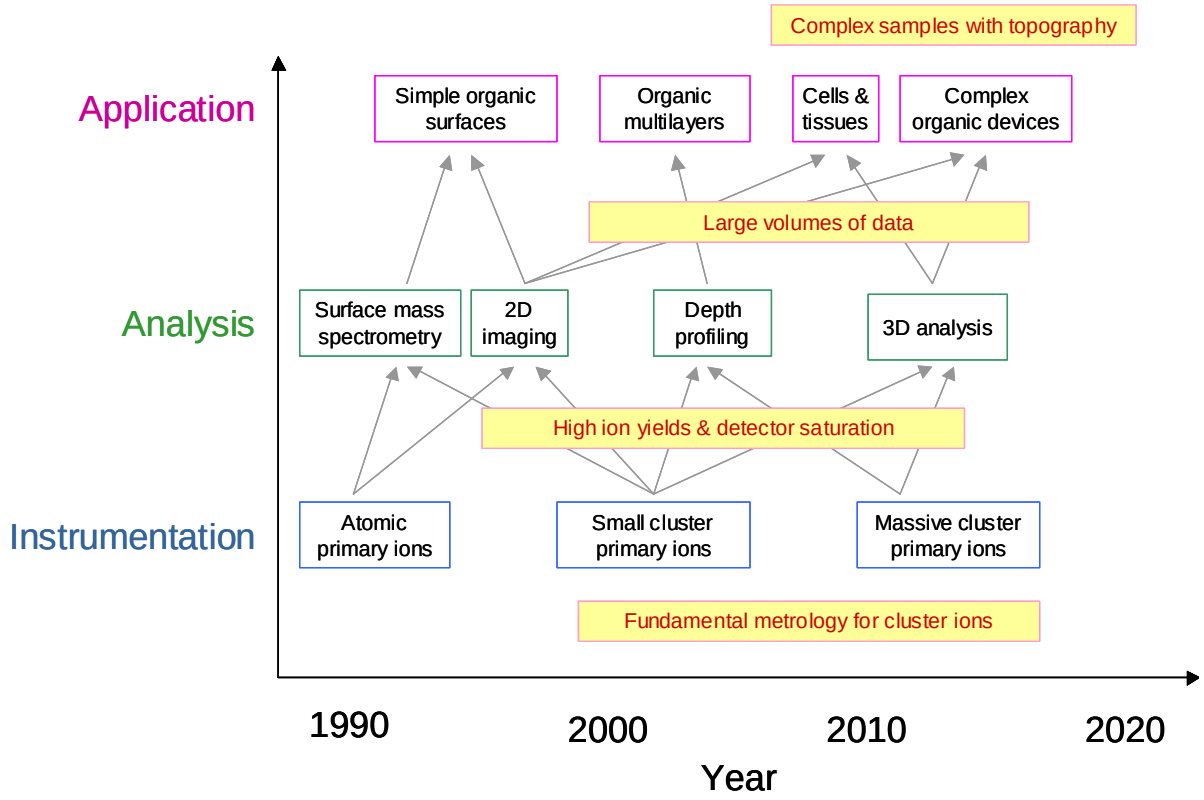

Figure 1.4 A diagram illustrating the development of time-of-flight secondary ion mass spectrometry for organic samples since 1990. Developments in the instrumentation (blue) led to new types of analyses (green) and applications (pink), which in turn result in new analytical challenges (yellow boxes).

The developments outlined above lead to significant new challenges for ToF-SIMS analyses, some of which are highlighted in the yellow boxes on Figure 1.4. These include,

- *Fundamental metrology for cluster ions*, required for the optimum use and future development of novel cluster ion primary beams such as C_{60}^{n+} and large argon clusters $Ar_{500-2500}^{+}$;

- *High ion yields and detector saturation*, caused by the enhanced secondary ion yields for cluster primary ions as well as increased beam current achievable with modern ion guns;

- *Large volumes of data* generated by ToF-SIMS imaging and 3D depth profiling, which necessitates new methodologies for data analysis beyond the traditional 'stare-and-compare' approach;

- *Complex samples with topography*, especially for samples relevant to industry and emerging technologies such as the fibres, particles, microfabricated devices such as microfluidics and organic electronics.

In the growing field of organic SIMS, the above list of developments and challenges is, of course, far from exhaustive. Significant efforts are currently underway to improve ionisation efficiencies, for example using water vapour injection,[34] water soft landing,[35] matrix enhancement[36] and metal-assisted SIMS;[37] to understand fragmentation of organic and biomolecules;[38,39] to develop novel instrumentation, including new mass spectrometers,[23] high brightness large cluster sources[40,41] and event-by-event detection;[42] to explore new applications from organic photovoltaics, nanoparticle analysis to biomaterials discovery;[43-45] and to compare SIMS with other bio- and nano-analytical methods such as ambient mass spectrometries and MALDI.[46-48] These efforts are complemented by the development of the metrology base for SIMS to ensure robust and validated measurements, via a series of interlaboratory studies leading to international standards on repeatability, constancy and accurate mass calibration.[49]

1.5 Overview of the thesis

This research project aims to address growing measurement requirements in industry by tackling the analytical challenges for ToF-SIMS discussed above. The objectives are to provide the essential metrological foundation to address frontier issues in surface and nano-analysis and extend the measurement capabilities of ToF-SIMS. The research section of the thesis is divided into seven chapters which are organised around three themes covering the aspects labelled on Figure 1.3. Each chapter forms a self-contained study with separate introduction, conclusion and references. An outline of the thesis is provided below.

1. *Sample topography and field effects*

   In Chapter 2 and Chapter 3, a systematic study is made of the effects of surface topography and the resulting field effects in ToF-SIMS, combining an experimental

approach using simple model systems with computer simulations. This aims to understand and quantify the key factors that give rise to unwanted topographical artefacts in ToF-SIMS images, and provide guidance to analysts to diagnose, identify and minimise topographic effects in practical analysis. Chapter 2 covers the analysis of conducting samples, using gold wires mounted onto silicon wafers as a model system. Improvements are demonstrated on an anisotropically etched silicon device. Chapter 3 covers the analysis of insulating samples, using poly(ethylene terephthalate) (PET) fibres as a model system. In particular, the influence of topography on effective charge compensation is investigated.

2. *Multivariate data analysis*

Chapter 4 to Chapter 6 deal with multivariate analysis, which tackles the large volumes of data generated in ToF-SIMS by using statistical techniques to aid quantification and identification. In Chapter 4, an overview is given of multivariate analysis followed by the theory and concepts behind two popular methods, principal component analysis (PCA) and multivariate curve resolution (MCR). In Chapter 5, a ToF-SIMS image of a simple immiscible polymer blend is used to evaluate PCA and MCR for the accurate identification, localisation and quantification of the phase-separated polymer domains. This highlights significant issues, including the discrimination of chemical features from noise, the resolution of weak chemical contributions and the potential bias introduced by data preprocessing. In Chapter 6, the study is extended to a complex real-life sample from industry, consisting of hair fibres pre-treated with a multi-component formulation. This is challenging because of extreme topography, detector non-linearity and a large number of unknown chemical components. Recommendations are presented for the optimum use of multivariate analysis by analysts, and guidance is provided to select the most appropriate multivariate method and data preprocessing.

3. *Cluster primary ions*

   Chapter 7 and Chapter 8 cover two fundamental studies on cluster ion sputtering. In Chapter 7, the basic issues of C_{60}^{n+} sputtering are explored using inorganic samples. Sputtering yields are measured as a function of impact energy, and the importance of carbon deposition at low energies, carbon implantation and unusual sputter induced topography are investigated. In Chapter 8, the potential of organic depth profiling using novel argon cluster ions Ar_{500}^{+} to Ar_{1000}^{+} are explored using an organic delta layer reference sample. This shows superior performance over C_{60}^{n+}, including a constant and high sputtering yield, an extremely low sputter induced roughness and the potential to achieve high depth resolution. The results indicate that argon cluster ions will have a major role to play in the depth profiling of organic materials.

Finally, in Chapter 9, a critical evaluation is given on the benefits and limitations of the approaches taken in this study. Suggestions are given for future work that will further address the challenges and extend the measurement capabilities of ToF-SIMS.

References

1 J. C. Vickerman and D. Briggs, *ToF-SIMS Surface Analysis by Mass Spectrometry* (IM Publications & Surface Spectra, Manchester, 2001).

2 P. Sigmund, Physical Review **184,** 383 (1969).

3 M. P. Seah, C. A. Clifford, F. M. Green, and I. S. Gilmore, Surface and Interface Analysis **37,** 444 (2005).

4 M. P. Seah, Nuclear Instruments & Methods in Physics Research Section B-Beam Interactions with Materials and Atoms **229,** 348 (2005).

5 D. Weibel, S. Wong, N. Lockyer, P. Blenkinsopp, R. Hill, and J. C. Vickerman, Analytical Chemistry **75,** 1754 (2003).

6 R. Kersting, B. Hagenhoff, F. Kollmer, R. Mollers, and E. Niehuis, Applied Surface Science **231,** 261 (2004).

7 S. Bouneau, A. Brunelle, S. Della-Negra, J. Depauw, D. Jacquet, Y. Le Beyec, M. Pautrat, M. Fallavier, J. C. Poizat, and H. H. Andersen, Physical Review B **65,** 144106 (2002).

8 A. V. Samartsev, A. Duvenbeck, and A. Wucher, Physical Review B **72,** 115417 (2005).

9 Z. Postawa, B. Czerwinski, M. Szewczyk, E. J. Smiley, N. Winograd, and B. J. Garrison, The Journal of Physical Chemistry B **108,** 7831 (2004).

10 J. Cheng, A. Wucher, and N. Winograd, Journal of Physical Chemistry B **110,** 8329 (2006).

11 A. G. Shard, F. M. Green, P. J. Brewer, M. P. Seah, and I. S. Gilmore, Journal of Physical Chemistry B **112,** 2596 (2008).

12 J. Schwieters, H. G. Cramer, T. Heller, U. Jurgens, E. Niehuis, J. Zehnpfenning, and A. Benninghoven, Journal of Vacuum Science & Technology a-Vacuum Surfaces and Films **9,** 2864 (1991).

13 A. Delcorte and P. Bertrand, Surface Science **412-413,** 97 (1998).

14 A. Delcorte, C. Poleunis, and P. Bertrand, Applied Surface Science **252,** 6542 (2006).

15 F. M. Green, I. S. Gilmore, and M. P. Seah, Journal of the American Society for Mass Spectrometry **17,** 514 (2006).

16 R. N. S. Sodhi, Analyst **129,** 483 (2004).

17 B. Hagenhoff, Mikrochimica Acta **132,** 259 (2000).

18 F. Kollmer, Applied Surface Science **231,** 153 (2004).

19 T. L. Salter, J. L. S. Lee, I. S. Gilmore, M. P. Seah, and A. G. Shard, presented at 17th International Conference on Secondary Ion Mass Spectrometry, Toronto, Canada (2009)

20 K. Iltgen, C. Bendel, A. Benninghoven, and E. Niehuis, Journal of Vacuum Science & Technology A: Vacuum, Surfaces, and Films **15,** 460 (1997).

21 C. Szakal, S. M. Hues, J. Bennett, and G. Gillen, The Journal of Physical Chemistry C **114,** 5338 (2009).

22 J. Brison, S. Muramoto, and D. G. Castner, The Journal of Physical Chemistry C **114,** 5565 (2010).

23 J. S. Fletcher, S. Rabbani, A. Henderson, P. Blenkinsopp, S. P. Thompson, N. P. Lockyer, and J. C. Vickerman, Analytical Chemistry **80,** 9058 (2008).

24 P. Steffens, E. Niehuis, T. Friese, D. Greifendorf, and A. Benninghoven, Journal of Vacuum Science & Technology A: Vacuum, Surfaces, and Films **3,** 1322 (1985).

25 A. Benninghoven, Surface and Interface Analysis **43,** 2 (2011).

26 D. Briggs, British Polymer Journal **21,** 3 (1989).

27 M. C. Davies and R. A. P. Lynn, Clinical Materials **5,** 97 (1990).

28 G. Gillen, A. Fahey, M. Wagner, and C. Mahoney, Applied Surface Science **252,** 6537 (2006).

29 D. Breitenstein, C. E. Rommel, R. Mollers, J. Wegener, and B. Hagenhoff, Angewandte Chemie-International Edition **46,** 5332 (2007).

30 D. Briggs and M. J. Hearn, Surface and Interface Analysis **13,** 181 (1988).

31 G. Gillen, D. S. Simons, and P. Williams, Analytical Chemistry **62,** 2122 (1990).

32 C. Szakal, S. Sun, A. Wucher, and N. Winograd, Applied Surface Science **231,** 183 (2004).

33 S. Ninomiya, K. Ichiki, H. Yamada, Y. Nakata, T. Seki, T. Aoki, and J. Matsuo, Rapid Communications in Mass Spectrometry **23,** 1601 (2009).

34 T. Mouhib, A. Delcorte, C. Poleunis, and P. Bertrand, Journal of the American Society for Mass Spectrometry **21,** 2005 (2010).

35 G. Li, J. Cyriac, L. Gao, and R. Graham Cooks, Surface and Interface Analysis **43,** 498 (2011).

36 J. J. D. Fitzgerald, P. Kunnath, and A. V. Walker, Analytical Chemistry **82,** 4413 (2010).

37 O. Restrepo, A. Prabhakaran, K. Hamraoui, N. Wehbe, S. Yunus, P. Bertrand, and A. Delcorte, Surface and Interface Analysis **42,** 1030 (2010).

38 F. M. Green, E. J. Dell, I. S. Gilmore, and M. P. Seah, International Journal of Mass Spectrometry **272,** 38 (2008).

39 M. P. Seah, F. V. Green, and I. S. Gilmore, Journal of Physical Chemistry C **114,** 5351 (2010).

40 C. Guillermier, S. Della Negra, R. D. Rickman, V. Pinnick, and E. A. Schweikert, Applied Surface Science **252,** 6529 (2006).

41 Y. Fujiwara, N. Saito, H. Nonaka, T. Nakanaga, and S. Ichimura, Nuclear Instruments & Methods in Physics Research Section B-Beam Interactions with Materials and Atoms **268,** 1938 (2010).

42 V. Pinnick, S. Rajagopalachary, S. V. Verkhoturov, L. Kaledin, and E. A. Schweikert, Analytical Chemistry **80,** 9052 (2008).

43 B.-Y. Yu, C.-H. Kuo, W.-B. Wang, G.-J. Yen, S.-i. Iida, S.-Z. Chen, W.-C. Lin, S.-H. Lee, W.-L. Kao, C.-Y. Liu, H.-Y. Chang, Y.-W. You, C.-J. Chang, C.-P. Liu, J.-H. Jou, and J.-J. Shyue, Analyst **136,** 716 (2011).

44 D. Baer, D. Gaspar, P. Nachimuthu, S. Techane, and D. Castner, Analytical and Bioanalytical Chemistry **396,** 983 (2010).

45 A. L. Hook, D. G. Anderson, R. Langer, P. Williams, M. C. Davies, and M. R. Alexander, Biomaterials **31,** 187 (2010).

46 L. A. McDonnell and R. M. A. Heeren, Mass Spectrometry Reviews **26,** 606 (2007).

47 J. C. Vickerman, Analyst **136,** 2199 (2011).

48 T. L. Salter, F. M. Green, I. S. Gilmore, M. P. Seah, and P. Stokes, Surface and Interface Analysis **43,** 294 (2011).

49 I. S. Gilmore, Journal of Surface Analysis **14,** 376 (2008).

Chapter 2 – Topography and field effects in SIMS: Conducting samples

2.1 Introduction

Many technological devices possess significant surface topography, including microfluidic systems, MEMS, composite materials, catalysts, electronics, sensors and biomedical devices. The functionality and activity of these components is often critically dependent on their nanoscale surface chemistry and molecular interactions, and considerable effort is made to study and characterise them. An example is the analysis of microfluidic channels for wetting and other properties. Secondary ion mass spectrometry (SIMS) is a promising technique for the study of surfaces due to its chemical sensitivity and specificity. However, significant topographic features in the scale of tens or even hundreds of microns are commonly encountered on these samples. This can cause many unwanted artefacts in SIMS spectra and images,[1-4] which significantly hinder data interpretation and quantification. As a result, chemical characterisation of surfaces with microscale topography remains a significant challenge due to the lack of systematic and validated measurement methods.

The analysis of topographic sample is different to the analysis of flat uniform surfaces in many aspects and these are discussed in detail in this chapter. These issues broadly fall into four categories:

1. Practical issues: Appropriate sample mounting for topographic samples is essential to minimise field effects, to optimise the sample surface potential (for insulating samples) or to reduce sample charging.[5]

2. Simple geometry effects: Due to the difference in the angle of the primary ion beam and the analyser with respect to the sample, the image coordinates can be distorted,

and geometrical shadowing can occur when an area of the sample is not accessible to the primary ion beam.

3. Sputtering behaviour: Many sputtering parameters are a function of the primary ion incidence angle, which varies across samples with topography. This includes sputtering yields[6] and the energy and angular distribution of emitted secondary ions.[7,8] For organic samples, changes to the spectra such as the relative intensity of organic fragments have been observed at different incidence angles.[1]

4. Instrumental response: This arises from the extraction and mass analysis of secondary ions from a sample with topography. For example, secondary ions entering the analyser at large angles may be lost because of limited analyser acceptance. For instruments with pulsed primary ions, the time-of-flight for secondary ions originating from different heights or positions may be shifted, leading to poorer overall mass resolution. It has been shown for samples with moderate topography that the resulting time-of-flight shift can be used to estimate the local height and partly restore the mass resolution.[2,9]

This study primarily concerns time-of-flight SIMS (ToF-SIMS) instruments. There are essentially two types of instrument design – pulsed primary ion source (currently covers most instruments) and DC primary ion source and pulsed analyser (a recent new design).[10] Here, the effects 1 to 4 above, which apply generally to both instrument designs, are studied. One important difference between the two designs is that in the pulsed primary ion type, the ion pulse is used to trigger the time-of-flight measurements for secondary ions, and the mass resolution depends on, amongst other parameters, the spread of flight times of the secondary ions. This gives rise to poorer mass resolution for topographic samples since higher sample features may have shorter flight times. In the pulsed analyser design the secondary ions pass continuously into the analyser (like conventional liquid chromatography mass spectrometers).[10] The secondary ions are subsequently bunched in time and then pulsed into a time-of-flight analyser. Consequently, the mass position and mass resolution are expected to

be approximately independent of the topography. Where parts of this study are not relevant to this instrument type, it is noted in the text.

The topographic effects described in this chapter are also relevant to SIMS instruments with non time-of-flight analyser designs, such as quadrupole or magnetic sector instruments, which are expected to be affected similarly by sample mounting, geometry, sputtering behaviour and the distortion of the ion extraction field. Although much of this work will be applicable to these instruments, they will not be discussed here in detail.

In this chapter, the effects of topography for conducting samples are reported. The study is extended to insulating samples using poly(ethylene terephthalate) (PET) fibres in Chapter 3. The aim of this study is to understand and quantify the key factors that give rise to unwanted topographical artefacts in ToF-SIMS, and to provide guidance to recognise and reduce these artefacts. This is done by combining an experimental approach using simple model systems with computer modelling using ion trajectory simulations in SIMION. The model systems consist of conducting gold wires, with nominal diameters of 33 μm, 60 μm and 125 μm. These are chosen since gold is a model conductor exhibiting a few clear mass peaks, and gold wires have well-controlled geometries and are easy to obtain in a range of diameters. This allows the variation of topographic field effects as a function of feature size to be studied at a scale that is relevant to many real devices. For samples with sub-micron topography, the field effects are minimal and they are not studied here. Improvements after instrumental optimisation are demonstrated on an anisotropically etched silicon sample. To help with practical analysis, the benefits of a simple sample holder with a V-shaped groove to reduce topographic field effects are investigated. Elsewhere in Chapter 6, using hair fibres with multi-component coatings, the rapid processing of high-resolution ToF-SIMS images for samples with topography using multivariate methods such as principal component analysis (PCA) and multivariate curve resolution (MCR) are evaluated.

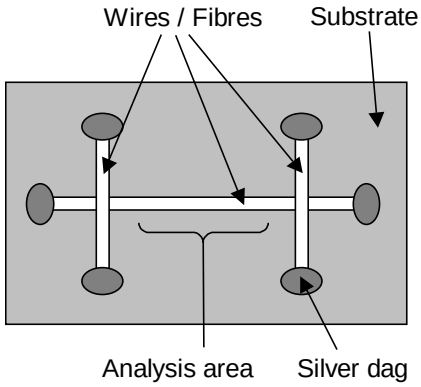

Figure 2.1 Method for mounting the wire samples used in this study.

2.2 Experimental

Gold wires (with nominal diameters of 33 μm, 60 μm and 125 μm) are obtained from Goodfellow (Goodfellow Cambridge Ltd., Huntingdon, UK) and used as received, without additional cleaning. The wires are mounted flat on a clean silicon substrate using the method shown in Figure 2.1. As we shall see later, it is important that the wire is mounted in good contact with the substrate. To do this, a section of the wire is first held under tension and mounted onto the substrate by the application of silver dag (Agar Scientific) at each end. Two additional wires are then held perpendicular to the first wire and mounted on top, roughly a quarter of the distance from the ends of the first. The perpendicular wires hold down the first wire such that the central area for analysis (marked on Figure 2.1) is in good contact with the substrate. Naturally, the wire cannot be in perfect contact with the substrate, so the gap between the wire and the substrate is estimated using an optical microscope. This is done by measuring the difference in the stage height between the positions where the centre of the wire and the substrate come into optical focus, and then subtracting from this the nominal diameter of the wire. It is found that good surface contact can be achieved between the wire and the substrate using this mounting method, and the gap can be kept to less than 5 μm.

The anisotropically etched silicon sample is kindly provided by Professor Martin Prutton (University of York). The full details of the sample are provided in Reference 11. It consists

of a Si (001) surface, where the oxide surface is photolithographically patterned and the exposed areas are etched in ethylene diamene pyrocatechol to a depth of 40 μm. This produces multiple polyhedra with eight (331) faces and four (111) faces.

SIMS analyses are conducted using an ION-TOF IV instrument (ION-TOF GmbH, Germany) of single-stage reflectron design.[12] For all experiments, the analyser reflector voltage is set to +20 V and an extraction gap of 1.5 mm between the sample and the extraction cone is used. For extraction voltage experiments, the sample is kept at ground potential and a constant extraction voltage (variable between –500 V and –2000 V) applied to the analyser extraction cone to extract positive secondary ions. This provides an extraction field which roughly covers the regime used in most ToF-SIMS instruments. For extraction delay experiments, the extraction voltage (set at –2000 V) is pulsed so that it switches on several tens of ns after the pulsed primary ions hit the sample. Standard analyser lens and reflector settings are used without further optimisation. For each analyser setting, a positive ion image is obtained for each wire diameter using a focused Bi^+ liquid metal ion gun at 25 keV, incident at $\theta = 45°$ to the sample normal for a flat sample. Images are acquired using an ion beam raster of 256 × 256 pixels. All secondary ion images are presented in the traditional manner with the *x* and *y* coordinates in the plane of a flat sample surface. Image analysis is conducted in Matlab v7.3 (The MathWorks, Inc., Natwick, MA, USA) using custom routines. The intensities are first summed over the observed length of the wire for an improved signal to noise ratio. Since the wire radius and the image field of view are known *a priori*, the originating positions of the ions (expressed as an angle ψ on the wire with respect to the extraction direction) is calculated for each pixel using simple geometry, and these are used to generate an angular intensity profile for each wire image.

Computer modelling is carried out to calculate the extraction field and secondary ion trajectories, as follows. Models are set up in an ion optics simulation software, SIMION 8.0 (Scientific Instrument Services Inc., Ringoes, NJ, USA), by placing cylinders of specified diameters on a flat conductive substrate (both at ground potential). A flat extraction plate is

placed 1.5 mm above the substrate to approximate the entrance of the analyser cone. Unless otherwise stated, the extraction voltage is kept at –2000 V and positive secondary ions are emitted from the wire and the substrate surface with an initial energy of 2 eV at a direction normal to the surface. The velocities and trajectories of the secondary ions as they accelerate towards the analyser entrance are recorded and analysed. A simple assumption is made that the angular acceptance of the analyser is 4°, and that secondary ions travelling with an angle of more than 4° to the extraction plate normal as they enter the analyser are unavailable for detection. SIMION enables visualisation and explains the essential topographic field effects observed experimentally but does not provide quantitative results, since the simple model does not take into account the secondary ion optics of the analyser system, including focusing lens, apertures and the use of dynamic emittance matching,[13] which have an effect on the ion trajectories and acceptance of the system.

2.3 Results for a gold wire

2.3.1 Topographic field effects

The total secondary ion images of a gold wire, with a diameter of 125 μm, are shown in Figure 2.2. The wire is orientated with its axes either parallel to the azimuth of the incoming primary ion beam direction (‘parallel alignment’) or perpendicular to it (‘perpendicular alignment’), and the total ion intensities are shown in both linear and logarithmic scales. It is clear that the topography critically limits the regions from which sputtered secondary ions may be detected, and chemical analysis over the whole area is difficult. We first focus on the results for parallel alignment. Only a thin central region of the wire can be detected with significant intensity, and signals from the substrate are ‘shadowed’ in the vicinity of the wire. The loss of ion intensities is caused by the severe distortion of the extraction field in the presence of the conducting wire, and can be simulated using SIMION. Figure 2.3a shows the SIMION results along the cross-section of the wire. This shows the equipotential lines (pink) and example ion trajectories (red / blue) from a conducting wire and the surrounding substrate

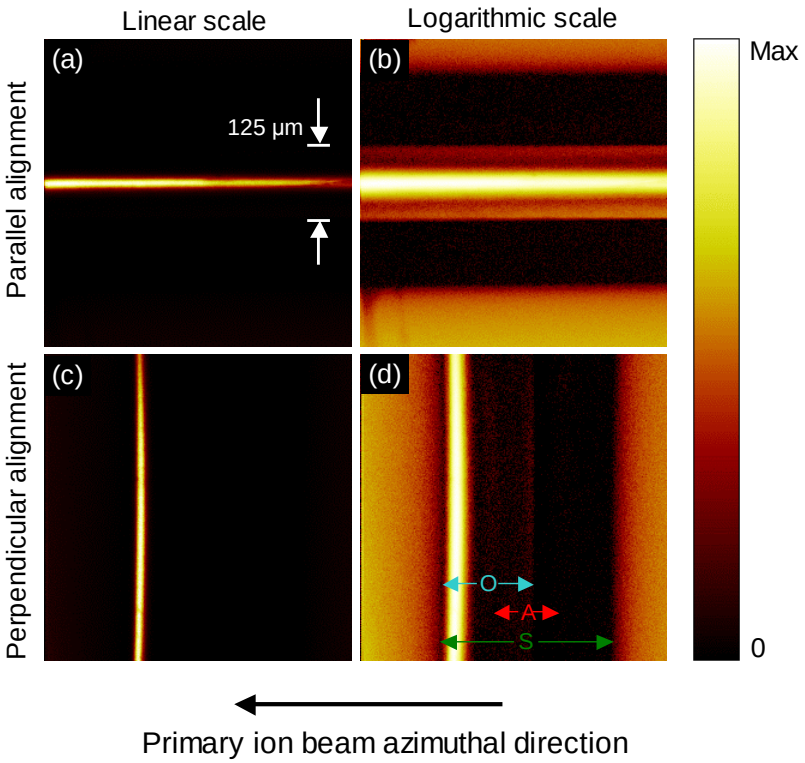

Figure 2.2 Total ion images of a gold wire with diameter 125 µm using 25 keV Bi^+ primary ions. (a) Parallel alignment, linear intensity scale. The field of view on the substrate surface is 500 µm × 500 µm (b) Parallel alignment, logarithmic intensity scale, field of view 500 µm × 500 µm (c) Perpendicular alignment, linear intensity scale, field of view 625 µm × 625 µm (d) Perpendicular alignment, logarithmic intensity scale, field of view 625 µm × 625 µm. In perpendicular alignment, the observed position of the wire in the SIMS image (O), actual position of the wire if viewed from above (A) and the shadow region (S) are marked by arrows.

for secondary ions emitted normal to the surfaces with kinetic energy of 2 eV. The equipotential lines are curved around the conducting sample, and the secondary ions acquire a large transverse velocity component as they are accelerated towards the mass analyser extraction cone. Secondary ions from the sides of the wire and the adjacent substrate, with trajectories shown by red lines, are lost due to the limited angular acceptance of the single reflectron analyser,[6] which is approximately 4°. Because of the significant topography of this example, the field effects completely dominate over the increase in the sputtering yields expected at grazing angles of incidence. Therefore we do not see a strong enhancement of secondary ion intensities at the sides of the wire, which is observed sometimes for smaller

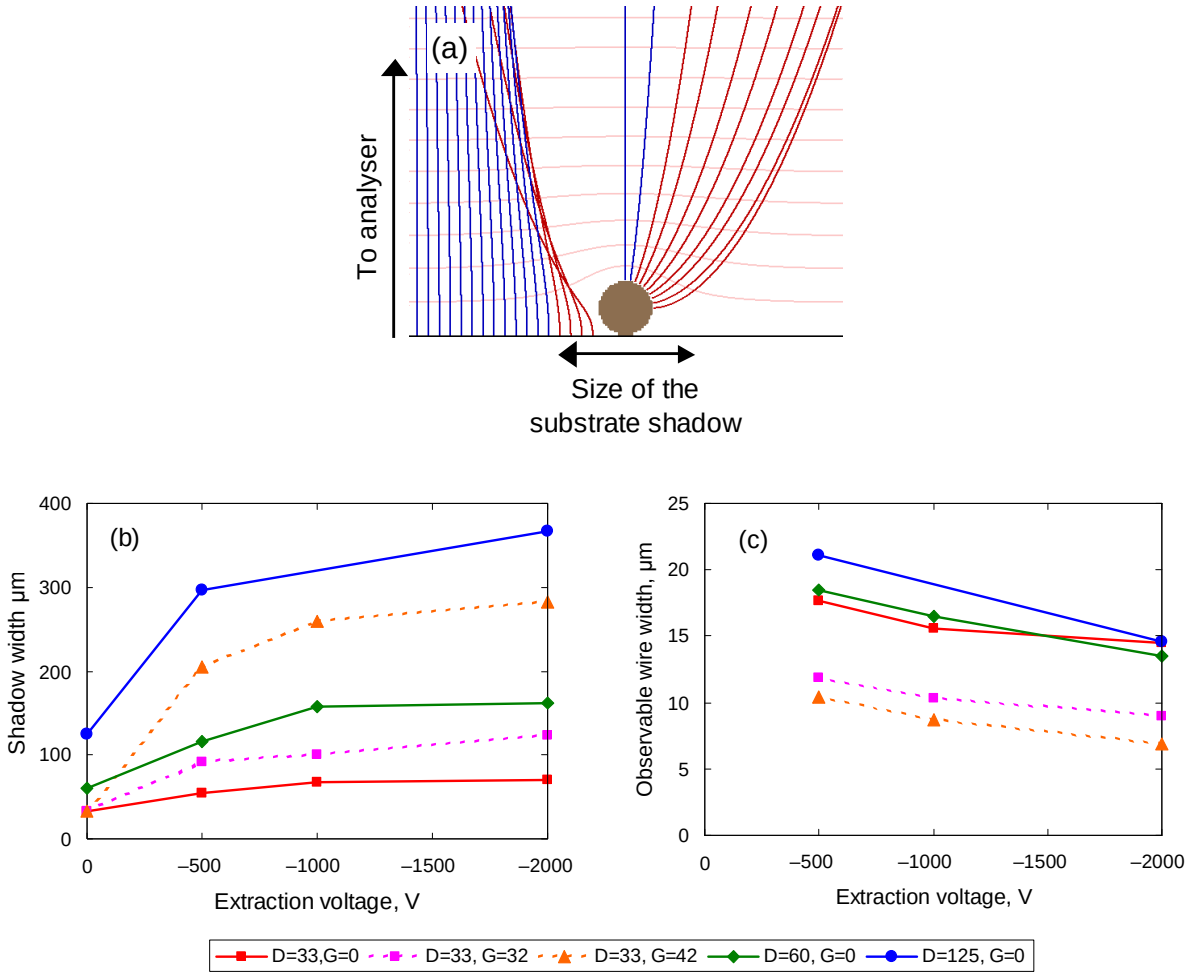

Figure 2.3 (a) SIMION simulation of a conducting wire, with a diameter of 125 µm, on a conducting substrate, showing the equipotential lines of the extraction field (pink lines) and the trajectory of sputtered secondary ions from the substrate and the wire. Assuming an analyser angular acceptance of 4°, the ions that are detected are shown in blue, and the ions that are lost are shown in red. The extraction gap is 1.5 mm and the extraction voltage is –2000 V. (b) Experimental results using 25 keV Bi^+ primary ions for gold wires of different diameters (D) and mounting gap from the silicon substrate (G), as a function of the extraction voltage from –500 to –2000 V, showing the size of the substrate shadow. For zero extraction voltage, the shadow is taken to be the wire diameter. (c) Experimental results showing the observable width of the gold wires in µm as a function of the extraction voltage.

wires or for insulating fibres where topographic field effects are much less significant.[1,14] Here these topographic effects are studied in detail to provide recommendations to analysts for their reduction.

2.3.2 Observable width of wire and shadow size

The extent of topographic effects for gold wires, for different diameters and extraction voltages, can be quantified using the total secondary ion images obtained experimentally. Figure 2.3b shows the size of the substrate shadow, defined by the position where the substrate secondary ion intensity has fallen to 10% of the plateau value for large distances from the wire, for experimental data from gold wires with diameters of 33 μm, 60 μm and 125 μm. For wires that are in good contact with the substrate (solid lines), the shadow size follows a power law for the wire diameter with an exponent of ~ 1.2 for each extraction voltage, i.e. it is disproportionately more pronounced for larger wires. The shadow size also increases sharply for poorly mounted wires that are raised from the substrate (dotted lines). This can be explained by the increased curvature of the extraction field, as the equipotential lines must contour around the raised samples. Figure 2.3c shows the observable width of the wires, defined as the full width half maximum of the thin central region in the total ion images. Poor mounting (dotted lines) drastically increases the topographic effects and reduces the observable width. Typically, for well-mounted samples (solid lines) only 15 μm of the wires may be observed regardless of the wire diameter. Expressed in terms of the angle, ψ, on the wire with respect to the extraction direction, only ions from $|\psi| \leq 26°$, 13° and 7° can be detected from the 33 μm, 60 μm and 125 μm wires, respectively. Since the area available to the primary ion beam is $|\psi| \leq 90°$, this represents a severe limitation to the chemical analysis of the wire surface. The topographic features observed here are in good qualitative agreement with those reported using a PHI nanoTOF instrument,[15] but differences in the magnitudes of these effects arise from the different extraction voltage, extraction gap and analyser design of the nanoTOF instrument.

From Figure 2.3b and Figure 2.3c, it is clear that sample mounting is crucial for the analysis of topographic samples, and it is recommended that conducting samples are in good contact with a flat conductive substrate, which minimises the distortion in the extraction field. For wires or fibres this can be achieved, for example, using the method shown in Figure 2.1. For

all samples, topographic effects can be reduced by the use of a smaller extraction voltage. This will be discussed in more detail later.

2.3.3 Effect of sample alignment

We now return to the images of the 125 μm gold wire acquired in perpendicular alignment, shown in Figure 2.2c and Figure 2.2d in the linear and logarithmic intensity scale, respectively. Due to geometry, the images are spatially distorted along the direction of the primary ion beam, which is incident from the right hand side. For angles of incidence other than normal (typically, $\theta = 45°$ is used), the coordinates of the image are not simply the *xy* spatial coordinate on the sample, but are dependent on the height *z*. Features with a height *z* are projected by a distance $d = z / \tan \theta$ to the left of the true position, as illustrated in Figure 1 in Reference 1. The effect for the wire in perpendicular alignment is marked on Figure 2.2d. The substrate shadow is marked by arrow 'S' on the figure. The wire should be in the middle of the shadow region if viewed from above (marked by arrow 'A'), but it is recorded to the left instead (marked by arrow 'O'). The perceived diameter of the wire is also increased by $\sqrt{2}$ to around 176 μm. Careful analysis of the data shows that the strongest intensities, which appear on the left hand side of the observed position of the wire, actually occur at the centre of the wire ($\psi = 0°$). Little intensity enhancement is observed on the left hand side of this bright area, despite the larger primary ion angle of incidence compared to the right hand side. Therefore, as in the horizontal alignment, the topographic field effect dominates the intensities in this image rather than the angle of incidence. Later, a method using an extraction delay to reduce field effects is presented so that the intensity changes due to the angle of incidence could be observed. In general, the extent of geometric distortions, angle of incidence effects and field effects are not trivial to predict, especially for a sample without well-characterised topography. It is recommended that samples should be analysed in an orientation that minimises geometrical distortions, if possible. For the remainder of this thesis, I will focus only on wires in the parallel alignment.

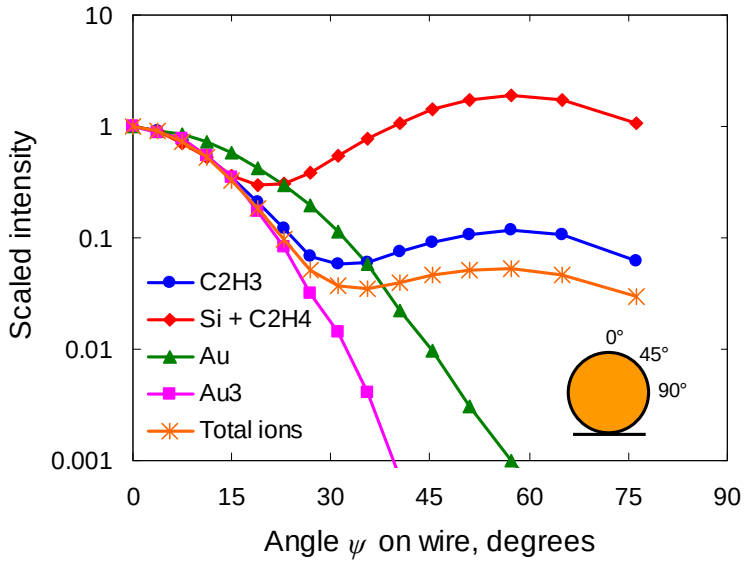

Figure 2.4 The angular intensity profile of secondary ions acquired from a 60 μm gold wire using 25 keV Bi^+ primary ions with an extraction voltage of –2000 V, scaled to their respective ion intensity at the centre of the wire, $\psi = 0°$. The inset diagram shows the angle ψ on the wire with respect to the extraction direction.

2.3.4 Effects for different secondary ions

So far only the total ion intensities have been examined. The study of individual ion images show that the extent of topographic effects also varies for different secondary ions. Figure 2.4 shows the scaled secondary ion intensities of different species (at around unit mass resolution) as a function of their originating position (angle ψ on the wire) for a 60 μm gold wire. The data are scaled to the intensity at the centre of the wire, $\psi = 0°$. In the intense central region $|\psi| \leq 15°$, all secondary ions shown vary in unison with the total ion intensity, with the exception of Au^+, which has a larger observable width. To an analyst, the spectrum at $\psi = 15°$ may be mistaken for 'cleaner' wire material, with much weaker organic peaks, than the spectrum at the centre of the wire at $\psi = 0°$. For larger angles $|\psi| \geq 30°$, the scaled intensity of Au^+ is more than an order of magnitude larger than Au_3^+. The strong enhancement of secondary ions $C_2H_3^+$, $C_2H_4^+$ and Si^+ are unrelated to this and will be discussed later in Section 2.3.5. The significant difference between Au^+ and Au_3^+ intensities is due to sputtered monatomic ions (e.g. Au^+) having, on average, higher kinetic energies than organic or cluster

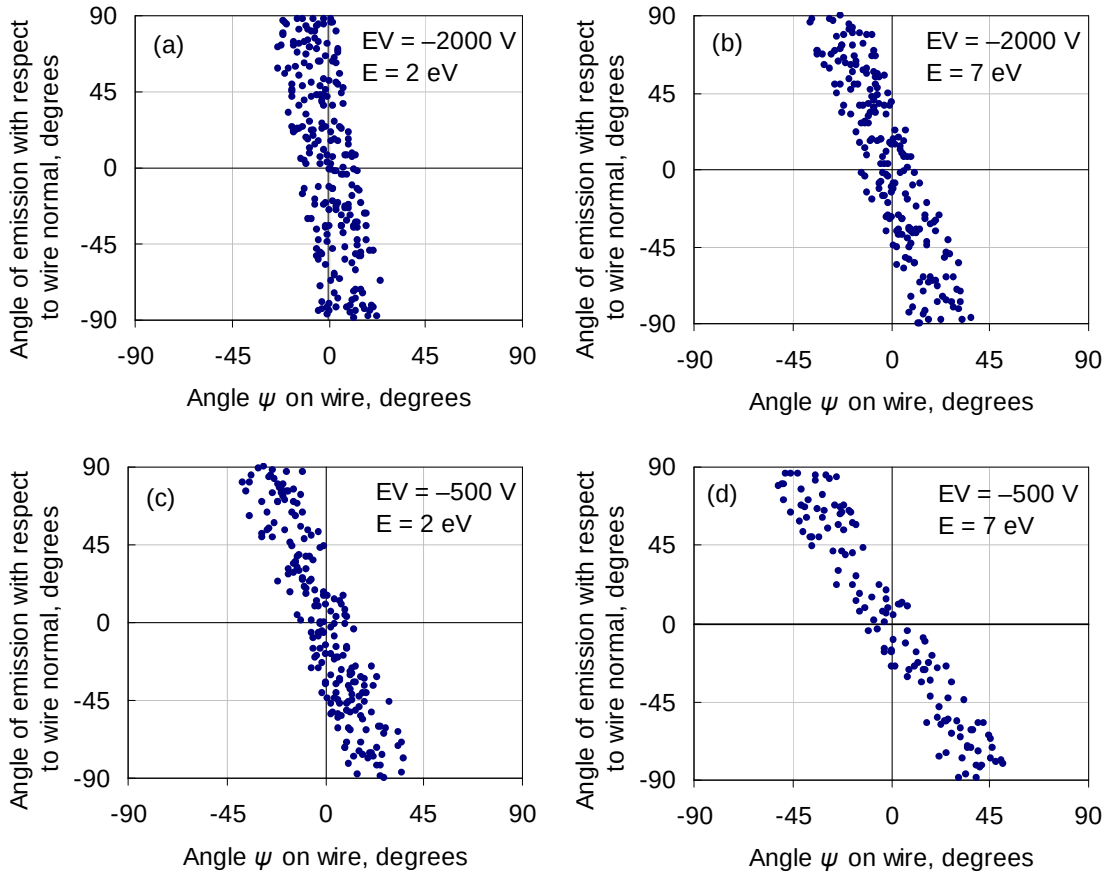

Figure 2.5 The results of Monte-Carlo simulation using SIMION, showing the secondary ions emitted from the wire surface that are likely to be detected (analyser entry angle < 4°), plotted as a function of their originating positions on the wire (angle ψ) and their angle of emission (in degrees) with respect to the normal of the wire surface. The simulations are carried out for secondary ion kinetic energies on emission (E) of 2 eV or 7 eV, and for extraction voltages (EV) of –500 V or –2000 V. These parameters are shown on the top right corner of each figure. The wire diameter and extraction gap are 125 μm and 1.5 mm, respectively.

ions (e.g. $C_2H_3^+$ or Au_3^+).[16] To understand this, Monte Carlo simulations were carried out using SIMION on the trajectory of secondary ions emitted from the wire surface with different kinetic energies (2 eV or 7 eV), over a range of emission angles with respect to the normal of the wire surface. The results are shown in Figure 2.5. The simple assumption is that the analyser has an angular acceptance angle of < 4°, so that ions travelling at a direction larger than 4° to the analyser axis at the point of entry are not detected. It is found that for larger angles ψ on the wire, the strong topographic field effect means that detection is not

possible except for ions emitted with a larger initial energy in the direction of the extractor. Thus, the observable width is larger for atomic secondary ions with higher kinetic energies, in agreement with the experimental data. Similarly, SIMION predicts that the substrate shadow is smaller for atomic secondary ions, which is also observed.

2.3.5 Scattering of the primary ions

Figure 2.4 also shows that for many secondary ions, notably at nominal mass 28 u (covering Si^+ and $C_2H_4^+$), a large enhancement effect which peaks at $\psi = 57°$ can be observed. The complete absence of the enhancement for Au^+ and Au_3^+ ions characteristic of the wire shows that it is not simply owing to an increased sputtering yield at grazing incidence angles. It is found that the enhancement is caused by the scattering of the Bi^+ primary ions from the gold surface at large angles of incidence, which has been suggested previously.[3] Scattering results in a delayed and broadened secondary ion intensity contribution to the time-of-flight spectra.

This is shown in Figure 2.6 for the H^+ peak from different regions of a 125 μm gold wire, before and after in-situ sputter cleaning to remove carbonaceous contamination. H^+ ions (from adsorbed surface contaminants) emitted from the centre of the wire (red) arrive a few ns before those emitted from the substrate (blue), since they are produced closer to the extractor. Before sputter cleaning (Figure 2.6a), at the side of the wire where the enhancement effect is observed, the regional spectrum (green) reveals two distinct contributions, one from the wire surface and one delayed, broadened contribution. The broadened contribution is also observed on other secondary ions and is not limited to H^+. After sputter cleaning (Figure 2.6b), most of the H^+ are removed from the wire surface, and the signal reduces by two orders of magnitude at the centre of the wire, although there is still a significant amount remaining on the silicon substrate. However, at the side of the wire, the broadened contribution is still significant and has the same intensity ratio to the substrate signal. The broadened contribution can be explained by a fraction of the scattered primary ions hitting the substrate at a location away from the shadow region, emitting secondary ions that are recorded by the instrument at the location of the wire after a delay of several ns. These data show that primary ion scattering is

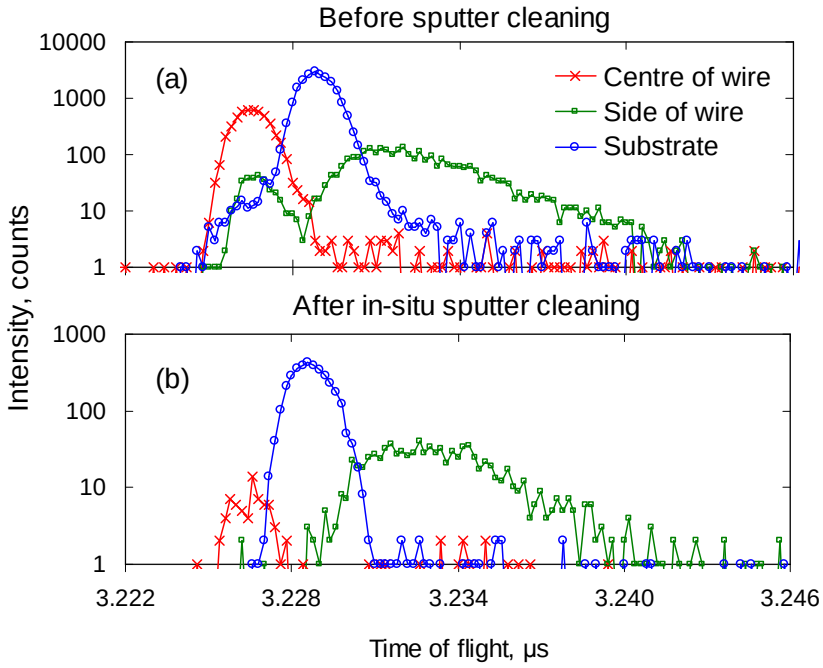

Figure 2.6 Regional time-of-flight spectra for H^+ peak, from a 125 µm gold wire using 25 keV Bi^+ primary ions (a) before sputter cleaning and (b) after sputter cleaning of the wire and substrate.

important for a primary ion incidence angle of ≥ 55° to the surface normal, and chemical components identified as localised to these areas may in fact originate from the surrounding regions. To diagnose these effects, a high mass resolution image using a bunched primary ion beam is useful to provide necessary mass resolution to identify the broadened contribution caused by scattering.

2.4 Optimising parameters

2.4.1 Extraction voltage

Figure 2.3 shows that using a smaller extraction voltage can reduce the extent of topographic effects in ToF-SIMS images of conducting samples. For example, the observable width of the gold wire is improved by ~ 35% when the extraction voltage is reduced from –2000 V to –500 V. As shown by the Monte Carlo simulations (Figure 2.5b and Figure 2.5d), at a smaller

extraction voltage, the maximum angle ψ on the wire from which ions can be detected is increased. However, at the centre of the wire ($\psi = 0°$), only secondary ions emitted with a narrower range of emission angles can be detected. This is because the ions that are emitted with an initial direction off-normal to the analyser axis receive less "pull" towards the analyser at smaller extraction voltages, and are consequently more likely to be lost due to the limited angular acceptance. Thus, using a smaller extraction voltage improves the intensities at the wire sides at a cost of reducing the intensities at the centre of the wire and from the substrate. For many analyser systems where the extraction voltage determines the ion energy during time-of-flight, using a smaller extraction voltage increases the data acquisition time, since the flight time required for measuring mass m using extraction voltage E is proportional to $(m/E)^{½}$. For these systems, using a smaller extraction voltage may reduce the mass resolution as the natural spread in the kinetic energies of sputtered secondary ions becomes a larger fraction of the total ion energy. Thus, a compromise has to be reached about the optimal reduction of topographic effects and the extraction voltage for each application.

2.4.2 Extraction delay

Topographic field effects can also be reduced via the use of an extraction delay, for instrument designs with pulsed primary ions. Here, the extraction voltage is switched on several tens of nanoseconds after the sputtering event, when the sputtered secondary ions have drifted away from the sample surface into a region where the extraction field would be less distorted by the topographic sample. The use of an extraction delay in SIMS has a similar effect as in secondary neutral mass spectrometry (SNMS), where sputtered neutrals drift freely until they are post-ionised by a pulsed laser beam and extracted. It has been shown that field effects are considerably reduced in SNMS compared to SIMS for the analysis of microparticles.[3]

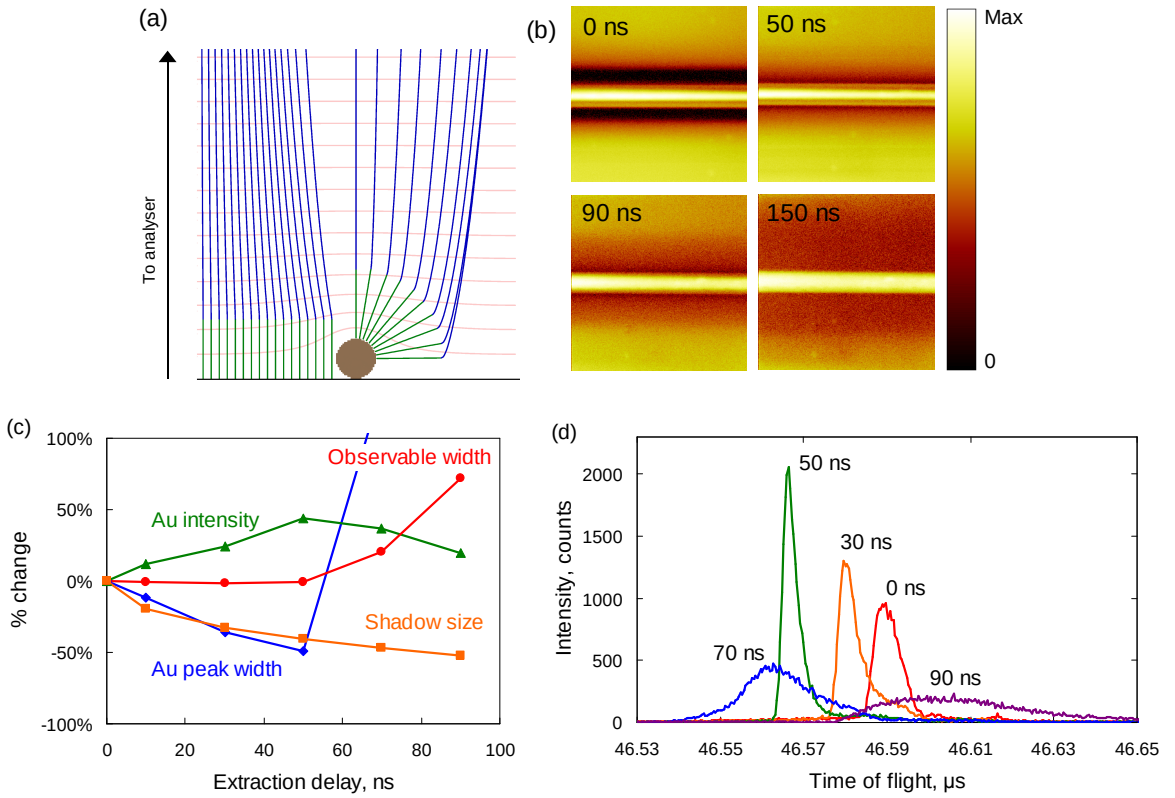

Figure 2.7 The use of extraction delay for the reduction of topographic field effects. This applies only to pulsed primary ion design instruments. (a) SIMION simulation of the effects of 50 ns extraction delay on a gold wire with a diameter of 125 µm. This shows the curved equipotential lines of the extraction field (pink lines), and the trajectory of sputtered secondary ions both before the extraction voltage is switched on (green) and afterwards (blue). All ions are detected assuming an analyser angular acceptance of 4°. (b) Experimental results for a 60 µm gold wire using 25 keV Bi^+ primary ions, showing the total ion images in logarithmic intensity scale, for extraction delays of 0 ns, 50 ns, 90 ns and 150 ns. The field of view on the substrate surface is 500 µm × 500 µm. (c) The observable width of the wire (red), the size of the substrate shadow (orange), the integrated intensity of the Au^+ peak (green) and the full width half maximum peak width (blue), as a function of the extraction delay, shown by their % change with respect to the value at zero extraction delay. (d) The time-of-flight and peak shape of Au^+ secondary ions for an extraction delay of 0 ns to 90 ns.

In the following, the use of extraction delay to reduce topographic field effects in SIMS is studied using an extraction voltage of –2000 V and standard analyser lens and reflector settings. Figure 2.7a shows the SIMION simulation results for an extraction delay of 50 ns. For comparison, the wire diameter, extraction voltage and extraction gap are the same as

those used in Figure 2.3a. The secondary ions drift in a straight trajectory away from the surface (green lines), until the extraction voltage is switched on some time later and they are quickly accelerated towards the analyser (blue lines). Compared to Figure 2.3a, the flight paths towards the analyser are less affected by topography, and the detection of the ions emitted from the sides of the wire and the substrate improves substantially, with all secondary ions travelling within the analyser acceptance angle of 4°. Figure 2.7b shows the total ion images of a 60 μm gold wire for a range of extraction delays. The observable width of the wire (red) and the shadow size (orange) are plotted in Figure 2.7c by their percentage change with respect to the value at zero extraction delay. With an extraction delay of 70 ns, the observable width of Au^+ is increased by 26%, and the substrate shadow is reduced by 42%. However, the use of an extraction delay has a large effect on secondary ion intensities, mass resolution and the ability to identify high mass species. These effects are now studied in more detail.

Figure 2.7d shows the time-of-flight spectra of the Au^+ secondary ion signals from a 60 μm gold wire, for different extraction delays. From this, the integrated intensities (green) and peak widths (blue) of the Au^+ peak are plotted in Figure 2.7c. Firstly, the effect of extraction delay on the secondary ion intensity is considered. On a flat sample, an extraction delay always causes a loss in intensity, which drops rapidly as the secondary ions eventually drift out of the extraction region. For a topographic sample, owing to improved analyser acceptance due to the reduction of topographic effects, the integrated intensity of Au^+ ions increases by more than 40% with an extraction delay of 50 ns before dropping at larger extraction delays. Secondly, the effect on the time-of-flight and mass resolution is considered. As the extraction delay is increased, the time-of-flight of Au^+ reduces and reaches a minimum at 70 ns before increasing rapidly again. This is observed for all secondary ions, and the extraction delay to achieve the minimum flight time is dependent on the ion mass and kinetic energy. This can be explained as follows. If the extraction voltage is switched on when the secondary ions are at a height h above the sample, then they will only acquire a fraction of the extraction energy. For a flat conducting sample, the fraction would be $1 - h / d$, where d is the

extraction gap. As a consequence, extraction delay leads to secondary ions having a reduced speed as they enter the analyser, and this affects their flight paths and their final flight times to the detector. At large extraction delays (e.g. for Au^+ ions beyond 90 ns), the drift distance *h* is large, and the low ion velocity means that these ions have a long flight time compared to those extracted normally. However, at smaller extraction delays (e.g. for Au^+ ions at 50 ns), the moderate reduction in ion velocity is more than compensated by the reduced penetration of these lower energy ions into the ion mirror in the reflectron analyser. Thus these ions have a shorter flight path than ions at full energy, which results in an overall reduced time-of-flight to the detector. This behaviour is by design and normally employed to improve the time focus at the detector by compensating for different secondary ion energies on emission. Here it has important consequences on the practical use of extraction delay. It is observed in Figure 2.7d that the minimum time-of-flight typically signifies the extraction delay beyond which the energy compensation of the analyser becomes ineffective, and the mass resolution degrades rapidly. With a high extraction delay, the peak shape thus becomes asymmetric with a large tail. Further SIMION simulations were carried out on a model of a complete reflectron instrument, provided by Green *et al*. and described in Reference 17. This shows that, for a flat sample, the minimum time-of-flight occurs when the secondary ions are extracted from a certain height above the surface, regardless of their mass and kinetic energies on emission. Using experimental data from a flat silicon wafer, the height is estimated to be about 60 μm above the surface, equivalent to a loss of 80 eV in extraction energy. Note that it is not straightforward to compensate for this by optimising the spectrometer, since secondary ions with different masses and energies will drift to different heights under an extraction delay, thus the optimisation of the energy compensation for one ion will generally lead to the loss of mass resolution for another. The loss in signal and mass resolution is particularly acute for low mass secondary ions, since the drift distance for a particular extraction delay and ion energy is proportional to $m^{-1/2}$.

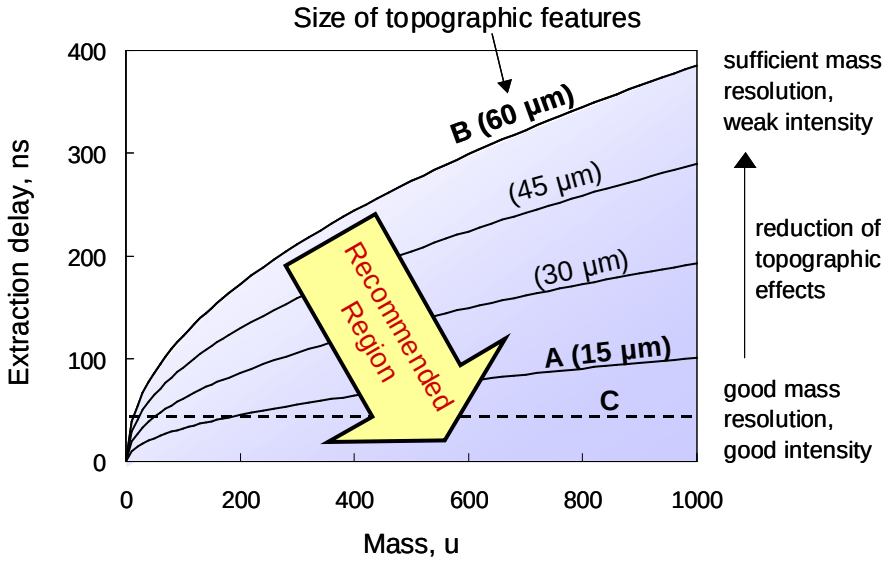

Figure 2.8 Recommendation plot for the optimal use of extraction delay for organic or cluster secondary ions, with an extraction voltage of –2000 V. This applies only to pulsed primary ion design instruments. Curve A shows the extraction delay, t_1, required to obtain minimum time-of-flight, and curve B shows the upper limit extraction delay, t_2, beyond which the peak shape ceases to be useful. Line C shows the maximum extraction delay required for the mass calibration of the data. The recommended analysis region lies below curve B. The estimated sizes of topographic features, whose effects may be minimised by the chosen extraction delay, are shown in brackets.

The effects described above represent limitations to the use of extraction delay for the reduction of topographic effects. The optimal extraction delay for a sample depends on the size of the topographic features, the mass of the secondary ions of interest, their kinetic energies on sputtering and the compromise between mass resolution, signal intensity and the extent of topographic effects. Using data from a flat silicon wafer, the recommendations are presented in Figure 2.8 for the extraction delay required for an organic or cluster secondary ion with mass *m*. Curve A shows the extraction delay, t_1, required to obtain minimum time-of-flight for the ion under study. The mass resolution and signal intensity begin to degrade from this point. Curve B shows the upper limit extraction delay, t_2, where the peak has severely broadened but the peak shape is still fairly symmetrical and Gaussian, acceptable for basic identification. At this point, the secondary ion intensity has degraded by typically a factor of two. The recommended analysis region lies below curve B. Often a large extraction delay

required for high mass and slow moving secondary ions leads to the loss of low mass and fast moving secondary ions, which are required for the mass calibration of the data. Line C shows the maximum extraction delay that retains sufficient signal for CH_x peaks for basic mass calibration. Beyond this, it is necessary to compare the spectra obtained using a low extraction delay for the identification of high mass peaks.

It is possible to estimate the size of topographic features whose effects may be minimised by a particular extraction delay, using the distance that the secondary ions have drifted away from the surface. Assuming the emitted ions have a kinetic energy of 2 eV, the upper limit extraction delay t_2 occurs at a drift distance of 240 μm. For minimum time-of-flight, t_1, this distance is 60 μm. From Figure 2.3a, we can see that the drift distance generally needs to be 3 to 4 times the size of topographic features for the effective removal of field curvature caused by sample topography. To help analysts, the suggested size of topographic features for each extraction delay is labelled in Figure 2.8. This simple estimate is in good agreement with experimental data obtained for Au_3^+ secondary ions (mass 591 u) from a 60 μm gold wire, which shows no improvements in the observable width after an extraction delay of 250 ns, approximately equivalent to a drift distance of 200 μm. Using Figure 2.8, an extraction delay may be quickly selected, depending on the desired compromise between mass resolution, signal intensity and topographic effects.

Finally, it is noted that an extraction delay is only useful for short primary ion pulse widths, where the pulse width is much smaller than the extraction delay. An extraction delay can also cause a shift of the image along the primary ion beam azimuth direction, as the beam ceases to be deflected by the extraction field. On some instruments, the setting at which the extraction delay is 0 ns may not be well defined and analysts should increase the delay incrementally until a change in the spectra is observed.

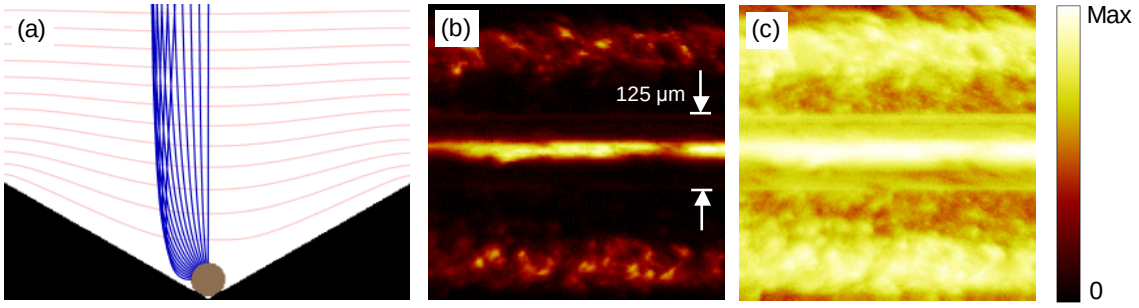

Figure 2.9 The use of a V-groove sample holder to reduce topographic field effects for conducting wires. The angle of the groove is 30° to the horizontal and the groove depth is 450 µm. (a) SIMION simulation of the secondary ions emitted from a 125 µm wire. This shows the curved equipotential lines of the extraction field (pink lines), and the trajectory of sputtered secondary ions (blue lines). All ions are detected assuming an analyser angular acceptance of 4°. (b) Experimental results using 25 keV Bi^+ primary ions for a 125 µm gold wire mounted on the V-groove sample holder, field of view 500 µm × 500 µm, acquired using a primary ion beam raster of 128 × 128 pixels, showing the total ion image in linear intensity scale for comparison with Figure 2.2a. (c) Experimental results as above showing the total ion image in logarithmic intensity scale, for comparison with Figure 2.2b.

2.4.3 Improved sample mounting

Where possible, topographic field effects can also be reduced significantly using special sample mounting methods to minimise the distortion of the extraction field. Whilst the simple method shown in Figure 2.1 produces good results for the analysis of a single conducting wire, and is relatively quick to implement, topographic field effects can be strongly reduced if a number of wires are mounted adjacent to each other in a parallel close-packed fashion. The disadvantages of this method are that it is relatively time consuming and that signal from the sides of the wires may not be available due to the close proximity of another sample.

To address these issues, SIMION is used to design a special sample holder which could effectively counteract the distortion of the extraction field arising from a conducting wire. The criteria are that the holder must be easy to use and be applicable to wires with a range of diameters. It is found that a single V-shaped groove cut into a sample block, with the wire mounted such that it is laying flat at the bottom, provides good results. The simulation and

experimental results for the sample holder are shown in Figure 2.9. The SIMION simulation (Figure 2.9a) shows an optimal design with the angle of the groove at 30° to the horizontal and a groove depth of 450 μm. Secondary ions emitted from the side of the wire are deflected by the groove towards the analyser, and the groove acts as a simple focusing lens for the secondary ions. All ions arrive at the analyser entrance with an angle of less than < 2° and are therefore available for detection. Figure 2.9b and Figure 2.9c show such a device in practice using a 125 μm gold wire. The total ion image is shown in linear and logarithmic intensity scale, for comparison with Figure 2.2a and Figure 2.2b, respectively. Although it is clear that topographic field effects are still important, the sample holder substantially reduces this and the observable width of the wire is increased to 31.2 μm, equivalent to $|\psi| \leq 15°$ on the wire. This represents a ~ 115% improvement over previous results achieved with the wire mounted on a flat silicon wafer. The sample holder also significantly reduces shadow regions on the substrate, although the substrate intensities are now uneven because of the surface roughness of the sample holder. This very simple prototype device significantly reduces topographic field effects with the benefit that the mass resolution is not strongly affected.

2.5 Application example – Antisotropically etched silicon surface

In this section, the practical application of extraction delay for the reduction of topographic field effects is demonstrated on a more complex sample. SIMS analysis is carried out on an anisotropically etched silicon sample, obtained from Prutton *et al.*[11] This sample has been previously used to evaluate topographical effects in Auger electron spectroscopy.[11] An SEM image of the sample is shown in Figure 2.10a. This shows a typical polyhedron with a height of 40 μm and multiple sloping surfaces that are inclined at 46.5° or 54.7° to the horizontal plane as calculated from the crystal structure. The total ion image obtained from SIMS without an extraction delay, obtained using a Bi^+ primary ion beam incident at $\theta = 45°$ to the horizontal from the right hand side of the image, is shown in Figure 2.10b. Note that in Figure 2.10b-c the sample is rotated approximately 45° with respect to Figure 2.10a as this

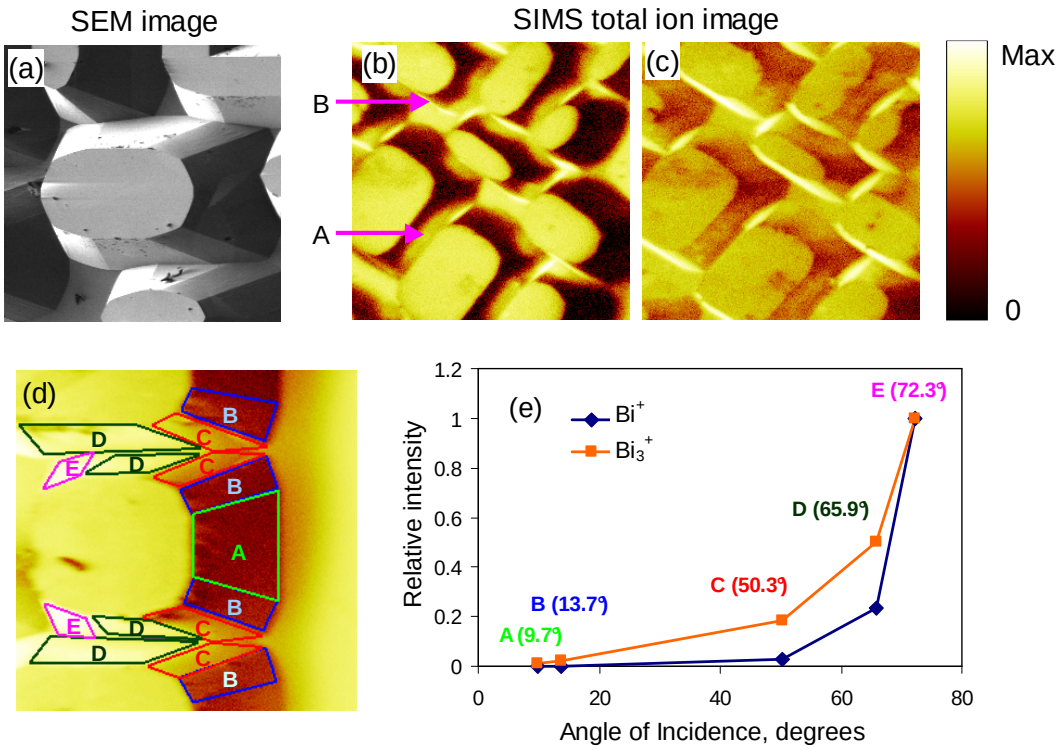

Figure 2.10 (a) SEM image of an anisotropically etched Si sample, showing a typical polyhedron on the surface, field of view 300 μm × 300 μm. (b) SIMS total ion images of the same sample using 25 keV Bi^+ primary ions, with no extraction delay, and with (c) 110 ns extraction delay. The intensities are shown in logarithmic scale and the field of view assuming a flat sample surface is 500 μm × 500 μm. (d) Total ion image acquired using 25 keV Bi^+ primary ions with 130 ns extraction delay (log scale), field of view 290 μm × 290 μm, showing the regions of interest on different faces. (e) Relative ion yields of PDMS characteristic peak ($C_5H_{15}OSi_2^+$) as a function of primary ion angles of incidence, using Bi^+ and Bi_3^+ primary ions with 130 ns extraction delay, for the regions of interest defined in (d). The intensities are normalised to their values at 72.3°.

allows the topographic effects to be shown more clearly. Clear contrast is observed due to topography. Firstly, few secondary ions can be detected from the sloping surfaces because of strong topographic field effects, except at locations where a sloping surface is immediately adjacent to another near the bottom of the polyhedra. An example of this is marked on the figure by arrow A. Here, the extraction equipotential lines form a 'V' shape as they must curve around the conducting surface, and this significantly improves the acceptance of secondary ions from the sloping surfaces, similar to the V-groove device discussed earlier. Secondly, a large increase of intensities at grazing incidence angles can be observed, marked

on the figure by arrow B. The increase is approximately 3 times compared to the top surface of the polyhedra, despite the strong field effects on these sloping surfaces. It is clear that field effects and primary ion angles of incidence are both significant mechanisms of topographical contrast in this image.

To reduce topographic field effects and investigate the variations in secondary ion yields at different primary ion angles of incidence, Figure 2.10c shows the total ion image obtained on the same area when an extraction delay of 110 ns is applied. The overall topographic contrasts are reduced significantly and it is possible to detect secondary ions originating from the entirety of the sample surface. The increase in secondary ion intensities at grazing angles of incidence is now more than 5 times due to the strong reduction of field effects. To investigate further, Figure 2.10d shows the total ion image obtained using an extraction delay of 130 ns, with the primary ion beam azimuth aligned with the edges of the polyhedra. The differences in the ion yields on the different sloping surfaces are now clear. Five regions of interest are specified and these are marked A to E on the figure. From these regions of interest, the relative ion yields as a function of the angles of incidence (calculated from the geometry of the sample) are plotted in Figure 2.10e, for images acquired using Bi^+ and Bi_3^+ primary ions. This uses the $C_5H_{15}OSi_2^+$ peak (nominal mass 147 u), characteristic of the polydimethylsiloxane (PDMS), a mobile surface contaminant that is fairly evenly distributed on the surface. The extraction delay chosen is below the upper limit of 150 ns (curve B on Figure 2.8) for this ion. The intensities are normalised to their values at the maximum incidence angle of 72.3°. It is found that the ion yields using Bi_3^+ have a weaker dependence on the angle of incidence compared to Bi^+. This is expected from the non-linear enhancement of cluster ion sputtering. Although it is not possible to completely eliminate the field effects, for example, the angle of incidence dependence of the ion yields for Bi^+ does not follow the expected $\sec^f \theta$ distribution, it is clear that useful semi-quantitative SIMS intensities can still be obtained from highly topographic samples using the simple recommendations presented here. Notwithstanding the reduction in mass resolution and the loss of intensities for lower mass ions, an extraction delay can be extremely helpful for analysts trying to localise

molecular components on a highly topographic surface, where they are not interested in the behaviour of smaller fragment peaks. The results also suggest that cluster ion beams further reduce the dependence of secondary ion yields on the primary ion angle of incidence, thus can be used to reduce topographic contrast in ToF-SIMS images. This is expected to be especially beneficial for samples with much smaller topographic features, where the image contrast becomes dominated by the different primary ion angle of incidence rather than topographic field effects, for example the analysis of surfaces with sub-micron topography.

2.6 Conclusions and recommendations

This chapter presents a detailed study of the key factors that give rise to topographic artefacts in ToF-SIMS images of conducting samples. Aside from simple geometry effects, the majority of unwanted topographical contrast can be accounted for by topographic field effects (where the distortion of the extraction field by the presence of the sample cause the loss of secondary ion signals) or by variations in the primary ion incidence angle. Using these results, the following recommendations are given for conducting samples:

1. If possible, topographic samples should be analysed in an orientation that minimises geometrical distortions, for example, by aligning wires or fibres parallel to the primary ion beam azimuth.

2. Samples should be mounted in such a way as to minimise the distortions of the extraction field, if possible. Wires or fibres should be mounted in good contact with a flat conductive substrate (following Figure 2.1), mounted parallel to each other in a close-packed fashion, or in a V-groove sample holder (Figure 2.9) to reduce field effects.

3. The field effects caused by topography may be reduced by using a smaller extraction voltage or an extraction delay. An extraction voltage of –500 V for positive ions is found to be useful for the instrument used in this study. Extraction delay is only applicable to pulsed primary ion design instruments and has a significant effect on

mass resolution and signal intensity. Figure 2.8 provides a simple guide for the extraction delay suitable for a given size of topographic features and secondary ion species.

4. The variation of secondary ion yields with the primary ion incidence angle is also a significant cause of topographic contrast. This can be reduced using a cluster ion beam such as Bi_3^+ instead of Bi^+.

5. At large angles of incidence, primary ions may be scattered from one region of the sample to another. Scattering may be diagnosed using a high mass resolution image acquired with a bunched primary ion beam.

Complementary recommendations for insulating samples are presented in Chapter 3. In the future, improved mass spectrometer designs would be crucial to further reduce topographic effects and enable the applications of SIMS to a wider range of industrial samples. This could be achieved, for example, by increasing the angular acceptance of the analyser, or by extending the usefulness of extraction delay using more sophisticated energy compensation and methods to restore mass resolution.

References

1 S. Rangarajan and B. J. Tyler, Journal of Vacuum Science & Technology A **24,** 1730 (2006).

2 L. A. McDonnell, T. H. Mize, S. L. Luxembourg, S. Koster, G. B. Eijkel, E. Verpoorte, N. F. de Rooij, and R. M. A. Heeren, Analytical Chemistry **75,** 4373 (2003).

3 B. Hagenhoff, Mikrochimica Acta **132,** 259 (2000).

4 S. J. Pachuta, Applied Surface Science **231-2,** 217 (2004).

5 R. Avci, A. M. Hagenston, N. L. Equall, G. S. Groenewold, G. L. Gresham, and D. A. Dahl, Surface and Interface Analysis **27,** 789 (1999).

6 M. P. Seah, C. A. Clifford, F. M. Green, and I. S. Gilmore, Surface and Interface Analysis **37,** 444 (2005).

7 B. J. Garrison, Nuclear Instruments & Methods in Physics Research Section B-Beam Interactions with Materials and Atoms **17,** 305 (1986).

8 A. Delcorte, X. Vanden Eynde, P. Bertrand, and D. F. Reich, International Journal of Mass Spectrometry **189,** 133 (1999).

9 L. A. McDonnell, S. R. Piersma, A. F. M. Altelaar, T. H. Mize, S. L. Luxembourg, P. D. E. M. Verhaert, J. van Minnen, and R. M. A. Heeren, Journal of Mass Spectrometry **40,** 160 (2005).

10 J. S. Fletcher, S. Rabbani, A. Henderson, P. Blenkinsopp, S. P. Thompson, N. P. Lockyer, and J. C. Vickerman, Analytical Chemistry **80,** 9058 (2008).

11 M. Prutton, L. A. Larson, and H. Poppa, Journal of Applied Physics **54,** 374 (1983).

12 J. Schwieters, H. G. Cramer, T. Heller, U. Jurgens, E. Niehuis, J. Zehnpfenning, and A. Benninghoven, Journal of Vacuum Science & Technology a-Vacuum Surfaces and Films **9,** 2864 (1991).

13 J. E. Campana, J. J. DeCorpo, and J. R. Wyatt, Review of Scientific Instruments **52,** 1517 (1981).

14 T. Kojima, H. Kitano, M. Niwa, K. Saito, Y. Matsushita, and K. Fukushima, Surface and Interface Analysis **43,** 562 (2011).

15 Quantitative analysis of topographic effects on conductive surfaces, downloaded from <http://www.phi.com>**,** Physical Electronics, Inc., (2009).

16 S. X. Sun, C. Szakal, N. Winograd, and A. Wucher, Journal of the American Society for Mass Spectrometry **16,** 1677 (2005).

17 F. M. Green, I. S. Gilmore, and M. P. Seah, Journal of the American Society for Mass Spectrometry **17,** 514 (2006).

Chapter 3 – Topography and field effects in SIMS: Insulating samples

3.1 Introduction

Sample topography is a significant issue in surface chemical analysis using secondary ion mass spectrometry (SIMS).[1-4] In the previous chapter, a detailed analysis of topographic effects for conducting samples was given, covering the following issues:

1. The mounting of topographic samples;
2. Geometrical effects, including the alignment of wires or fibres either parallel or perpendicular to the primary ion beam azimuth;
3. Sputtering behaviour, for example the variation of secondary ion yields with the local primary ion angle of incidence, and primary ion scattering effects at grazing incidence;
4. Topographic field effects, caused by the distortion of the extraction field in the presence of the sample, which cause significant loss of ion intensities and shadowing.

Since these effects are also generally applicable to insulating samples, to avoid repetition, points 1 to 3 will not be specifically covered in this chapter. Instead, I will focus on aspects where the topographic effects are significantly different for insulating samples compared with conducting samples. This includes the penetration of the extraction field into the sample (which affects the extent of topographic field effects) and charge compensation using a low energy electron flood gun.

In this study, a simple experimental model system is used in combination with finite element modelling of the extraction field using COMSOL to understand the key factors that give rise to unwanted topographical artefacts in ToF-SIMS images of insulating samples, and provide guidance to analysts for their reduction. The model system consists of poly(ethylene terephthalate) (PET) fibres (nominal diameters 100 μm) mounted on a flat substrate. The

approach here is similar to that in Chapter 2, allowing direct comparisons to be made on the relative extent of topographic effects for conducting and insulating samples.

Most of the discussions in this chapter are specific to an ION-TOF ToF-SIMS IV instrument of a single stage reflectron design, where the sample is held at ground potential and a standard voltage is applied at the extraction cone to extract secondary ions. In these systems, the reflector voltage determines the energy acceptance of the analyser and must be adjusted for insulating samples. The correct setting of the reflector voltage is discussed in Section 3.3.1. It is worth noting that the situation is different with PHI TRIFT instruments, where the extractor is kept at ground potential and secondary ions are extracted via the application of a sample bias. For these instruments, the sample bias determines both the energy of the secondary ions and their acceptance, and this is optimised for insulating samples. This will not be discussed here. A detailed study of the sample bias voltage for the analysis of insulating fibres in PHI TRIFT instruments can be found in Reference 5.

3.2 Experimental

Polyethylene terephthalate (PET) fibres with nominal diameters of 100 μm were obtained from Goodfellow (Goodfellow Cambridge Ltd., Huntingdon, UK) and used as received, without additional cleaning. The fibre is mounted onto a clean substrate (either a silicon wafer or a glass slide) using the method shown in Figure 2.1.

SIMS analyses are conducted using an ION-TOF IV instrument (ION-TOF GmbH, Germany) of single-stage reflectron design.[6] The extraction gap is fixed to 1.5 mm. For positive secondary ions, an extraction voltage between –500 V and –2000 V is used. The correct setting of the reflector voltage is described in Section 3.3.1, although the reflector voltage is kept at +20 V for the majority of the experiments for the reasons stated in Section 3.3.2. For negative secondary ions, the polarities of the extraction and reflector voltages are reversed. Charge compensation is effected by low-energy electrons (variable energy between 10 – 25 eV) provided by a flood gun mounted at an angle of 57° to the sample normal. The

analyser is operated in pulsed extraction mode, with the voltage of the extraction cone alternating between the extraction voltage (when the primary ions hit the sample) and the extraction bias voltage (when the electron flood gun is active). The extraction bias prevents the flood gun electrons from entering the analyser and is normally set to –30 V. Positive and negative ion images are obtained using a focused Bi^+ liquid metal ion gun at 25 keV energy, incident at $\theta = 45°$ to the sample normal for a flat sample. Unless otherwise stated, images are obtained using a digital primary ion raster in 'random' mode to minimise sample charging effects. All secondary ion images are presented in the traditional manner with the *x* and *y* coordinates in the plane of a flat sample surface. The ion beam is incident from the right with its azimuth parallel to the *x*-axis.

Computer modelling was carried out to calculate the electric field around the insulating fibre and secondary ion trajectories. Models are set up in a finite element analysis program COMSOL Multiphysics 3.4 (COMSOL Inc., Burlington, MA, USA), by placing an insulating cylinder with a diameter 100 μm and dielectric constant $\varepsilon_r = 3$ on a conducting plane that is kept at ground potential. A flat extraction plate is then placed 1.5 mm from the substrate to approximate the entrance of the analyser cone. Unless otherwise stated, an extraction voltage of –2000 V for positive ions and +2000 V for negative ions are used. COMSOL calculates the trajectories of secondary ions emitted from the fibre and the substrate, assuming secondary ions have a mass of 28 u and zero kinetic energy on emission. To simulate the effect of sample charging by either the primary ions or the charge compensation electrons, electrostatic charges are added to the top surface of the fibre available to the primary ion beam. For simplicity, the charges are assumed to be distributed uniformly. The charge density is determined using the value where the surface potential at the top of the fibre is –20 V (for electron charging) and +50 V or +100 V (for primary ion charging) when the extraction voltage is zero. Secondary ion trajectories are then calculated as before for comparison.

3.3 Results and discussion

3.3.1 Surface potential and reflector voltage

First, the effect of sample topography on the extraction field is discussed. In Chapter 2, it is shown that for conducting samples with topography, the extraction equipotential lines curve around the sample, which is kept at ground potential. The situation is different for insulating samples, where the extraction field penetrates the sample depending on its dielectric constant and thickness. This results in a non-zero surface potential and a potential gradient within the sample. A COMSOL simulation was carried out to assess whether the use of a pulsed extraction would result in time-dependency in the surface potential of insulating samples. It was found that the surface potential reaches its steady state value almost instantaneously once the extraction voltage is switched on and dynamic effects are negligible for the purpose of SIMS analyses. Therefore, static COMSOL models are used for all the subsequent simulations.

Figure 3.1a shows a COMSOL simulation of a PET fibre (diameter 100 μm), mounted in contact with a flat conducting substrate at ground potential, with an extraction voltage of –2000 V to extract positive secondary ions. The equipotential lines for the extraction field are shown in pink with a spacing of 20 V. For insulating samples with topography, the surface potential varies spatially across the sample and is not trivial to predict. This causes two important effects. First, the achievable mass resolution for fibre secondary ions is affected. Figure 3.1a shows that the ions emitted from the side of the fibre are accelerated by a larger potential difference than ions emitted from the top. In this example, there will be a 34 eV kinetic energy difference between the secondary ions emitted from the top and the side by the time they enter the analyser. Although the reflectron analyser provides first order energy compensation, it is not optimised for such a large energy spread. Therefore the same ion species from different locations will arrive at the time-of-flight detector at different times, resulting in poor mass resolution in the overall fibre spectra. Second, the varying surface potential affects the correct setting of the reflector voltage, which determines the energy

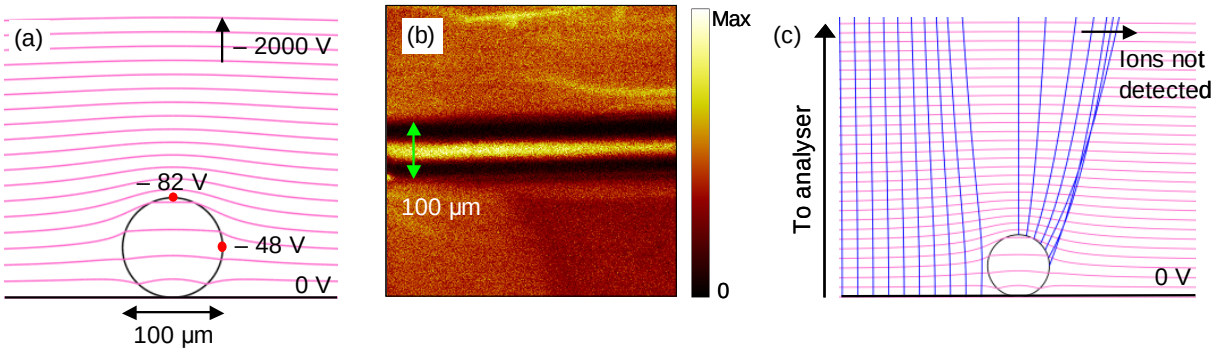

Figure 3.1 Topographic field effects on a PET fibre with diameter 100 µm, mounted onto a flat conducting substrate. (a) COMSOL modelling of the extraction field and the surface potential on the fibre along the cross-section direction. The extraction voltage is –2000 V and the extraction gap is 1.5 mm. The dielectric constant of the fibre is assumed to be ε_r = 3.0. The equipotential lines of the extraction field are shown in pink with a spacing of 20 V. The surface potentials at the top and the side of the fibre are labelled with red dots. (b) The total ion image of the PET fibre obtained experimentally for positive ions. The intensities are shown on a linear intensity scale. The field of view is 500 µm × 500 µm. (c) The COMSOL simulation as in (a) but with secondary ion trajectories shown in blue, for zero energy secondary ions emitted from the fibre surface and from the substrate adjacent to the fibre. The equipotential lines of the extraction field are shown in pink.

acceptance of the reflectron analyser. For ION-TOF IV instruments, the optimal reflector voltage is +20 V relative to the sample surface potential for positive ions, which provides an energy acceptance of up to 20 eV. For an insulating fibre, the ions emitted from the side have a higher kinetic energy than those from the top when they enter the analyser, and may be lost if the reflector voltage is too low. It is therefore recommended that the reflector voltage should be at least +20 V higher than the potential at the side of the fibre for the optimal acceptance of all fibre secondary ions (the polarity is reversed for negative ions). This is applicable regardless of how the fibre is mounted. In the example in Figure 3.1a, a reflector voltage of –28 V should be used.

For the convenience of analysts, Equation 3.1 shows a simple empirical formula for the potential at the side of a fibre, V_S, mounted on a flat conducting substrate, with ~ 2% accuracy to the values calculated from COMSOL, for $0 \leq \varepsilon_r < 20$.

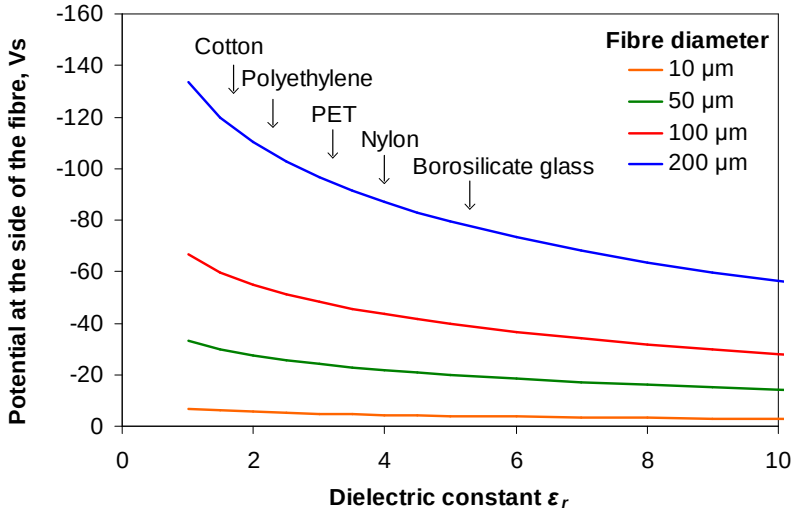

Figure 3.2 A graph showing the surface potential at the side of the fibres, V_S, for fibres with different dielectric constants and diameters, mounted flat on a conducting substrate as shown in Figure 3.1. Dielectric constant values are obtained from Kaye and Laby.[7] An extraction voltage of –2000 V and extraction gap of 1.5 mm is used for the COMSOL calculation. It is recommended that the reflector voltage should be at least +20 V higher than the potential at the side of the fibre for the optimal acceptance of fibre secondary ions. The polarity is shown for positive secondary ions and should be reversed for negative secondary ions. For reference, the value of V_S at $\varepsilon_r = 1$ is the same as the potential above the surface at the same vertical position but with no fibre present.

$$V_S = \frac{V_E d}{2g}(0.5787\log(\varepsilon_r) - 1) \tag{3.1}$$

Here, V_E is the signed extractor voltage in Volts, g is the extraction gap and d is the diameter of the fibre, both in the same units, and ε_r is the dielectric constant of the fibre. This is plotted in Figure 3.2 for fibres of different diameters using a typical extraction voltage of –2000 V and an extraction gap of 1.5 mm. Provided the extraction gap is much larger than the fibre diameter, the surface potential of the top surface, V_T, and at the side of the fibre, V_S, scale linearly with extractor voltage, fibre diameter, and roughly scale with the logarithm of the dielectric constant.

In practical analyses, the surface potential may not be readily measured on the side of fibres, due to the availability of the signal and topographic effects. In this case, for fibres mounted in good contact with a flat substrate (whether conducting or insulating), analysts can measure the

surface potentials at the top of the fibre and on the substrate away from the sample, and set the reflector voltage to be +20 V higher than the average value of the two for positive ions (the polarity is reversed for negative ions). This provides a conservative value that satisfies the energy acceptance consideration for all fibre secondary ions.

3.3.2 Topographic field effects

In Sections 3.3.2 and 3.3.3, the SIMS images of a PET fibre mounted on a flat silicon substrate is studied. To allow the detection of all secondary ions including those originating from the substrate, a reflector voltage of ± 20 V is used in the analyses. The use of a larger reflector voltage degrades the mass resolution and mass accuracy of the ions originating from the fibre, as it increases the spread of the relative time-of-flight of secondary ions emitted with different kinetic energies.[8] However, this is found to have an insignificant effect on the integrated intensities of the fibre peaks.

Figure 3.1b shows the total ion image acquired on a PET fibre (ε_r ~ 3) with a diameter of 100 μm, mounted onto a flat silicon substrate. The fibre is mounted with its axis roughly parallel to the primary ion beam azimuth, which is incident from the right hand side of the image. The topographic field effects are qualitatively similar to those observed on a conducting gold wire. Secondary ions are strongly detected only on a thin central area of the fibre, and there is little signal from the sides. This is caused by the distortion of the extraction field by the dielectric sample. Figure 3.1c shows the simulated trajectories for secondary ions emitted from the fibre surface and from the substrate adjacent to the fibre, using the COMSOL model in Figure 3.1a. Because of the curvature of the extraction field, secondary ions are deflected laterally as they accelerate towards the analyser, and they are lost due to the limited angular acceptance of the analyser, which is estimated to be around 4°. In Figure 3.1c, only the first two trajectories to the right of the axial emission is thus detected. To quantify this experimentally, the observable width of the PET fibre (defined as the full width at half maximum of the central bright region in the total ion image) is calculated. This gives an observable width of 27 μm. Expressed in terms of the angle, ψ, on the fibre with respect to the

extraction direction, only ions from $|\psi| \leq 13°$ can be detected with significant intensity. Since the area available to the primary ion beam is $|\psi| \leq 90°$, this is a significant limitation to the chemical analysis of the fibre surface. Figure 3.1c also shows that the substrate secondary ions emitted close to the fibre are deflected slightly due to field effects. For the PET fibre studied here, this is not sufficient to cause an observable loss of ion intensity. This is in contrast to conducting wires, where the topographic field effects are much more severe. In Chapter 2, it is shown that for a gold wire with a diameter of 125 μm, the observable width is only $|\psi| \leq 7°$, and a large substrate shadow can be seen with few secondary ions detected over a 365 μm area (around 120 μm on either side of the wire). In general, topographic field effects for insulating samples are much less severe than conducting samples of the same dimensions, due to the penetration of the extraction field into the sample which reduces the distortion of the field. The lower the dielectric constant, the greater the penetration of the field (as seen in Figure 3.2) and the less severe the topographic field effects, but with larger extraction energy difference between ions emitted from different heights on the sample. Thus, cotton fibres ($\varepsilon_r \sim 1.3$) would show much lower topographic field effects than nylon fibres ($\varepsilon_r \sim 4.5$) of the same diameter in the ion images, but with greater mass peak broadening in the spectra.

3.3.3 The effect of topography on charge compensation

Charge compensation using a low energy electron flood gun is typically employed for the analysis of insulating samples. This prevents the accumulation of positive charges on the surface as the sample is bombarded by a positively charged primary ion beam. The charge compensation needs to be effective without introducing excess electron fluence to the surface, which may damage sensitive organic samples. Guidance for the optimisation of charge compensation for polymer samples is given in Reference 9. In this section I discuss how sample topography influences effective charge compensation. Under typical operating conditions, insulating samples are found to be negatively charged by the incident flood gun electrons. The effects depend on the secondary ion polarity and they are covered separately below.

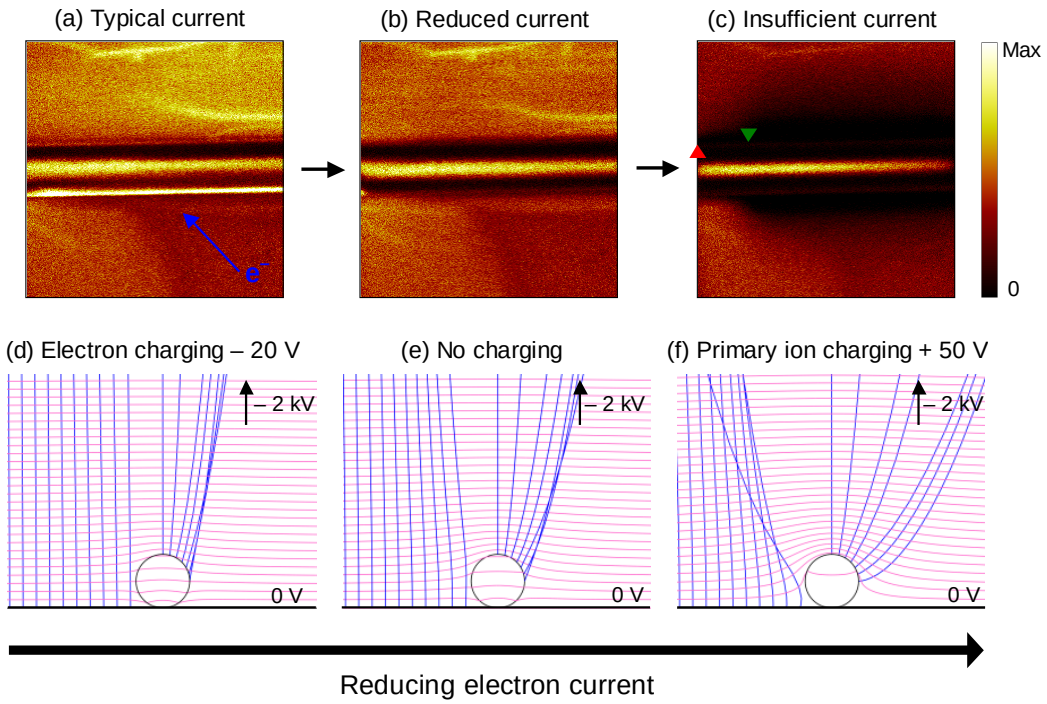

Figure 3.3 The effect of the electron current for charge compensation in the positive ion mode, using a PET fibre (diameter 100 μm) mounted on a conducting silicon substrate. (a) to (c) show the total ion images as the electron current is reduced. The images are acquired over the same area of the sample, with an electron energy of 20 eV and field of view of 500 μm × 500 μm. (d) to (f) show the corresponding COMSOL simulations along the vertical cross-section of the fibre, showing the equipotential lines of the extraction field in pink with a spacing of 20 V, and the trajectories of the secondary ions in blue.

Positive ion mode

For the PET fibre, the effect of charge compensation on the total ion images acquired in the positive ion mode is shown in Figure 3.3a–c. The images obtained are strongly dependent on the level of charge compensation used. First, we can compare Figure 3.3a with Figure 3.3b. Figure 3.3a is acquired using a high electron current typically used in routine image analysis (around 1 μA), whilst Figure 3.3b (which is also shown as Figure 3.1b) is acquired using a lower but sufficient electron current of approximately 70 nA. Note that the currents given here are for reference only, since the amount of actual charge compensation delivered to the sample surface is dependent on the alignment of the electron gun and the achievable focus and differ between different instruments. With a high electron current (Figure 3.3a), a strong

intensity enhancement is observed on one side of the fibre, and the regional SIMS spectrum at this location shows strong characteristic PET secondary ions. The enhancement is caused by the charging of the sample by the electron gun, which is incident from the bottom right of the image (the direction is shown by the blue arrow on Figure 3.3a). In these experiments the electron energy is 20 eV, so electron charging may reduce the surface potential on the fibre by 20 V at most. The effects of charging on the extraction field and secondary ion trajectories are illustrated by COMSOL simulations in Figure 3.3d–f. Figure 3.3e (also shown as Figure 3.1c) shows the simulated trajectories of the secondary ions (blue) when the sample surface is not charged by either the primary ions or flood gun electrons. Figure 3.3d shows the same model but with accumulated negative charges on the surface from electron charging, such that the surface potential at the top of the fibre is –20 V in the absence of an external extraction field. For topographic samples in positive ion mode, COMSOL shows that electron charging reduces the distortion of the extraction field and increases the acceptance of secondary ions from the sides of the fibre. It is worth noting that COMSOL only provides qualitative comparison with the experimental data, rather than quantitative results, since the precise extent of charging at each electron current cannot be known. Experimentally, the intensity enhancement observed in Figure 3.3a is very strong, due to the high secondary ion yield at these locations where the primary ions are incident at near grazing incidence angles. Since the electrons are incident from the bottom right direction of the image, the enhancement is observed only on this side of the fibre where the charging is more prominent. If the electron current is increased further, eventually the other side of the fibre becomes charged sufficiently and the strong intensity enhancements can then be observed on both sides of the fibre. Clearly, for samples with topography it would be advantageous for electrons to be incident from above the sample so that localised electron charging does not occur. Such configurations have previously been developed.[10]

We can also examine the effect of not using a sufficient electron current and allowing the sample to become positively charged from the primary ion beam. The total ion image is shown in Figure 3.3c and the COMSOL simulation, assuming a charging of +50 V, is shown

in Figure 3.3f. In the positive ion mode, primary ion charging increases the curvature of the extraction field, which strongly deflects the secondary ions from the sides of the fibre and from the substrate. The observable fibre width is reduced from $|\psi| \leq 13°$ (for Figure 3.3b) to $|\psi| \leq 10°$. Primary ion charging severely affects the analysis of insulating samples and this is shown clearly in COMSOL. It is interesting to observe that, in Figure 3.3c, the substrate shadow is absent on the far left of the image. This is a geometric effect due to the primary ions being incident from the right at $\theta = 45°$ to the substrate normal. Features with a height z are projected by a distance $d = z / \tan \theta$ to the left of the true position, as explained in Chapter 2. The edge of the shadow on the substrate (green triangle on Figure 3.3c) is in fact physically adjacent to the edge of the fibre section analysed (red triangle on Figure 3.3c), and the triangles would line up if viewed from above the sample (i.e. along the direction of the substrate normal). Since the substrate to the left of the green triangle is adjacent to a section of the fibre that is not analysed by the primary ion beam, charging is not important in this region and the substrate shadow is therefore absent.

Negative ion mode

The experiment above is repeated in negative ion mode and the changes in the total ion images as the electron current is varied are observed. The total ion images acquired experimentally are shown in Figure 3.4a–d and simulation results are shown in Figure 3.4e–h. Here, the polarity of the extraction voltage is reversed, and the effects caused by sample charging are also reversed. First, the effect of electron charging is studied. In the negative ion mode, electron charging increases the distortion of the extraction field and the associated topographic field effects. The total ion image acquired with a large electron current of ~ 1.4 μA (Figure 3.4a) shows a large substrate shadow adjacent to the fibre, in agreement with the COMSOL simulation (Figure 3.4e). As the electron current is reduced (Figure 3.4b and Figure 3.4f), the sample surface ceases to be negatively charged, and the substrate shadow disappears, although the signals from the side of the fibre are still lost. The total ion image is now similar to the one obtained in the positive ion mode under a reduced electron current

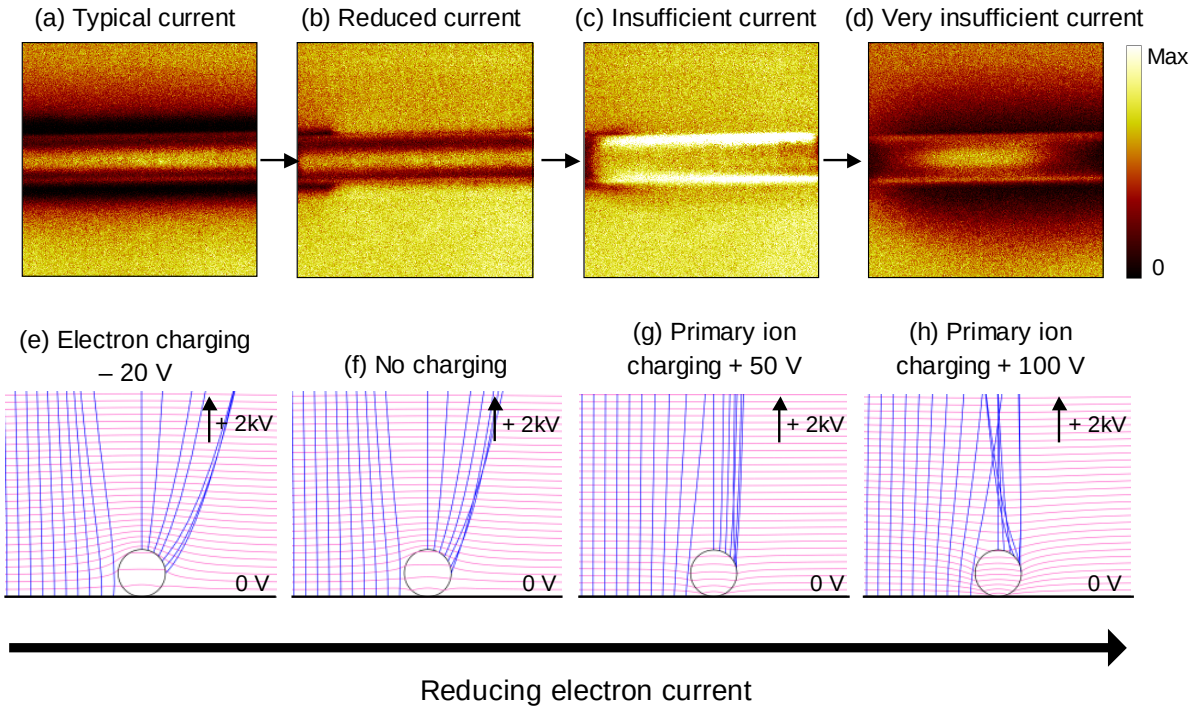

Figure 3.4 The effect of the electron current for charge compensation in the negative ion mode, using a PET fibre (diameter 100 μm) mounted on a conducting silicon substrate. (a) to (d) show the total ion images as the electron current is reduced. The images are acquired over the same area of the sample, with an electron energy of 20 eV and field of view of 500 μm × 500 μm. (f) to (h) show the corresponding COMSOL simulations along the vertical cross-section of the fibre, showing the equipotential lines of the extraction field in pink with a spacing of 20 V, and the trajectories of the secondary ions in blue.

(Figure 3.4b). The feature in the far left of the image is again caused by the geometric effect as described previously. Reducing the electron current further causes the sample to be positively charged from the primary ion beam (Figure 3.4c and Figure 3.4g). In the negative ion mode, this reduces the distortion of the extraction field significantly and allows the detection of secondary ions originating from the sides of the fibre, causing very strong intensities at these regions where the sputtering yield is high. However, if the electron current is reduced even further (Figure 3.4d and Figure 3.4h), the fibre eventually becomes so severely charged that field effects dominate again, resulting in significant loss of secondary ion intensities. The intensities on the fibre reduce significantly towards the edges of the image

in Figure 3.4d due to the large difference in charging between the analysed and non-analysed sections of the fibre.

Although Figure 3.4c appears to minimise the field distortion and allow the whole available fibre surface to be studied, in practice, it is extremely difficult to adjust the level of primary ion charging precisely. The level of charging is often a function of analysis time and it may not be possible to achieve an equilibrium level. It is not therefore recommended for analysts to use this method to reduce topography field effects. It is also worth noting that, for the same extent of field effects, the observable fibre width appears to be larger in the negative ion mode compared to the positive ion mode. This can be seen when we compare Figure 3.3b and Figure 3.4b. The reason is that the negative ion spectrum is strongly dominated by atomic secondary ions, such as H^- and O^-, whereas the positive ion spectrum is dominated by organic secondary ions characteristic of PET, for example $C_xH_yO_z^+$. In Chapter 2, it was found that the observable width is larger for atomic secondary ions, which have higher kinetic energies than organic or cluster secondary ions, which explains the observation here.

The important result from this study is that the level of charge compensation significantly affects the image obtained during the SIMS analysis of topographic insulating samples. Under typical operating conditions, insulating samples are negatively charged by the incident flood gun electrons. This reduces topographic field effects in the positive ion mode but increases the topographic field effects in the negative ion mode. Strong field effects also occur if the sample is allowed to be positively charged by the primary ion beam. It is also observed that, at very high electron currents, the flood gun electrons are deflected by the negatively charged insulating sample causing strong electron damage elsewhere. From these results, it is clear that for insulating samples with topography, a careful control of the electron current is needed for adequate charge compensation, repeatable images and to minimise electron damage. Analysts should note that it may not be possible to acquire repeatable images and keep to the recommended electron dose limit of 6×10^{18} electrons/m^2 for low damage.[9]

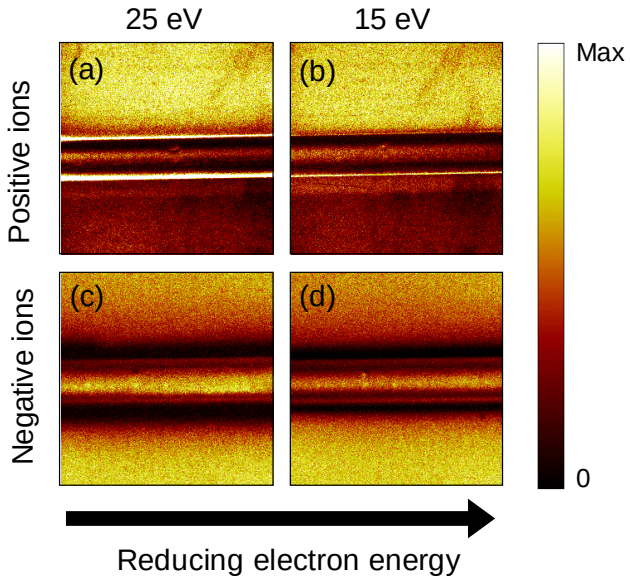

Figure 3.5 The effect of changing the electron energy for charge compensation, for a PET fibre (diameter 100 μm) mounted onto a conducting silicon wafer. (a) and (b) show the total ion images in the positive ion mode, (c) and (d) show the total ion images in the negative ion mode. The field of view is 500 μm × 500 μm and the images are acquired over the same area of the sample.

3.4 Optimising parameters

In this section several methods to reduce topographic field effects and obtain more reproducible images for insulating samples are outlined.

3.4.1 Reducing the effect of charging

In Section 3.3.3, sample charging by the flood gun electrons is discussed. The poor reproducibility of the total ion images is caused by the changing surface potential difference between the charged insulating surface (fibre) and the grounded conducting surface (substrate). This effect has been explored for a flat surface in a separate study by Shard *et al.*[11] Fortunately, the extent of electron charging can be controlled easily using the electron energy. Figure 3.5 shows the total ion images for the PET fibre using different electron energies, for positive ions (Figure 3.5a–b) and negative ions (Figure 3.5c–d). The electron current is

approximately 1 μA for both electron energies. In the positive ion mode, electron charging reduces the extent of the topographic field effects, and strong intensities can be observed at the sides of the fibre with an electron energy of 25 eV (Figure 3.5a). The bright sides disappear at a lower electron energy of 15 eV (Figure 3.5b). In the negative ion mode, electron charging increases the extent of the topographic field effects, and a large substrate shadow is observed (Figure 3.5c). The shadow size is reduced using a lower electron energy of 15 eV (Figure 3.5d). A lower electron energy therefore reduces the discrepancies between positive and the negative ion images by reducing the differential charging between the insulating and the conducting surfaces. It is therefore recommended that a lower flood electron energy should be used when analysing insulating samples adjacent to conducting surfaces, for example for insulating fibres mounted onto a conducting substrate, in agreement with Reference 11.

Differential electron charging can also be reduced by mounting an insulating sample onto a flat, insulating substrate, so that both the sample and the substrate acquire a similar negative surface charge under electron flood gun bombardment. Figure 3.6 shows the total ion images obtained for the PET fibre mounted onto a clean glass substrate. Again, the images are acquired using electron energies of 25 or 15 eV with an electron current of ~ 1 μA. The COMSOL simulation of this experimental configuration is given in Figure 3.7a and discussed later. Figure 3.6 shows that repeatable secondary ion images are now obtained regardless of the electron energy or the secondary ion polarity. It is therefore recommended that if possible, insulating samples should be mounted onto insulating substrates to improve repeatability of the images for different charge compensation settings.

Sometimes differential charging can also occur within an insulating sample, causing different field effects on different areas of the surface. This can be a consequence of the position of the electron flood gun. For the fibre sample, more electrons reach one side of the fibre compared to the other, resulting, in our arrangement, in a top-down asymmetry in the ion images. The effect is observed in Figure 3.3a. The asymmetry is significantly worse when a ‘sawtooth’

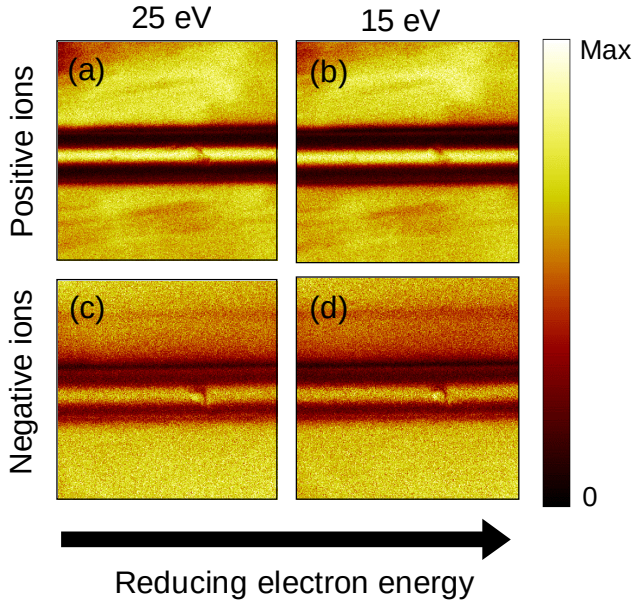

Figure 3.6 The effect of changing the electron energy for charge compensation, for a PET fibre (diameter 100 μm) mounted onto an insulating glass slide. (a) and (b) show the total ion images in the positive ion mode, (c) and (d) shows the total ion images in the negative ion mode. The field of view is 500 μm × 500 μm and the images are acquired over the same area of the sample.

primary ion raster is used – the primary ion charging becomes severe and the far side of the fibre cannot be charge compensated adequately. A random primary ion raster is therefore recommended if it is available. This type of differential charging may also be reduced by configuring the instrument so that the flood gun electrons are incident from directly above the sample.[10]

3.4.2 Reducing field effects in the absence of charging

So far the discussions have focused on the effects of charging for fibres mounted onto flat substrates. However, even in the absence of sample charging by electrons or primary ions, the extraction field is distorted by the presence of the sample (as discussed in Section 3.3.2), resulting in the loss of signal from the sides of the fibres due to the deflection of secondary ions. In Chapter 2, the use of a lower extraction voltage or an extraction delay has been shown to considerably reduce the extent of field effects for conducting wires, resulting in a larger observable width and reduced substrate shadow. However, these are found not to be generally

applicable to insulating samples. A lower extraction voltage is found to exacerbate the effects of electron charging, since a charge build-up of –20 V is more significant for an extraction voltage of 500 V compared to 2000 V. Furthermore, little improvement can be made using an extraction delay, where the extraction voltage is switched on several tens of nanoseconds after the sputtering event, so that the secondary ions may drift away from the sample surface into a region where the extraction field would be less distorted by the topographic sample. For insulating samples, the secondary ions do not drift freely during extraction delay. Rather, they are under the effect of an unspecified electric field caused by surface charges on the insulating sample, as well as a bias of –30 V applied to the analyser extraction cone to repel the entry of flood gun electrons. This results in a significant loss of secondary ion signals, especially for negative ions which are repelled from the analyser cone. Extraction delay is therefore unsuitable for insulating samples.

Another method to reduce the curvature of the extraction field is to use alternative sample mounting methods. Here, COMSOL is used to compare different sample mounting schemes for insulating fibres in the absence of sample charging. Figure 3.7a shows the fibre mounted onto a thick glass substrate. The curvature of the extraction field around the fibre surface and the resulting ion trajectories are very similar to Figure 3.1c, which shows the same fibre mounted on a conducting substrate. Little improvement in topographic field effects is therefore expected from such a configuration. Figure 3.7b shows fibres mounted in a close packed fashion on a conducting substrate. This substantially reduces topographic field effects, and an additional benefit is that the analysis is not complicated by the presence of the substrate. The disadvantages are that this method is time consuming practically, requires a number of fibre sections and the availability of signal from the sides of the fibre may be limited due to close proximity of another sample. Figure 3.7c shows fibres suspended in space using an aperture which is grounded, above a grounded backplane at infinite distance. This is a simple method and there is a good improvement to the topographic field effects. Again, the analysis is not complicated by the substrate. The disadvantage is that the extraction field and surface potential cannot easily be predicted, as it depends on the size and placement of the

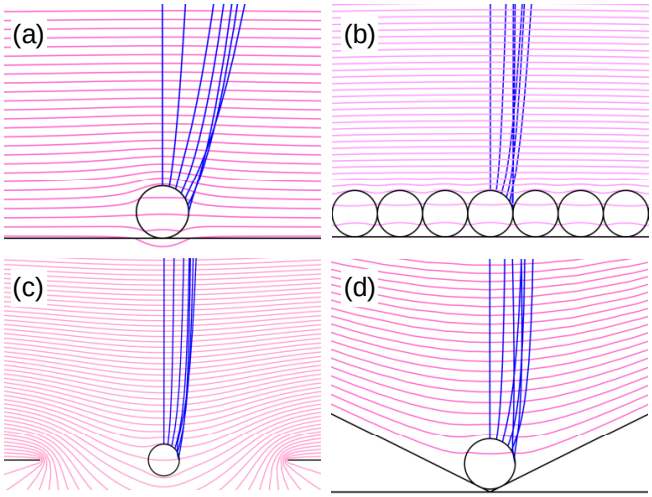

Figure 3.7 COMSOL simulations of the effect of alternative sample mounting methods on the trajectories of secondary ions emitted from the fibre surface, for a fibre with diameter 100 μm and dielectric constant of ε_r = 3.0. The extraction voltage is –2000 V and the extraction gap is 1.5 mm. The equipotential lines of the extraction field are shown in pink with a spacing of 20 V and the trajectories of the secondary ions are shown in blue. (a) Fibre mounted onto a flat insulating substrate with a dielectric constant of ε_r = 5.0 (similar to glass). (b) Fibres mounted in a close packed fashion on a conducting substrate. (c) Fibre mounted suspended in space using an aperture. (d) Fibre mounted onto a conducting sample holder with a V-shaped groove as described in Chapter 2.

fibre with respect to the aperture, and field effects may vary along the length of the fibre. Therefore repeatability and reproducibility may be an issue using this method. Finally, Figure 3.7d shows the fibre mounted on a simple conducting sample holder with a V-shaped groove, which was shown to be helpful for conducting wires. The simulation shows the same design used in Chapter 2, where the angle of the groove is 30° to the horizontal and the groove depth is 450 μm. The groove distorts the local electric field so that secondary ions emitted from the side of the fibre are deflected towards the analyser, thus it acts like a simple focusing lens for the ions. The method also results in the smallest surface potential difference between the top and sides of the fibre, which improves the mass resolution for fibre secondary ions. Using these COMSOL simulations, the V-groove sample holder is recommended for the best reduction of topographic field effects for fibres combined with simple mounting and easy reproducibility. If such a configuration is not available, then the analysts will need to make a compromise depending on the aim of the analysis. The close packed method is expected to

give good reproducibility and performance but is time consuming. Mounting on a flat substrate gives the best reproducibility but the topographic field effects are worse, and using an open aperture is very quick but the reproducibility can be poor.

3.5 Conclusions and recommendations

Using a fibre model system, a detailed study is conducted focusing on two key issues for the analysis of insulating samples with topography – topographic field effects caused by the penetration of the extraction field into the sample, and the effect of charge compensation. From this, the following recommendations are given for practical analysis.

1. A larger reflector voltage (or acceptance energy) should be used to maximise the acceptance of secondary ions from different areas of the sample surface, since topographic samples have a non-uniform surface potential. Guidance for this is given in Section 3.3.1.

2. Careful control of the electron current and electron energy for charge compensation is required to obtain repeatable images and to minimise electron damage.[9] Under typical conditions, insulating samples are charged by flood gun electrons. This reduces topographic field effects for positive secondary ions but exacerbates topographic field effects for negative secondary ions, resulting in poor reproducibility of images.

3. The effects of electron charging can be reduced by using a lower electron energy or by mounting insulating samples adjacent to insulating surfaces. For example, fibres can be mounted in good contact with a flat insulating substrate using the method in Figure 2.1.

4. Differential charging of the sample can be reduced using a ‘random’ primary ion raster and by configuring the instrument so that the flood gun electrons are incident from directly above the sample.

5. Alternative sample mounting strategies may be employed to reduce topographic field effects. Some methods for fibres are discussed in Section 3.4.2, for example, mounting fibres in a close packed fashion or in a V-groove sample holder (Figure 3.7) is expected to give improved results.

References

1 S. Rangarajan and B. J. Tyler, Journal of Vacuum Science & Technology A **24,** 1730 (2006).

2 L. A. McDonnell, T. H. Mize, S. L. Luxembourg, S. Koster, G. B. Eijkel, E. Verpoorte, N. F. de Rooij, and R. M. A. Heeren, Analytical Chemistry **75,** 4373 (2003).

3 B. Hagenhoff, Mikrochimica Acta **132,** 259 (2000).

4 S. J. Pachuta, Applied Surface Science **231-2,** 217 (2004).

5 R. Avci, A. M. Hagenston, N. L. Equall, G. S. Groenewold, G. L. Gresham, and D. A. Dahl, Surface and Interface Analysis **27,** 789 (1999).

6 J. Schwieters, H. G. Cramer, T. Heller, U. Jurgens, E. Niehuis, J. Zehnpfenning, and A. Benninghoven, Journal of Vacuum Science & Technology a-Vacuum Surfaces and Films **9,** 2864 (1991).

7 Tables of Physical & Chemical Constants (16th edition 1995). 2.6.5 Dielectric properties of materials. Kaye & Laby Online. Version 1.0 <www.kayelaby.npl.co.uk> (2005).

8 F. M. Green, I. S. Gilmore, and M. P. Seah, Journal of the American Society for Mass Spectrometry **17,** 514 (2006).

9 I. S. Gilmore and M. P. Seah, Applied Surface Science **187,** 89 (2002).

10 I. S. Gilmore and M. P. Seah, Surface and Interface Analysis **23,** 191 (1995).

11 A. G. Shard J. L. S. Lee, I. S. Gilmore and S. Jerome, presented at the 6th European Workshop on Secondary Ion Mass Spectrometry, Muenster, Germany, September 2008. “Lateral Charging Effects in SIMS Imaging”

Chapter 4 – Introduction to multivariate data analysis

4.1 Introduction

Multivariate analysis was developed in the 1950s with its roots founded in the study of behavioural science in the 1930s. It is now widely used in analytical chemistry to provide identification and quantification for a range of spectroscopic techniques.[1] Multivariate analysis involves the use of simultaneous statistical procedures for two or more variables in a data set. An essential aspect of multivariate analysis is the statistical study of the dependence (covariance) between different variables. By summarising the data using a small number of statistical variables, the interpretation of complex data sets involving a large number of dependent variables can quickly be simplified. Multivariate analysis has numerous advantages over traditional (manual) analysis. It provides an objective and statistically valid approach using all available information in a data set. The need for manual identification and selection of key peaks and features for analysis is eliminated or significantly reduced, thereby reducing the need for *a priori* knowledge about the system under study and minimising the potential for bias. By correlating data across a number of variables, an improved signal to noise ratio can be obtained. Multivariate analysis can also be fast and automated. A typical analysis takes only a few minutes on a modern desktop computer, and therefore it has potential for on-line analysis of real-time processes.

Multivariate analysis has been used for a number of years in surface analysis, most notably in the techniques of secondary ion mass spectrometry (SIMS), X-ray photoelectron spectroscopy (XPS) and Raman spectroscopy, as the raw data obtained from these techniques are intrinsically multivariate in nature. For example, in XPS, the intensities on more than one variable (i.e. binding energy) are recorded during each measurement, whereas in time-of-flight SIMS (ToF-SIMS) a complete and detailed mass spectrum, containing detected ion intensities over a million mass channels, can be obtained. Multivariate methods have been

applied successfully to the characterisation and quantification of a variety of materials including inorganic materials,[2-4] polymers,[5,6] polymer additives,[7] organic thin films,[8-10] proteins,[11-16] self-assembled monolayers[17] and bacteria samples.[18] Various studies have also been carried out on the comparison of different multivariate analysis methods[19,20] and the effect of data preprocessing, such as mean centering and normalisation.[20-22] Recently, Keenan *et al* proposed a new data preprocessing method that provides scaling for data whose noise is dominated by Poisson counting statistics.[23] This has been shown to improve noise rejection and chemical characterisation when applied prior to principal component analysis (PCA) and multivariate curve resolution (MCR).[24-26] The dramatic growth in the use of multivariate analysis in SIMS in recent years reflects the increased power and throughput of modern instruments, and the increasing requirements for fast, robust methods of data analysis. This chapter provides an introduction to the research described in Chapters 5 and 6 of this thesis. A brief overview is given on multivariate methods for the analysis of SIMS data, followed by the theory and concepts behind two popular factor analysis methods for exploratory analysis – PCA and MCR, which form the basis of the research.

4.2 Overview of multivariate methods

A review of the 9 most popular multivariate methods for the identification, quantification and classification of SIMS data, highlighting the objectives, assumptions and validity of each method, can be found in Reference 27. Figure 4.1 shows the typical questions an analyst may ask when confronted with a data set. Before undertaking any data analysis, it is crucial to have a clear aim and hypothesis so that an appropriate multivariate method may be chosen. Broadly speaking, multivariate analysis methods fall into the following three categories: exploratory analysis and identification, calibration and quantification, and classification and clustering.

4.2.1 Exploratory analysis and identification

Multivariate methods are used to examine the data and identify or highlight important features, without *a priori* knowledge of what the analyst is searching for. In case of SIMS, the

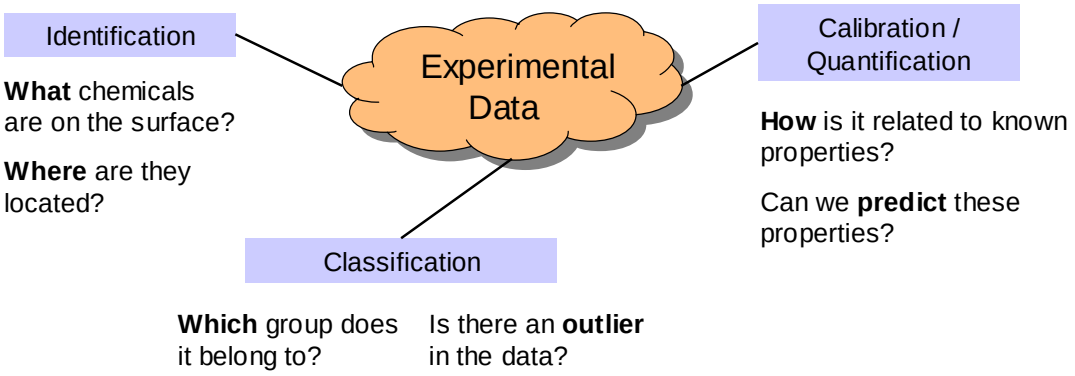

Figure 4.1 Typical questions involved in the analysis of data obtained from surface analysis. These can be broadly split into three categories.

typical questions are: what chemicals are on the surface and what are the main similarities and differences between different samples? Factor analysis methods, including PCA, MCR and maximum autocorrelation factors (MAF), are the most widely used for the exploratory analysis of SIMS data. The principles behind factor analysis will be discussed in Section 4.3. A popular application of PCA is the characterisation of proteins on surfaces.[11-16] Since all proteins consist of identical amino acids arranged in different sequences, the SIMS spectra of different proteins are similar, with main differences being the relative intensities of amino acid related fragment peaks. Combined with the extreme surface sensitivity of SIMS, PCA has been shown to discern small but important changes in spectra which reflect changes of protein conformation and orientation in vacuum.[14] MCR is most commonly applied to the analysis of SIMS images for the identification and localisation of chemical components on surfaces.[19,26,28-30]

4.2.2 Calibration and quantification

Multivariate methods also can be used to analyse the relationship between two or more sets of independent measurements made on the same samples.[31,32] A predictive model can be computed which allows specific surface properties to be predicted using only the SIMS spectra, provided that a suitable calibration data set is available. Calibration and quantification methods include multivariate regression methods, such as principal component regression (PCR) and partial least squares regression (PLS). PLS has been applied to correlate SIMS

spectra with data from other surface analysis techniques, including XPS.[6,11,17] PLS is also useful in studying the relation between surface chemistry and resulting surface property, for example, to predict water contact angles of materials using their ToF-SIMS spectra.[33-35]

4.2.3 Classification and clustering

Multivariate methods can be used to classify a sample into one of a number of possible groups of materials that exhibit similar characteristics. Multivariate methods provide a powerful route to this type of classification and interpretation of spectral information from surface analytical techniques, either using predetermined groups or via unsupervised clustering. Methods in this category include discriminant function analysis (DFA), hierarchical cluster analysis (HCA) and artificial neural networks (ANN). Although classification and clustering methods have not been yet widely applied to SIMS data, there are several successful applications including the discrimination of similar strains of bacteria using DFA[18,36] and the use of an ANN for pattern recognition of static SIMS spectra and classification using library data.[37]

4.3 Factor analysis

In this section, a brief overview will be given on the theory and concepts behind two popular factor analysis methods for exploratory analysis – PCA and MCR. It is worth noting that multivariate analysis should not be treated as a 'black box' approach to data analysis. An understanding of the theory, assumption and validity of each method is vital in obtaining a valid, physical interpretation of analysis results.

Factor analysis[1] is a broad field that has been in continual development for over 70 years, and today has an extensive range of applications in fields such as spectroscopy,[38] remote sensing,[39] social sciences[40] and economics.[41] It is a technique for reducing matrices of data to their lowest meaningful dimensionality by describing them using a small number of factors, which are directions in the data space that reflect useful properties of the data set. This is

equivalent to a transformation so that the new basis (or 'factors') used to describe the data are a linear combination of the original variables.

4.3.1 The factor analysis model

A typical factor analytical model containing N factors can be written in matrix notation as

$$\mathbf{X} = \mathbf{TP}' + \mathbf{E} \quad \Leftrightarrow \quad \mathbf{X} = \sum_{n=1}^{N} \mathbf{t}_n \mathbf{p}_n' + \mathbf{E} \quad \Leftrightarrow \quad x_{ik} = \sum_{n=1}^{N} t_{in} p_{nk} + e_{ik} \tag{4.1}$$

where letters in upper case, bold font, denote matrices and letters in the lower case, bold font, denote vectors. Letters in unbold, italic font, denote scalars. The matrix transpose is denoted by an apostrophe. All indices are taken to run from one to their capital versions, e.g. i = 1, 2, … I. **X** is the 'data matrix' and is an $I \times K$ matrix containing experimental data obtained for I samples over K variables, after suitable data preprocessing. **P** is the 'loadings matrix', with dimensions $K \times N$, whose rows are the projection of the factors onto the variables. **T** is called the 'scores matrix' and is an $I \times N$ matrix whose rows are the projections of the samples onto the factors. **E** is the error between the factor analysis model and the experimental data and is called the 'residuals matrix'. It has the dimensions of $I \times K$, and is usually assumed to contain noise only.

Different factor analysis techniques differ in the way in which the factors are extracted. Rotational and scaling ambiguities mean that there are no unique solutions to Equation 4.1. By keeping only N factors in the model, we can subtract the residuals matrix from the data and construct a 'reproduced data matrix' $\overline{\mathbf{X}}$, such that

$$\overline{\mathbf{X}} = \mathbf{TP}' \approx \mathbf{X} \tag{4.2}$$

Using this, we can gauge the success of different factor analytical models based on its ability to reproduce interesting features in the data using the fewest number of factors. A detailed explanation of factor analysis may be found in Reference 1.

Term used here	Symbol	Definition	Term commonly used in PCA	Term commonly used in MCR
Factor	–	Axis in the data space of a factor analysis model, representing an underlying dimension that contributes to summarising or accounting for the original data set	Principal component	Pure component
Loadings	**p**	Projection of a factor onto the variables	Loadings, Eigenvector	Pure component spectra
Scores	**t**	Projection of the samples onto a factor	Scores, Projections	Pure component concentration

Table 4.1 The factor analysis terminology adopted in this work in relation to those commonly used in literature for different multivariate factor analysis techniques, adapted from ISO 18115-1:2010.[42]

4.3.2 Terminology

A well-defined terminology is essential for ideas and practices to be communicated clearly and accurately. As a result of its history and scope, factor analysis is laden with confusing terminology, with different names given to similar or equivalent terms depending on the technique and the field of application. For example, in PCA the loadings $\mathbf{p}_n$ and scores $\mathbf{t}_n$ associated with a particular factor n are sometimes called, collectively, a 'principal component', whereas in other cases 'principal component' is used synonymously with 'loadings' and 'eigenvector'. In MCR, 'pure component spectra' and 'pure component concentration' are often used in place of 'loadings' and 'scores', reflecting the background of the technique in spectroscopic mixture analysis. A problem may arise as the term 'components', when referred to the factors extracted mathematically in factor analysis, may be confused with real chemical components of the system. Here, the terminologies are clarified in order to ensure clarity and consistency within this thesis, and to emphasise the relationship between different multivariate analysis techniques. Only factors, loadings and scores will be referred to in this work. Table 4.1 shows the definitions of these terms, and conversion between these and the various terminologies commonly used in the literature. In close consultation with international experts, these definitions (along with other terms on

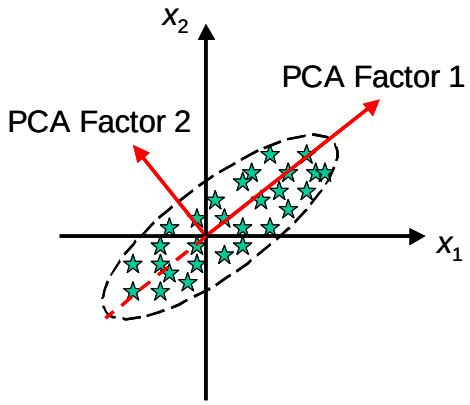

Figure 4.2 A two dimensional graphical representation of principal component analysis (PCA).

multivariate analysis) has now been incorporated into ISO standard ISO 18115-1:2010 Surface chemical analysis – Vocabulary – Part 1: General terms and terms used in spectroscopy.[42]

4.3.3 Principal component analysis

PCA is a multivariate technique for reducing matrices of data to their lowest dimensionality by describing them using a small number of orthogonal factors.[43] The goal of PCA is to extract factors, or 'principal components', that capture the largest amount of variance within the multi-dimensional data set. PCA is perhaps the most popular and widely used multivariate analysis method, with applications ranging from face recognition[44] to behavioural sciences.[45] Often, PCA is used as a first step for data reduction prior to other methods of statistical analysis.

Basic principles

A two dimensional graphical representation of PCA, applied after mean centering of the data, is shown in Figure 4.2. This shows data for 28 samples measured over two variables, x_1 and x_2. The first PCA factor describes the direction of the largest variance, or spread, of data points in the data set. The second PCA factor is the direction orthogonal (i.e. at a right angle) to the first that captures the largest remaining variation. It is obvious that PCA factors can be

interpreted as rotated axes in the data space that optimally describe the variance within the data. Using PCA, we have transformed the correlated variables x_1 and x_2 into a new basis which is uncorrelated. At this stage, two factors describe all features in the data set. However, it may be useful to assume that x_1 varies linearly with x_2, and the scatter in the data set arises only from experimental noise. It is then beneficial to discard information in PCA factor 2, so that all the relevant chemical information would be provided by the projection of the data onto PCA factor 1. In doing so, we have achieved the dimensionality reduction desired in factor analysis, and the data set, originally containing two variables, can now be described solely using one factor. This ability for PCA to transform variables into an optimal basis and achieve dimensionality reduction is extremely important in a large data set with many variables which are highly correlated, as is the case for many practical analyses.

Mathematical formulation

PCA follows the factor analysis equation (Equation 4.1). The main steps of PCA are shown in a schematic diagram in Figure 4.3. PCA factors are computed using the eigenvector decomposition of matrix **Z**, where

$$\mathbf{Z} = \mathbf{X}'\mathbf{X} \tag{4.3}$$

Here **X** is the data matrix containing experimental data, after suitable data preprocessing. If **X** is mean centered, then **Z** is called the covariance matrix and often denoted as $\mathbf{Z}_{\text{cov}}$. If **X** is auto scaled, then **Z** is referred to as the correlation matrix and often denoted as $\mathbf{Z}_{\text{corr}}$. An eigenanalysis of **Z** gives

$$\mathbf{Z}\mathbf{q}_r = \lambda_r \mathbf{q}_r \tag{4.4}$$

where $\mathbf{q}_r$ is the rth eigenvector of **Z** and λ_r is its associated eigenvalue. Due to the properties of eigenvalue decomposition of a symmetric matrix, the eigenvectors are orthonormal (i.e. orthogonal and normalised), and the eigenvalues can only have positive or zero values. At this stage the total number of non-zero eigenvectors and eigenvalues obtained is equal to R, the

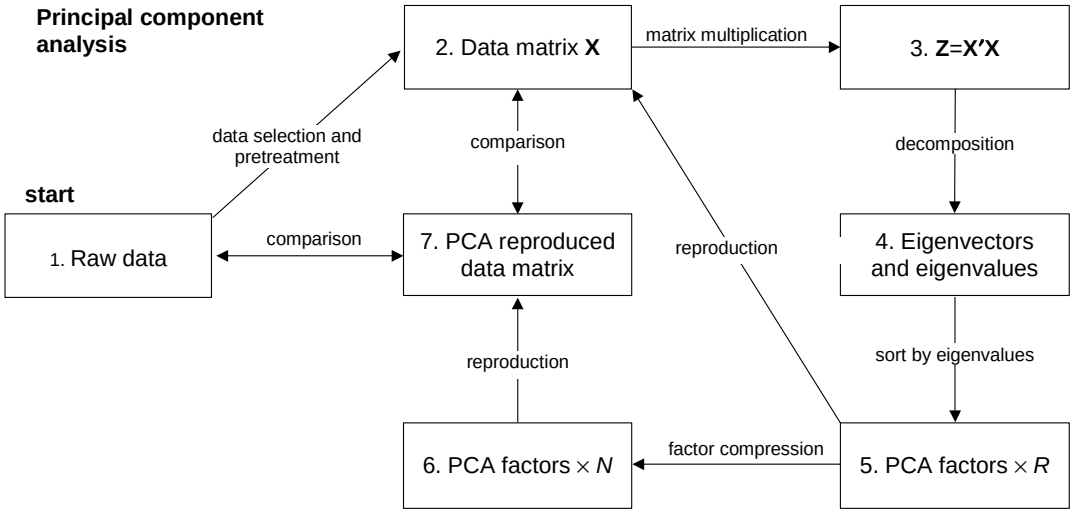

Figure 4.3 A schematic diagram illustrating typical steps in principal component analysis (PCA), after Malinowski.[1]

rank of the data matrix. Because **Z** contains information about the variances of the data within the data set, the eigenvectors are special directions in the data space that are optimal in describing the variance of the data. The amount of variance accounted for by each eigenvector is given by the eigenvalues.

PCA factors consist of the eigenvectors of **Z**, sorted in descending order by their associated eigenvalues, such that PCA factor 1 describes the direction of the largest variance and has the largest associated eigenvalue. The eigenvectors matrix **Q** is given by

$$\mathbf{Q} = \begin{pmatrix} \mathbf{q}_1 & \mathbf{q}_2 & \cdots & \mathbf{q}_R \end{pmatrix} \tag{4.5}$$

where $\mathbf{q}_r$ are column vectors of the sorted eigenvectors such that $\mathbf{q}_1$ is associated with the largest eigenvalue λ_1. To rewrite the data using the PCA factors as new basis, the scores matrix $\mathbf{T}_{\text{full}}$ is calculated to give the projections of the data onto all the factors. This can be written in matrix notation

$$\mathbf{T}_{\text{full}} = \mathbf{XQ} \tag{4.6}$$

Equation 4.6 can now be manipulated to obtain an expression for data matrix **X** by post multiplying the equation by $\mathbf{Q}^{-1}$, which is the matrix inverse of **Q**. This gives,

$$\mathbf{X} = \mathbf{T}_{\text{full}}\mathbf{Q}^{-1} \tag{4.7}$$

By comparison of Equation 4.7 with Equation 4.1, the factor analysis equation is satisfied if we set the transpose of the loadings matrix, $\mathbf{P}'_{\text{full}}$, to be equal to $\mathbf{Q}^{-1}$. However, since **Z** is a symmetrical matrix in PCA, the columns of **Q** are orthogonal and $\mathbf{Q}^{-1}$ is simply equivalent to $\mathbf{Q}'$. This gives the PCA solution to the factor analysis equation,

$$\mathbf{P}_{\text{full}} = \mathbf{Q} \tag{4.8}$$

$$\mathbf{X} = \mathbf{T}_{\text{full}}\mathbf{P}'_{\text{full}} = \sum_{n=1}^{R} \mathbf{t}_n \mathbf{p}'_n \tag{4.9}$$

At this stage, all PCA factors have been included in the factor analysis model, and the scores $\mathbf{T}_{\text{full}}$ and loadings $\mathbf{P}_{\text{full}}$ reproduce the original data matrix **X** fully. Often, it is preferable to discard higher PCA factors in order to reduce the dimensionality of the data. This is referred to as factor compression. If one assumes that variances in the data arising from *N* chemical features are greater than the variances arising from random noise, then all chemical information can be accounted for using the first *N* PCA factors. Methods to determine *N* are described in Section 4.3.5. By carrying out the summation in Equation 4.9 for the first *N* factors only, we obtain

$$\overline{\mathbf{X}} = \sum_{n=1}^{N} \mathbf{t}_n \mathbf{p}'_n = \mathbf{T}\mathbf{P}' \tag{4.10}$$

where the scores and loadings matrices **T** and **P** now contain only *N* columns for the first *N* factors. Finally, $\overline{\mathbf{X}}$ is the PCA reproduced data matrix and contains a noise-filtered version of the data matrix **X**, reconstructed using variances described in the first *N* PCA factors only. $\overline{\mathbf{X}}$ differs from the original data matrix **X** by an amount accounted for in the residuals matrix **E**,

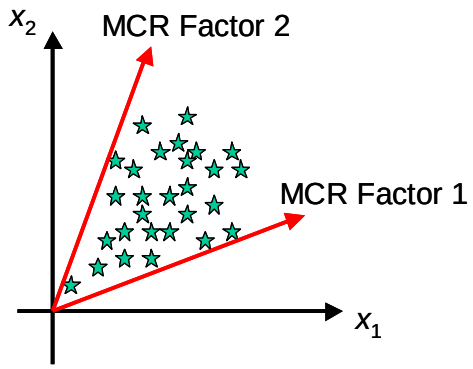

Figure 4.4 A two dimensional graphical representation of multivariate curve resolution (MCR).

i.e.,

$$\mathbf{X} = \overline{\mathbf{X}} + \mathbf{E} = \mathbf{TP}^{'} + \mathbf{E} \tag{4.11}$$

This gives the full PCA solution to the factor analysis equation.

4.3.4 Multivariate curve resolution

Multivariate curve resolution (MCR)[28,46,47] belongs to a family of methods sometimes referred to as 'self modelling curve resolution',[48] which are designed for the recovery of pure components from a multi-component mixture when little or no prior information is available. MCR uses an iterative least-squares algorithm to extract solutions to the factor analysis equation (Equation 4.1), while applying suitable constraints.

Basic principles

A two dimensional graphical representation of MCR is shown in Figure 4.4. MCR assumes that each spectrum can be described as a linear sum of non-negative contributions (MCR scores) from individual chemical components, each associated with a particular spectral profile (MCR loadings). This is true for many systems such as absorption spectroscopy, where Beer's law dictates that absorbance is proportional to concentration.[49] However, this is only a first approximation in SIMS, where many factors other than chemical composition can affect the position and the intensity of peaks, including matrix effects, topography, detector

saturation and sample degradation during analysis. This is explored in more detail in Chapters 5 and 6. Unlike PCA, MCR factors are not required to be mutually orthogonal. An advantage of MCR is the application of constraints during the solution process. By applying non-negativity constraints to the loadings and scores matrices using optimisation, MCR solutions obtained resemble SIMS spectra and chemical contributions more closely, as these must have positive values. For example, in Figure 4.4, all data points can be expressed as a positive mixture of MCR factors 1 and 2, and the factors themselves are positive combinations of the original variables x_1 and x_2. Other constraints can also be applied, including equality constraint, where using *a priori* knowledge of the system, one or more columns of the loadings or scores matrices can be fixed to known spectral or contribution profiles prior to the resolution of unknown components. MCR is also more computationally intensive than PCA and requires more analyst input prior to analysis. Importantly, unlike PCA which produces a unique solution for each data set, MCR results are not unique and are strongly dependent on initial estimates, constraints and convergence criterion. The accuracy of the resolved spectra depends on existence of samples with chemical contribution from one component only, and features from intense components can often appear in the spectral profiles resolved for weak components.[46] Therefore, careful application of MCR and interpretation of the outputs is required to obtain optimal results.

Mathematical formulation

MCR follows the factor analysis equation (Equation 4.1). The main steps of MCR are shown in a schematic diagram in Figure 4.5. In the first stage, the number of factors, N, to be resolved is determined independently, either by prior knowledge of the system or via the application of PCA and the inspection of the eigenvalue diagram (this is described in Section 4.3.5). An initial estimate of either the scores matrix, **T**, representing the contribution profiles of each component, or the loadings matrix, **P**, representing the spectra of each component, is then required as an input to the alternating least squares (ALS) algorithm. The initial estimates can be obtained in many ways, for example by the use of ‘pure variable’ detection algorithms, which find variables with contributions from single components only, or

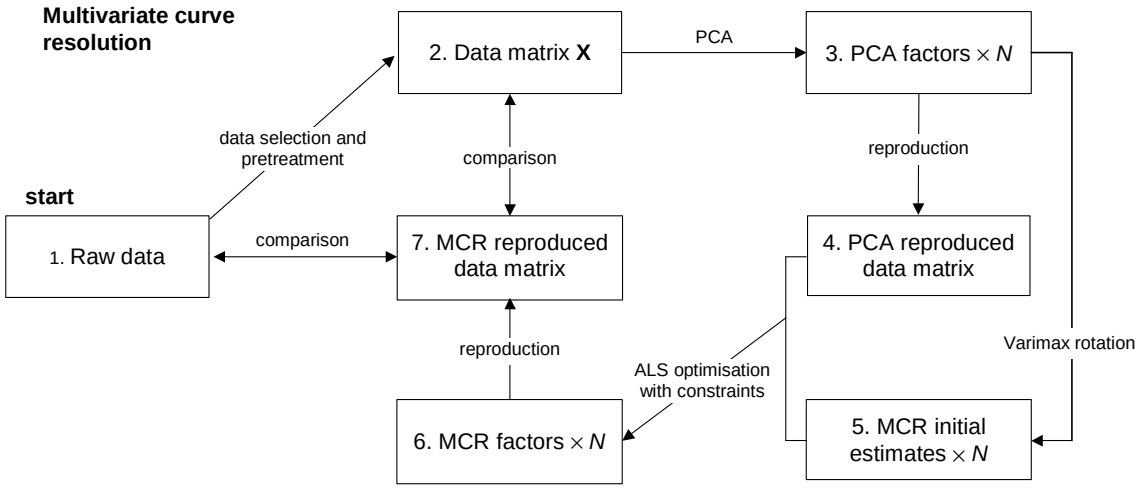

Figure 4.5 A schematic diagram illustrating typical steps in multivariate curve resolution (MCR)

by the Varimax rotation of PCA factors,[50] which simplifies PCA factors by an orthogonal rotation such that each factor only has a small number of variables with large loadings. MCR then uses an iterative algorithm to extract solutions to the factor analysis equation (Equation 4.1), by the ALS minimisation of error matrix **E**. To increase the stability of the algorithm, PCA is applied to the data as a first step and the ALS fitting is done on the noise filtered PCA reproduced data matrix, $\overline{\mathbf{X}}$, rather than the original data matrix. Assuming an initial estimate of the loadings matrix **P**, a least squares estimate of the scores matrix **T** can be obtained by

$$\mathbf{T} = \overline{\mathbf{X}}(\mathbf{P}')^{+} \tag{4.12}$$

where $(\mathbf{P}')^{+}$ is the pseudoinverse of matrix $\mathbf{P}'$. A new estimate of the loadings matrix **P** can then be obtained

$$\mathbf{P}' = \mathbf{T}^{+}\overline{\mathbf{X}} \tag{4.13}$$

In each stage of the fitting, suitable constraints are applied to the loadings and scores matrices **P** and **T**, such as non-negativity. Finally, Equation 4.12 and Equation 4.13 are re-evaluated until **T** and **P** are able to reproduce $\overline{\mathbf{X}}$, within an error specified by the user, i.e. convergence is achieved.

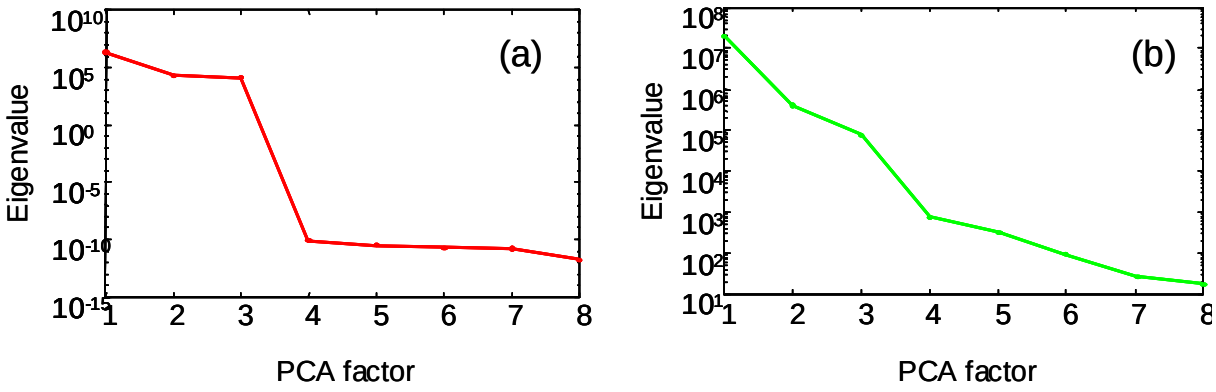

Figure 4.6 The eigenvalue diagram obtained from eight synthetic SIMS spectra produced using the library spectra of three reference materials, (a) before addition of noise (b) after addition of Poissonian noise.

4.3.5 Number of factors

The aim of factor analysis is find a small number of factors which contribute to summarising or accounting for the data. As discussed previously, PCA factors are calculated to account for the largest sources of variance in the data, and MCR factors are found to estimate contributions from individual chemical components. It is therefore important to determine an appropriate number of factors to include in a factor analysis model. If we assume that variances in the data arising from *N* chemical features are greater than the variances arising from random noise, then all chemical information can be accounted for using the first *N* PCA factors. There are many ways of determining the number of factors that one should retain. Often a combination of methods, together with the experience of the analyst, produces the best results.

Figure 4.6 shows an example simulated data set consisting of eight SIMS spectra created by mixing the library spectra of three reference materials. The eigenvalues associated with the PCA factors is plotted. Without noise (Figure 4.6a), only three factors with non-zero eigenvalues exist. This is equal to the rank of the data set and the number of independent components. Therefore only three factors are needed to explain all the features of the data set. With random, Poissonian noise, added to simulate the ion counting statistics of the SIMS

detector (Figure 4.6b), the number of factors one needs to retain is not so clear. One of the most popular ways to determine the number of factors required to sufficiently describe the data is by inspection of the eigenvalue plot in what is known as the scree test.[51] This is so-called as the plot visually resembles the scree, or debris, that accumulate at the base of a cliff. The scree test assumes that eigenvalues decrease in a steady manner for factors that describe variations arising from noise. Often, a turning point would be visible on the eigenvalue plot, where the factors describing large variances due to chemical features ("the cliff") stops and the factors describing smaller variances due to noise ("the debris") appears. Apply the scree test to Figure 4.6b, we recover that three factors are needed to describe the data. Often, the scree test is used in conjunction with the percentage of total variance captured by the N eigenvectors, which is given by

$$\%\ \text{variance captured} = \frac{\text{sum of eigenvalues up to factor } N}{\text{sum of all eigenvalues}} \times 100\% \qquad (4.14)$$

The total variance captured provides a good guidance on the number of factors one should retain in order to describe and reproduce the data satisfactorily. This will depend on the level of noise in the data set and the number of minor features, such as contamination, non-linear and other effects that one wants to include in the factor analysis model. Finally, inspection of the residuals matrix **E**, and associated lack-of-fit statistics such as Q residuals, can be helpful in determining if any meaningful structure has been excluded from the model.

4.3.6 Data preprocessing

Since all multivariate analysis techniques seek to describe the underlying structure of the data, they are sensitive to data preprocessing and transformations.[52] Data preprocessing can enhance PCA or MCR by bringing out important variances in the dataset, but because it makes assumptions about the nature of the variance in the data, it can distort interpretation and quantification and therefore needs to be applied with care.[53] Prior to multivariate analysis, data selection and binning are often performed to reduce the size of the data set. The

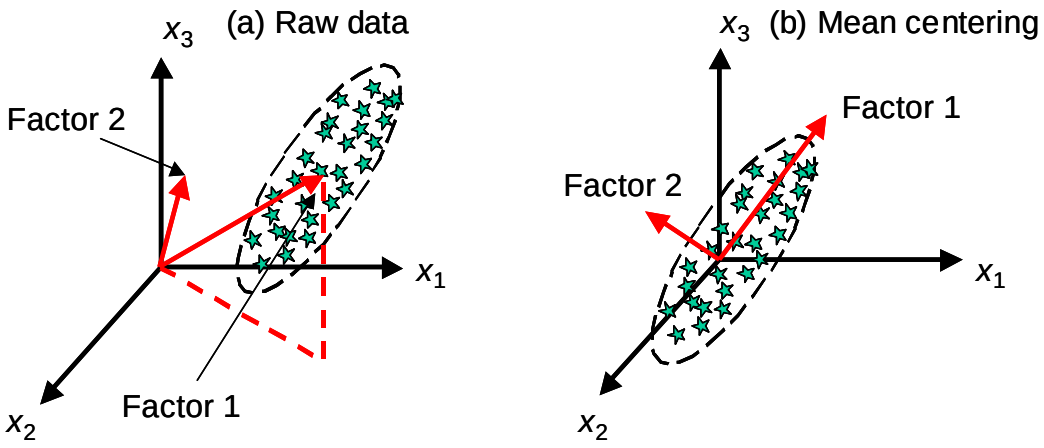

Figure 4.7 The effect of mean centering on PCA. (a) Without mean centering, PCA factor 1 goes from the origin to the centre of gravity of the data. (b) With mean centering, PCA factor 1 goes from origin and accounts for the highest variance within the data set.

following is a description of data preprocessing methods common in the field of surface analysis. The relative merits of these methods are evaluated in Chapters 5 and 6.

In **mean centering**, each variable is centered by the subtraction of its mean value across all samples. In the case of spectral data such as SIMS, this is equivalent to subtracting the mean spectrum of the data set from each sample. Mean centering is a common practice for PCA, so that the first PCA factor would go through the centre of the data rather than the origin. This allows for the effective description of the differences between samples rather than their variations from zero intensity, as can be seen in Figure 4.7. Mean centering is not applicable to MCR, as it requires positive input data for the resolution of positive loadings and scores using non-negative constraints.

In **normalisation**, the data are scaled by a constant for each sample, which could be the value of a specific variable, the sum of selected variables or the sum of all variables for the sample. This preserves the shape of the spectra data and normalisation to the total ion intensity is commonly used in SIMS, assuming chemical variances can solely be described by the relative changes in ion intensities. Normalisation therefore removes the gross variations in total ion

intensities caused by topography, sample charging, changes in primary ion dose, and other effects.

In **variance scaling**, each variable is individually divided by its variance in the data set. Variance scaling is referred to 'auto scaling' when it is followed by mean centering. Variance scaling equalises the importance of each variable, and is often used in SIMS to emphasise high mass, low fragmentation ions which often have lower intensities. However, it can be problematic for weak peaks with variations arising mostly from background signal, noise or minor contaminants, and therefore variance scaling is commonly used on a selection of strong characteristic peaks only.

In **Poisson scaling**, it is assumed that the statistical uncertainty of each variable is dominated by the counting statistics of the detector, which are Poissonian in nature.[23] This is a good approximation for SIMS raw data where the detector is operating within linearity, and Poisson scaling cannot be applied in conjunction with other data scaling methods. Poisson scaling weights the data by their estimated uncertainty, using the fact that the noise variance arising from Poisson statistics is equal to the average counted intensity. Since multivariate methods generally assume uniform uncertainty in the data, Poisson scaling has been shown to provide greater noise rejection in the multivariate analysis of SIMS data.[23,26,53] Poisson scaling thus emphasises the weak peaks which vary above the expected counting noise, over intense peaks with large variances solely accounted for using Poisson statistics. Poisson scaling is especially valuable for image data sets, which can have low counts per pixel and can therefore be dominated by Poisson noise. A detailed explanation of Poisson scaling is given in Reference 23.

In **Binomial scaling**, the data are scaled by the statistical uncertainty of each variable for data that are affected by detector saturation. It has been shown that when detector saturation is an issue and dead time correction is required, the corrected data follow a binomial distribution, and binomial scaling should be employed instead of Poisson scaling.[54] Binomial scaling

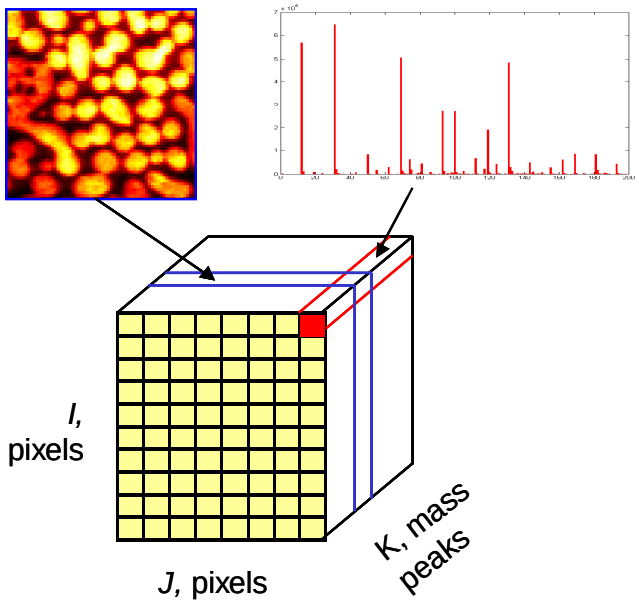

Figure 4.8 The complexity of ToF-SIMS imaging data sets, where a complete mass spectrum is recorded for each pixel, producing a large $I \times J \times K$ 'datacube'. Manual analysis is often carried out either by comparing selected ion images by eye, or comparing spectra from several selected regions of interest. With complex images where there are many unknown chemical components or features of interest, manual analysis quickly becomes impractical.

prevents highly saturated, noisy peaks from unduly influencing multivariate analysis over weaker peaks that may describe more chemically meaningful variations. A detailed explanation of binomial scaling is given in Reference 54.

4.3.7 Analysis of multivariate images

In this final section, we discuss the application of multivariate analysis to images, which is the main focus of the research in Chapters 5 and 6. With the advances in instrumentation, many spectroscopy or mass spectrometry instruments are now capable of generating images where a whole spectrum is recorded at each pixel.[55] This paves the way for the study of spatially localised features, but provides an acute problem for data analysis and interpretation due to the vast amount of information recorded. The complexity of this data is illustrated in Figure 4.8. For example, in a typical ToF-SIMS image consisting of 256 × 256 pixels, with the spectra nominally binned to unit mass up to 400 u, the data set would contain 400

individual images or 26 million data points, occupying 200 megabytes of computer memory. In addition, SIMS images often suffer from low signal-to-noise ratio, especially at high spatial resolution. This arises from the need to minimize acquisition time as well as the static limit, typically 10^{16} ions m^{-2}, imposed on the primary ion fluence to minimise surface damage by primary ions.[56] As a result, the available signal deteriorates rapidly with increased spatial resolution, and noise arising from the counting statistics of the detector becomes significant. Traditional data analysis involves the manual selection and comparison of key ion images, which is slow and requires *a priori* knowledge of the compounds on the surface. Consequently, the results may be influenced by the bias of the analyst, and small but chemically significant features can easily be overlooked, for example any localised contamination that covers only a small area on the surface of the sample.

Factor analysis methods, which take into account the whole data set, are ideal for exploring complex image data sets obtained from SIMS. The application of PCA and MCR can be easily extended to the analysis of multivariate images. A multivariate image data set contains a spatial raster of $I \times J$ pixels, where each pixel contains a complete spectrum consisting of K variables. Prior to PCA or MCR, the spatial information is simply discarded, and each pixel is treated as a separate sample. The image data cube, with dimensions of $I \times J \times K$, is 'unfolded' into a two-dimensional data matrix with dimensions $IJ \times K$, and factor analysis is then carried out to obtain scores and loadings, as described previously. On completion of the analysis, the scores matrix **T** is then 'folded' so that it has the dimensions of $I \times J \times N$, and can therefore be displayed as a series of N images, one for each of the N factors in the model. This represents significant time-saving in image analyses. Instead of having to examine K individual ion images, often a small number of factors N are sufficient to capture the main trends and variations in the image. The use of PCA and MCR for SIMS image analysis will be discussed in more detail in Chapters 5 and 6.

4.4 Conclusions

In this chapter, an introduction is given to the background and theory for some of the most common employed multivariate analysis techniques used in surface analysis. From the growing varieties of studies in the literature, it is clear that multivariate methods are powerful for the analysis of SIMS data, including spectra, images and depth profiles. Current research is actively addressing many issues and challenges in multivariate analysis, from the fundamentals such as data scaling for optimal discrimination of chemical features from noise, to practical applications such as the analysis of biological images. Terms and definitions, developed in consultation with leading industry and academic experts, has now been incorporated into ISO 18115-1 – Surface chemical analysis – Vocabulary.[42] In addition, an ISO guide to multivariate analysis, recently identified as a high priority by industry analysts, is currently in active development. These developments contribute towards providing clearer recommendations and guidelines on the application of multivariate analysis for SIMS data, which is essential to give confidence to the analysis results and ensure the widest uptake and impact of these powerful methods. With the increased power and throughput of modern analytical instruments, and the growing analytical requirements in novel research areas, for example the surface analysis of biomaterials and innovative devices, multivariate analysis is becoming an increasingly indispensable tool in extracting the maximum information from data with a fast, robust and unbiased approach.

References

1 E. R. Malinowski, *Factor Analysis in Chemistry*, 3rd ed. (John Wiley, New York, 2002).

2 S. J. Pachuta, Applied Surface Science **231-2,** 217 (2004).

3 M. L. Pacholski, Applied Surface Science **231-2,** 235 (2004).

4 V. S. Smentkowski, M. R. Keenan, J. A. Ohlhausen, and P. G. Kotula, Analytical Chemistry **77,** 1530 (2005).

5 X. V. Eynde and P. Bertrand, Surface and Interface Analysis **25,** 878 (1997).

6 D. Cossement, R. Gouttebaron, V. Cornet, P. Viville, M. Hecq, and R. Lazzaroni, Applied Surface Science **252,** 6636 (2006).

7 N. Médard, C. Poleunis, X. V. Eynde, and P. Bertrand, Surface and Interface Analysis **34,** 565 (2002).

8 M. C. Biesinger, P.-Y. Paepegaey, N. S. McIntyre, R. R. Harbottle, and N. O. Petersen, Analytical Chemistry **74,** 5711 (2002).

9 B. Tyler, Applied Surface Science **203,** 825 (2003).

10 L. Yang, Y.-Y. Lua, G. Jiang, B. J. Tyler, and M. R. Linford, Analytical Chemistry **77,** 4654 (2005).

11 S. Ferrari and B. D. Ratner, Surface and Interface Analysis **29,** 837 (2000).

12 O. D. Sanni, M. S. Wagner, D. Briggs, D. G. Castner, and J. C. Vickerman, Surface and Interface Analysis **33,** 715 (2002).

13 C. Bruuning, S. Hellweg, S. Dambach, D. Lipinsky, and H. F. Arlinghaus, Surface and Interface Analysis **38,** 191 (2006).

14 N. Xia, J. Collin, S. L. McArthur, and D. G. Castner, Langmuir **18,** 4090 (2002).

15 D. J. Graham, M. S. Wagner, and D. G. Castner, Applied Surface Science **252,** 6860 (2006).

16 M. S. Wagner and D. G. Castner, Langmuir **17,** 4649 (2001).

17 M. Von Gradowski, M. Wahl, R. Förch, and H. Hilgers, Surface and Interface Analysis **36,** 1114 (2004).

18 J. S. Fletcher, A. Henderson, R. M. Jarvis, N. P. Lockyer, J. C. Vickerman, and R. Goodacre, Applied Surface Science **252,** 6869 (2006).

19 B. J. Tyler, Applied Surface Science **252,** 6875 (2006).

20 B. J. Tyler, G. Rayal, and D. G. Castner, Biomaterials **28,** 2412 (2007).

21 B. T. Wickes, Y. Kim, and D. G. Castner, Surface and Interface Analysis **35,** 640 (2003).

22 M. S. Wagner, D. J. Graham, B. D. Ratner, and D. G. Castner, Surface Science **570,** 78 (2004).

23 M. R. Keenan and P. G. Kotula, Surface and Interface Analysis **36,** 203 (2004).

24 J. A. T. Ohlhausen, M. R. Keenan, P. G. Kotula, and D. E. Peebles, Applied Surface Science **231-2,** 230 (2004).

25 V. S. Smentkowski, J. A. Ohlhausen, P. G. Kotula, and M. R. Keenan, Applied Surface Science **231-2,** 245 (2004).

26 M. S. Wagner, D. J. Graharn, and D. G. Castner, Applied Surface Science **252,** 6575 (2006).

27 J. L. S. Lee and I. S. Gilmore, in *Surface Analysis – The Principal Techniques*, 2nd ed., edited by J. C. Vickerman and I. S. Gilmore (Wiley, Chichester, 2008), p. 563.

28 N. B. Gallagher, J. M. Shaver, E. B. Martin, J. Morris, B. M. Wise, and W. Windig, Chemometrics and Intelligent Laboratory Systems **73,** 105 (2004).

29 V. S. Smentkowski, S. G. Ostromiski, E. Braunstein, M. R. Keenan, J. A. T. Ohlhausen, and P. G. Kotula, Analytical Chemistry **79,** 7719 (2007).

30 V. S. Smentkowski, S. G. Ostrowski, F. Kollmer, A. Schnieders, M. R. Keenan, J. A. Ohlhausen, and P. G. Kotula, Surface and Interface Analysis **40,** 1176 (2008).

31 P. Geladi and B. R. Kowalski, Analytica Chimica Acta **185,** 1 (1986).

32 S. Wold, M. Sjostrom, and L. Eriksson, Chemometrics and Intelligent Laboratory Systems **58,** 109 (2001).

33 A. J. Urquhart, M. Taylor, D. G. Anderson, R. Langer, M. C. Davies, and M. R. Alexander, Analytical Chemistry **80,** 135 (2008).

34 L. Yang, A. G. Shard, J. L. S. Lee, and S. Ray, Surface and Interface Analysis **42,** 911 (2010).

35 M. Taylor, A. J. Urquhart, D. G. Anderson, R. Langer, M. C. Davies, and M. R. Alexander, Surface and Interface Analysis **41,** 127 (2009).

36 R. M. Jarvis and R. Goodacre, Analytical Chemistry **76,** 40 (2004).

37 I. S. Gilmore and M. P. Seah, NPL Report CMMT(D)268 (2000).

38 P. B. Harrington, P. J. Rauch, and C. Cai, Analytical Chemistry **73,** 3247 (2001).

39 R. Larsen, Journal of Chemometrics **16,** 427 (2002).

40 J. Stevens, *Applied Multivariate Statistics for the Social Sciences* (Lawrence Erlbaum Associates, New Jersey, 2001).

41 R. S. Tsay, in *Analysis of Financial Time Series* (John Wiley, New York, 2001), p. 335.

42 ISO 18115-1 Surface chemical analysis - Vocabulary - Part 1: General terms and terms used in spectroscopy, International Organization for Standardization, Geneva, Switzerland

43 I. T. Jollife, *Principal Component Analysis*, 2nd ed. (Springer-Verlag, New York, 2002).

44 M. Turk and A. Pentland, Journal of cognitive neuroscience **3,** 71 (1991).

45 A. Beuzen and C. Belzung, Physiology & behavior **58,** 111 (1995).

46 A. De Juan and R. Tauler, Analytica Chimica Acta **500,** 195 (2003).

47 A. de Juan and R. Tauler, Critical reviews in analytical chemistry **36,** 163 (2006).

48 J. H. Jiang, Y. Liang, and Y. Ozaki, Chemometrics and Intelligent Laboratory Systems **71,** 1 (2004).

49 R. Tauler, A. Smilde, and B. Kowalski, Journal of Chemometrics **9,** 31 (1995).

50 H. F. Kaiser, Psychometrika **23,** 187 (1958).

51 R. B. Cattell, Multivariate behavioural research **1,** 245 (1966).

52 S. N. Deming, J. A. Palasota, and J. M. Nocerino, Journal of Chemometrics **7,** 393 (1993).

53 J. L. S. Lee, I. S. Gilmore, and M. P. Seah, Surface and Interface Analysis **40,** 1 (2008).

54 M. R. Keenan, V. S. Smentkowski, J. A. Ohlhausen, and P. G. Kotula, Surface and Interface Analysis **40,** 97 (2008).

55 P. Geladi and H. Grahn, *Multivariate Image Analysis* (John Wiley, Chichester, 1996).

56 I. S. Gilmore and M. P. Seah, Surface and Interface Analysis **24,** 746 (1996).

Chapter 5 – Quantification and methodology issues in multivariate analysis of ToF-SIMS data for mixed organic systems

5.1 Introduction

Time-of-flight secondary ion mass spectrometry (ToF-SIMS) data sets contain vast amounts of information and pose huge challenges for data interpretation. Due to the complexity of ToF-SIMS data sets, multivariate methods such as principal component analysis (PCA) and multivariate curve resolution (MCR) are often employed in data analysis.[1] An introduction to multivariate analysis methods for ToF-SIMS data is given in Chapter 4. Despite advances and the widespread studies in the literature, the uptake of the techniques into general industrial analysis has been slow. This is not to say that industry analysts are not proficient in multivariate analysis; on the contrary, they are among the most expert of multivariate analysis users. Rather, in the context of all industry analysis by SIMS the use of multivariate methods is not routine and is far from fulfilling its potential. There are several reasons for this. Firstly, multivariate analysis is associated with a steep learning curve. For many scientists, there have been significant ambiguities, confusion in terminology and jargon, low confidence in the results, and a need for an improved understanding of basic and practical aspects.[2] Secondly, there is widespread confusion over the most appropriate choice of multivariate technique for each application. In particular, the application of different data preprocessing methods often leads to major inconsistencies, and therefore reliable guidance is needed for practical analysts. This situation needs resolution, since the procedures are well established mathematically and can be extremely helpful for many analytical situations. Thirdly, analysts need improved access to reliable multivariate analysis software with clear guidance on its use and regimes of validity. A significant issue is the export of experimental data from the instrument format into separate software packages for multivariate analysis, which can be slow and cumbersome. The use of the ISO Standard Data Transfer Format (SDTF) provides a solution to this problem.[3]

The work described in this chapter aims to provide clear guidance on the use of multivariate methods for the quantification and identification of organic materials by ToF-SIMS. The study focuses on a simple model system consisting of an immiscible polymer blend, poly(vinyl chloride) (PVC) – polycarbonate (PC), used in a previous study by Gilmore *et al.* on ToF-SIMS and AFM quantification issues.[4] Phase separation occurs at the surface and distinctive domains can be seen in the images. Two of the most popular multivariate methods, PCA and MCR, are applied to quantify the surface area of each phase and evaluate the effects of four different data preprocessing methods (no scaling, normalisation, variance scaling and Poisson scaling). This highlights significant issues and challenges in the quantitative multivariate analysis of mixed organic systems, including the discrimination of chemically significant features from experimental noise, the resolution of weak chemical contributions and potential bias introduced by data preprocessing. The methodology developed using this simple system is validated using a complex simulated image of a polymer blend, composed of two structurally similar polymers, poly(methyl methacrylate) (PMMA) and poly(ethyl methacrylate) (PEMA). Using these results, recommendations are given for analysts on the optimum use of multivariate analysis and selection of the most appropriate methods. The methods developed here will be applied and extended to study a complex hair treatment relevant to industry in Chapter 6.

5.2 Experimental

Sample preparation and the acquisition of SIMS data was performed by Prof Ian Gilmore (National Physical Laboratory) as part of the previous study.[4] The experimental details are as follows. Polymer blends of 50% by weight pure poly(vinyl chloride) (PVC) and 50% by weight pure polycarbonate (PC), totaling 300 mg, both from Goodfellow Cambridge Ltd. (Huntingdon, UK), were dissolved in 25 ml of tetrahydrofuran and cast freely from solution onto carefully cleaned Si wafers under normal laboratory conditions. Static SIMS analyses were made using an ION-TOF IV instrument (ION-TOF GmbH, Münster, Germany) of single-stage reflectron design.[5] Negative ion images of the PVC–PC polymer blend were obtained using a high-resolution Ga^+ focused liquid metal ion gun, with its beam incident at

45° to the surface normal. The ion beam was operated at 25 keV energy with a spot size of approximately 300 nm. Images were acquired with a 256 × 256 pixel raster and a field of view of 50 μm × 50 μm. Charge compensation was effected by low-energy (20 eV) electrons provided by a flood gun mounted at an angle of 57° to the sample normal. Further information on the sample can be found in the previous study from which the data were obtained.[4] For the simulated SIMS image in Section 5.4, data from another previous study (unpublished) was used, which consists of positive ion spectra of poly(methyl methacrylate) (PMMA) and poly(ethyl methacrylate) (PEMA) acquired using Cs^+ primary ion beam at 10 keV, mounted at 45° to the surface normal.

All calculations were performed using Matlab v7.2 (The MathWorks, Inc., Natwick, MA, USA). PCA was performed using PLS Toolbox v3.5 (Eigenvector Research, Inc., Wenatchee, WA, USA), with MIA Toolbox v1.0 add-on (Eigenvector Research) for multivariate image analysis. MCR was performed using a freely available MCR-ALS Graphic User-Friendly Interface 1.0.0 Toolbox,[6,7] which implements the fast non-negative least squares (FNNLS) algorithm.[8] Additional image processing was performed with Matlab Image Processing toolbox (The MathWorks, Inc.). The mass spectra were binned to 1 u and stored in the freely available DataSet Standard Data Object (DSO) format,[9] which combines all the separate elements associated with a multivariate data set, such as sample labels and axis scales, into a single structure variable in the MATLAB workspace.

5.3 Results and discussion

In this section, a ToF-SIMS image of the immiscible PVC–PC polymer blend was investigated, with the aim of identifying the surface species and quantifying the surface area of the distinct polymer domains formed by phase separation. The total ion image of the polymer blend is shown in Figure 5.1. This simple polymer blend is chosen as a model system as it has already been studied in detail previously.[4] My work focuses on the thorough evaluation of data analysis methods and highlights the effects of different data preprocessing.

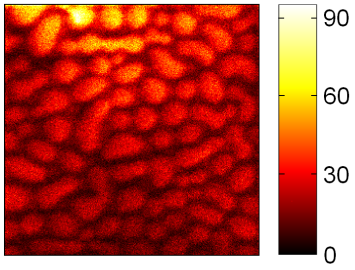

Figure 5.1 ToF-SIMS total ion image of a simple immiscible PVC–PC polymer blend, field of view = 50 μm × 50 μm.

Prior to analysis, the spectra are binned to 1 u and data for ions with a mass over 40 u are discarded to reduce the size of the data set and hence the computation time. The only observable peaks above 40 u are for Cl_2^- which do not add much further information as Cl^- is clearly observed. The lack of characteristic molecular peaks is due to the damage caused by the Ga^+ primary ion beam at the molecular signal dose (MSD) limit, where most of the molecular signals have been consumed. Therefore the removal of data over 40 u does not constitute a loss of information in this case. In addition, for reasons that will be discussed later, the top 25% of this image is also excluded from the analysis. The total ion spectrum of the cropped image is shown in Figure 5.2a. Using prior knowledge of the sample, the secondary ion images for $^{35}Cl^-$ + $^{37}Cl^-$ and O^- + OH^-, characteristic of PVC and PC respectively, are selected and shown in Figure 5.2b and 5.2c. The decrease in intensity towards the bottom of the images can be attributed to surface charging effects during acquisition with a sawtooth raster. This can be reduced by using a random raster, which was not available at the time. The phase separation of the polymers can clearly be observed. It is apparent that PVC, which forms discrete islands in the polymer blend, has a higher secondary ion yield compared to PC, which forms the continuous phase in the image. It is the surface area of these polymer domains, with dimensions around 5 μm, which will be quantified using the different analysis methods as described in the following sections.

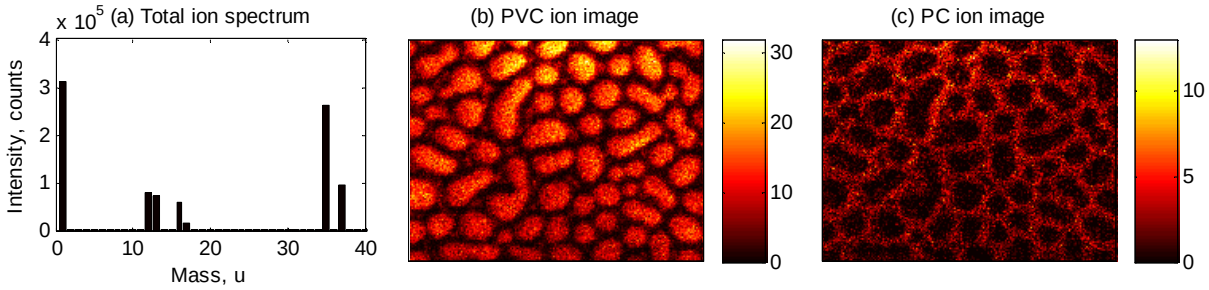

Figure 5.2 ToF-SIMS image of the PVC–PC polymer blend, after cropping, field of view = 50 μm × 37.5 μm. (a) The total ion spectrum of the cropped image. (b) $^{35}Cl^{-}$ + $^{37}Cl^{-}$ ion image representing PVC. (c) O^{-} + OH^{-} ion image representing PC.

5.3.1 Manual analysis

Due to the reduction of the signal intensity down the image, classification of each pixel to be either PVC or PC using a given threshold intensity gives irreproducible results. Therefore, in this study, a modified version of a consistent and repeatable method developed previously[4] is used for the manual quantification of the surface area of the polymer domains. The method is described below. Using Matlab Image Processing Toolbox, the characteristic ion images from Figure 5.2 are first smoothed by convolution with a circular averaging (top hat) filter with a radius of two pixels to improve the signal to noise ratio. The two images are then scaled to their respective maximum pixel intensities in order to account for the differences in secondary ion yields of the two phases. Although this is somewhat sensitive to outliers in the data, scaling to the mean intensity is not appropriate since it would be dependent on the area of coverage of the polymers. A scatter plot is then compiled by plotting the scaled PVC intensity against the PC intensity for each of the 192 × 256 pixels in the image, with the intensity of any point being proportional to the frequency of the occurrence. The resulting diagram, shown in Figure 5.3a, is fairly symmetrical along the diagonal and reveals two distinct oval distributions with the major axes almost parallel to the PVC and PC axes of the scatter plot. Plumes extend near the major axis towards higher intensities, and the two distributions overlap in a central region. As expected, pixels with high PVC intensities have low PC intensities due to the phase separation. The angular divergence of the ellipse major axes from

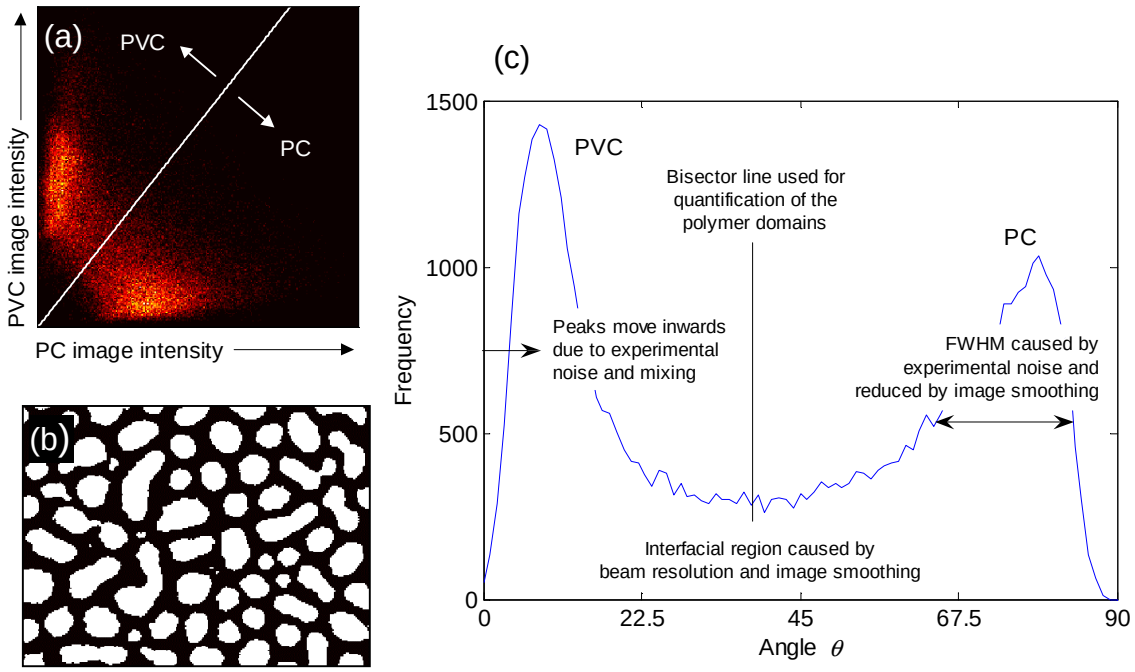

Figure 5.3 Area quantification using manual analysis. (a) Scatter plot of the scaled image intensity of PVC against the scaled image intensity of PC. (b) Domain map of the polymer blend generated by assigning image pixels according to the bisector in (a). Pixels identified as PVC are shown in white, and pixels identified as PC are shown in black. (c) Polar plot, obtained by replotting the data in (a) as a function of the angle θ on the scatter plot, where tan θ = scaled PC image intensity / scaled PVC image intensity. The ordinate is the frequency occurrence of pixels per unit angle.

the scatter plot axes arises as the phases are not pure polymers but are of each enriched with a very small amount of the other. From the previous study, it was also found that very small islands of PC, typically 200 nm in diameter, exist within the PVC-rich areas. This is smaller than the focus of the ion beam and cannot be resolved in the image after smoothing. The result is a slight broadening of the PVC plume on the scatter plot, but as we shall see, this deviation is not large enough for the pixels to be classified as PC using the bisector method for quantification. Therefore, these small islands do not affect the overall quantification of the larger domain features which are the focus of this study.

To proceed with the quantification, the scatter plot is divided into two distinct sectors using a bisector, as shown in Figure 5.3a. The bisector is drawn to go through the origin and the

geometric midpoint of the centres of the two oval distributions, which are the positions with the highest densities of pixels. A binary domain map of the polymer blend can now be generated by remapping pixels above and below this bisecting line, as shown in Figure 5.3b. By counting the number of pixels in each region, it is simple to arrive at a surface area quantification of PVC : PC = 47.1 : 52.9. This differs slightly from the results obtained in the previous study.[4] The discrepancy is solely due to the exclusion of part of the image in the current analysis, and is therefore not a matter of concern.

Before the multivariate methods are considered, it is also useful to replot the scatter plot in Figure 5.3a as shown in Figure 5.3c. Here we are not concerned with the radial distances of the data points from the origin, but their angular position on the scatter plot. The frequency occurrence of pixels per unit angle is plotted as a function of the angle θ, where tan θ = scaled PC image intensity / scaled PVC image intensity. For an ideal immiscible blend, the peaks associated with the two polymers would appear at 0° and 90° as delta function spikes. Mixing between the two phases causes the peaks to move inwards and reduces their angle of separation on the polar plot. Experimental noise in the spectra also causes the peaks to move inwards and broaden. Although smoothing the image with a circular averaging filter sharpens the peaks, it also leads to an increase in the amount of pixels within the interfacial region between the PVC and PC domains, which is also caused by the primary ion beam resolution of 300 nm. Fortunately, quantification using the bisector line has the effect of averaging this and therefore quantification is not too dependent on smoothing or beam size. The polar plot in Figure 5.3c allows these effects to be visualised rapidly, and therefore provides a clear way to evaluate the quantification of binary systems using various methods. Three criteria for accurate quantification can be established. Firstly, the angular separation of the two peaks must be large on the polar plot. Secondly, each peak must have a narrow width. Thirdly, the number of pixels close to the bisector line must be small.

At this stage it is helpful to discuss the effects of the scaling of image intensities on the scatter and polar plots produced. For the scatter plot, scaling is simply equivalent to a stretch in one

	Manual analysis		No scaling	Normalisation	Variance scaling	Poisson scaling
Quantification PVC : PC	47.1 : 52.9	PCA	45.0 : 55.0	52.2 : 47.8	44.7 : 55.3	49.6 : 50.4
Quantification error (%)	-		13.0	5.9	11.9	3.8
Number of factors	-		8	7	2	1
Quantification PVC : PC	47.1 : 52.9	MCR	48.4 : 51.6	51.5 : 48.5	47.3 : 52.7	47.1 : 52.9
Quantification error (%)	-		4.0	5.4	2.0	1.5
PVC width (°)	12		16	10	14	12
PC width (°)	21		20	35	20	19
Angular separation (°)	71		53	52	67	67
Total width / Angular separation	0.46		0.68	0.87	0.51	0.46
Pixels within 5° of bisector (%)	6.0		8.8	9.1	6.5	6.3

Table 5.1 Summary of PVC–PC polymer blend quantification results using manual analysis, PCA and MCR.

or both directions. For the polar plot however, scaling has the effect of narrowing one peak while widening the other, and may increase or decrease their angle of separation. Therefore to obtain a reliable indictor based on the quality criteria listed above, the angular widths of the two peaks on the polar plot are summed and this is then divided by their angular separation. Provided that the scaling used is sensible and the scatter plot is not overly distorted, this forms a good basis of comparison between different scatter plots. It is also worth noting that scaling does not affect the location of the bisector with respect to the pixels. Although the angular position of the bisector would change, the area quantification obtained remains the same. For the manual analysis of the polymer blend, the maxima of the PVC peak lies at 8° and the maxima of the PC peak lies at 79°, with widths of 12° and 21° at full width half maximum respectively. The ratio of total width to angular separation is 0.46 and the percentage of image pixels within 5° of the bisector is 6.0%. These results are summarised in Table 5.1 and will be compared to results obtained using MCR in Section 5.3.3.

Due to the simplicity of our model system, all chemically specific information about the two polymer phases is included in the four ion peaks (O^-, OH^-, $^{35}Cl^-$ and $^{37}Cl^-$) selected for the

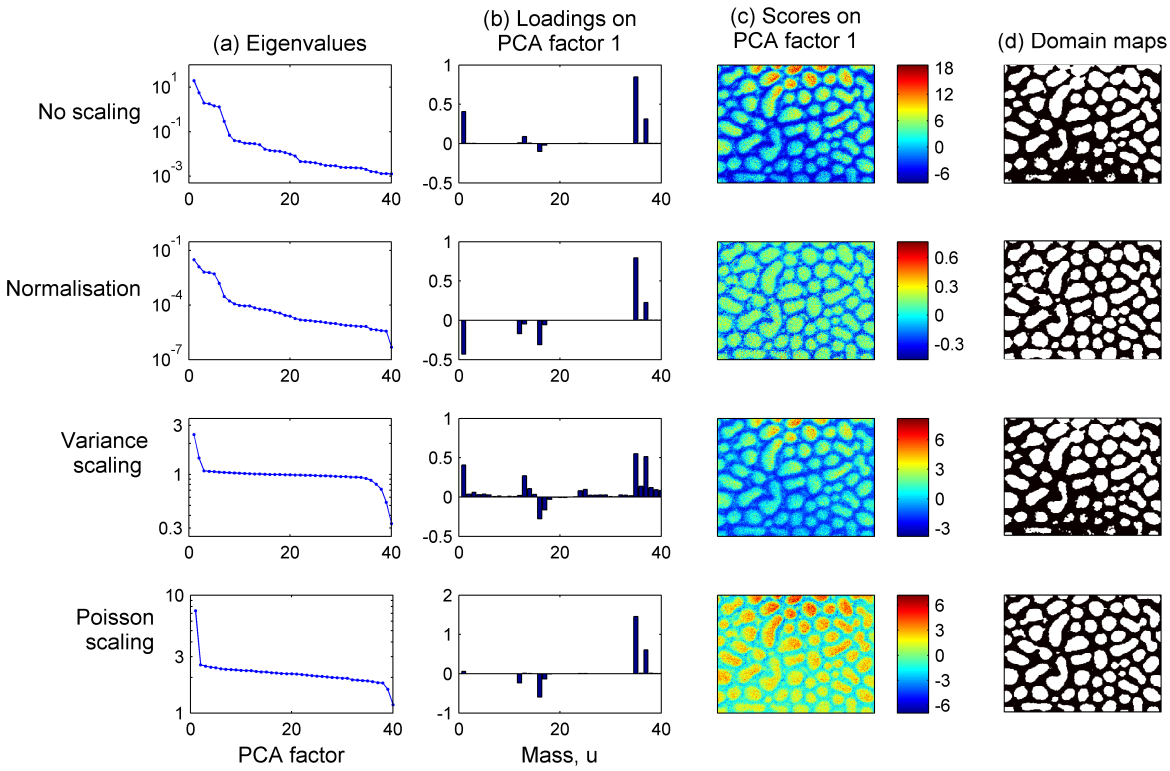

Figure 5.4 Results from PCA after the application of four data preprocessing methods, showing (a) the eigenvalue diagrams, or 'scree plots', (b) the loadings on PCA factor 1, (c) the scores on PCA factor 1, and (d) the domain maps produced using a threshold score of zero on PCA factor 1.

above analysis. Therefore, the result obtained here using manual analysis provides an effective basis for the detailed comparison and evaluation of different multivariate techniques.

5.3.2 Principal component analysis

Principal component analysis is now applied to the polymer blend image. Four different data preprocessing methods (no scaling, normalisation, variance scaling and Poisson scaling) are investigated. In all cases, the data are mean centered prior to PCA analysis. The typical computation time is less than 5 seconds due to the small size of the data set. The eigenvalue plots of the four PCA models are shown in Figure 5.4a. The eigenvalues, which are equal to the variance captured in each factor, decrease quickly for factors that contain chemical features and reach a gently declining slope for factors that describe noise variations before

dropping rapidly again for higher factors containing little additional information. Note that the eigenvalues refer to the variance captured in the preprocessed data rather than in the raw data. Since data scaling can alter both the total variance of the data and the relative variance contained in each variable, the eigenvalues are strongly dependent on the data preprocessing methods used. It is obvious that the effectiveness of PCA in accounting for variances in the data using the first few factors depends considerably on the data preprocessing method chosen. For each PCA model, the number of factors needed to describe the non-noise variances in the data is determined by the visual inspection of the eigenvalue plots, using the scree test to select the factor beyond which the eigenvalues decrease steadily and no further jumps may be observed. The loadings and scores on PCA factor 1 for each data preprocessing method are shown in Figure 5.4b and 5.4c. Regardless of the preprocessing method, PCA factor 1 successfully distinguishes the two phases, showing positive loadings on PVC characteristic ion peaks ($^{35}Cl^- + {}^{37}Cl^-$) and negative loadings on PC characteristic ion peaks ($O^- + OH^-$). This is reasonable as we expect the largest variance in the data set to arise from the chemical differences between the two polymer phases. PCA therefore enables the rapid identification of the polymer blend without any prior knowledge of the system.

The scores on PCA factor 1 are used in the quantification of the polymer blend, as follows. Since PCA factor 1 distinguishes the two polymer phases, we can classify pixels with positive scores as PVC and pixels with negative scores as PC to generate a binary domain map of the polymer blend. This method is most suitable for polymer blends where the composition is close to 50:50 and the two phases have similar intensities, since the pixels with zero scores, which are identical to the mean spectra, would lie approximately midway between the two phases. For polymer blends with composition far from 50:50 or vastly different secondary ion yields between the phases, the mean spectra would shift towards the more abundant or intense phase, and therefore a threshold score of zero is no longer suitable for the classification of the polymer domains. To ensure results obtained in this study are directly comparable with manual analysis, which gave smooth domain boundaries using spatially averaged ion intensities, the PCA scores images are smoothed by a circular averaging filter as used in

manual analysis prior to classification. It is worth noting that smoothing was not performed on the original data prior to PCA analysis as we are interested in evaluating the ability of PCA in extracting chemically significant variances from noisy data typical in ToF-SIMS imaging. The domain maps of the polymer blend for PCA with each of the four data preprocessing methods is shown in Figure 5.4d. By counting the number of pixels in each phase, an overall surface area quantification can be obtained. To assess the accuracy of the quantification, a comparison is made for each pixel between the domain maps obtained from PCA and manual analysis. The quantification error is then defined as the percentage of pixels that are misclassified in PCA. Finally, the results obtained above are summarised in Table 5.1 for each data preprocessing method.

It is now possible to analyse the effect of data preprocessing on the quantification of the polymer blend. It is obvious that the ability of PCA to describe the chemically significant variance in the data set, and therefore produce accurate domain maps and quantification, is hugely affected by the data preprocessing method applied.

No scaling

Without scaling, eight factors are required to describe the data, as determined using the scree test. The loadings on PCA factor 1 are dominated by intense secondary ions such as H^- and $^{35}Cl^-$. This describes the variations of overall ion intensities in the image, and only weakly distinguishes the chemistry of the two phases. As a result, the domain map obtained without scaling is a poor representation of the chemistry of the system, and displays a significant gradient due to the changes in secondary ion intensities arising from surface charging. Despite an overall quantification value that is close to the result obtained in manual analysis, a large quantification error of 13.0% is obtained. Therefore, PCA with no scaling is shown to be unsuitable for the accurate quantification of polymer domains.

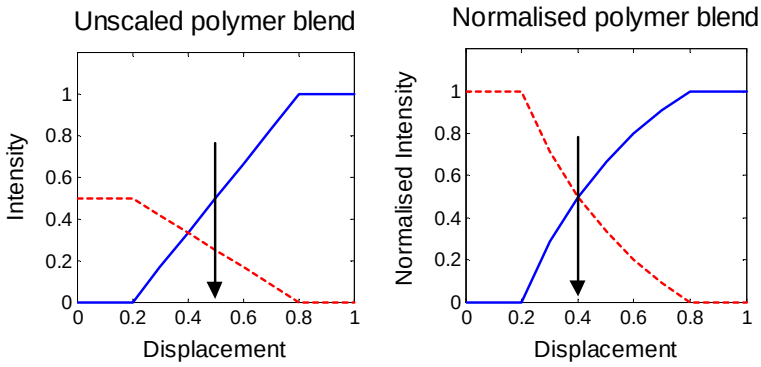

Figure 5.5 A simple illustrative model showing the effect of normalisation on the surface area quantification of a binary immiscible mixture. The locations of the phase boundaries are shown by the vertical arrow. Normalisation moves the boundary such that the perceived surface area of the more intense component is enhanced.

Normalisation

Normalisation reduces the effect of intensity variations due to surface charging, by scaling the data so that the total count per pixel is constant. Since normalisation removes one degree of freedom from the data set, seven factors are needed to account for the data. Normalisation results in an improved description of chemical differences in the loadings on PCA factor 1, along with clear scores image and domain map that are not driven by changes in overall ion intensities. Normalisation thus reduces the quantification error to 5.9%. However, normalisation is found to overestimate the amount of PVC on the surface, resulting in a quantification value of PVC : PC = 52.2 : 47.8, compared with the manual analysis result of 47.1 : 52.9. This is due to the higher secondary ion yield of PVC compared to PC, and can be explained simply as shown in Figure 5.5. This shows two immiscible chemicals components across a simple phase boundary, where the measured intensities of both components decrease in a linear manner between one phase and the other due to the limited resolution of the primary ion beam in ToF-SIMS. Vertical arrows on the diagrams mark the locations of the phase boundaries where both components have intensities that are half of their maximum values. Normalisation, such that the sum of intensities at any point is unity, moves the boundary such that the perceived surface area of the more intense component is enhanced. Therefore, normalisation can significantly distort quantification and whilst it is an

improvement from no scaling, it is not optimal for determining the relative fraction of the two components.

Variance scaling

Variance scaling equalises the variance of each peak prior to PCA, so that the less intense O^- and OH^- peaks associated with PC are given the same importance as the more intense $^{35}Cl^-$ and $^{37}Cl^-$ peaks associated with PVC. However, variance scaling also enhances weak, non-characteristic peaks, and therefore produces noisy loadings that are unsuitable for identification. The domain map is again dominated by the changes in overall ion intensities, and a large quantification error of 11.9% is obtained. Despite the small number of factors required to describe the data, the PCA result after variance scaling is unsuitable for either identification or quantification of surface materials.

Poisson scaling

Poisson scaling equalises the noise variance of each peak prior to PCA using the Poisson counting statistics of the detector. The loadings on PCA factor 1 show excellent chemical characterisation of the system and the H^- ion is notably absent. Due to its high yield, H^- has a large associated counting error, but manual inspection of the ion image reveals only a weak correlation with the PVC phase. Poisson scaling is therefore the only method able to separate the Poisson counting error from chemical variations and provide improved chemical characterisation in PCA. The area quantification with Poisson scaling is in good agreement with manual results and the quantification error, 3.8%, is the lowest out of all data preprocessing methods investigated. The domain map generated is clear and unaffected by the changes in ion intensities due to surface charging, and furthermore it is clear from the eigenvalue plot that one factor is sufficient to describe the data, in agreement with the single degree of freedom characteristic of a binary system. Thus, Poisson scaling concentrates all chemically significant information into the fewest number of factors and accomplishes greater noise rejection. The superiority of Poisson scaled PCA in the characterisation and

quantification of surface chemical composition is therefore clearly demonstrated using this polymer blend system.

5.3.3 Multivariate curve resolution

The next step of this study is to evaluate multivariate curve resolution in the identification and quantification of the polymer blend image, after data preprocessing using the four methods discussed previously. MCR with a non-negativity constraint for the loadings and scores is applied to the preprocessed data. Mean centering is not carried out prior to analysis, since the non-negativity constraint requires the data to have positive values throughout. Using prior knowledge of the system, the number of factors is fixed at two. An initial estimate of the loadings matrix for the alternating least squares fitting is obtained using a Varimax rotation[10] of the first two factors of equivalent PCA models without mean centering. MCR is more computational intensive than PCA, and a typical analysis of the data takes 2 – 5 minutes, depending on the criteria for convergence.

For all data preprocessing methods, MCR is able to extract two distinctive factors, with the loadings showing strong resemblances to experimental ToF-SIMS spectra of pure PVC and PC. The scores images also agree closely with the distribution of PVC and PC from the raw data in Figure 5.2. MCR therefore enables the identification of the polymer blend without prior knowledge of the system. MCR results after Poisson scaling are shown in Figure 5.6. Results for other preprocessing methods are qualitatively similar to these, with the exceptions that variance scaling produces noisy loadings with many non-characteristic peaks, and normalisation produces scores images without the gradient in intensity. To obtain a surface area quantification of the polymer blend we use the same approach as in manual analysis, and plot the scaled intensities of the two MCR scores images on a scatter diagram for each pixel. The locations of the bisectors are calculated, and the resulting scatter plots are shown in Figure 5.7a–d. Using this, the domains maps for surface area quantification are generated, and the quantification error, defined as the percentage of pixels that are misclassified in MCR compared to manual analysis, is calculated for each preprocessing method. In addition, a polar

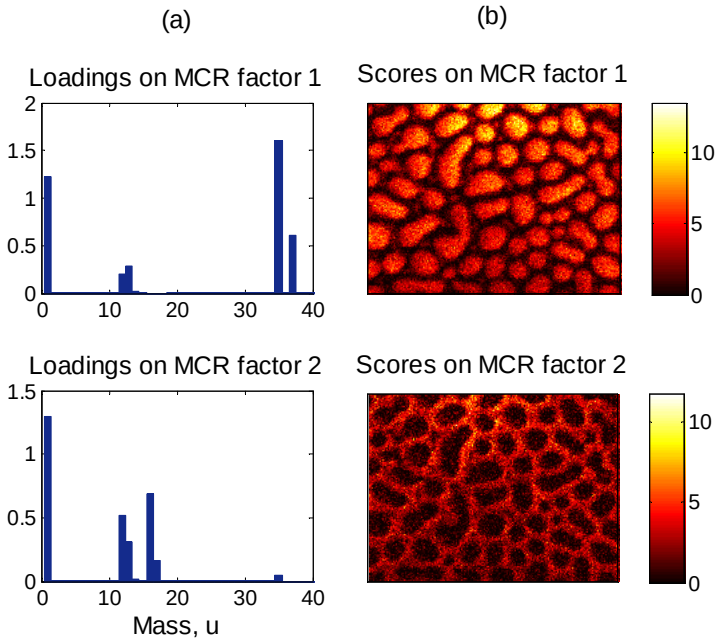

Figure 5.6 Results from MCR, after Poisson scaling. (a) The loadings on the MCR factors, corresponding to PVC and PC chemical spectra respectively, and (b) the scores on the MCR factors, corresponding to the distribution of PVC and PC, in agreement with the raw data shown in Figure 5.2.

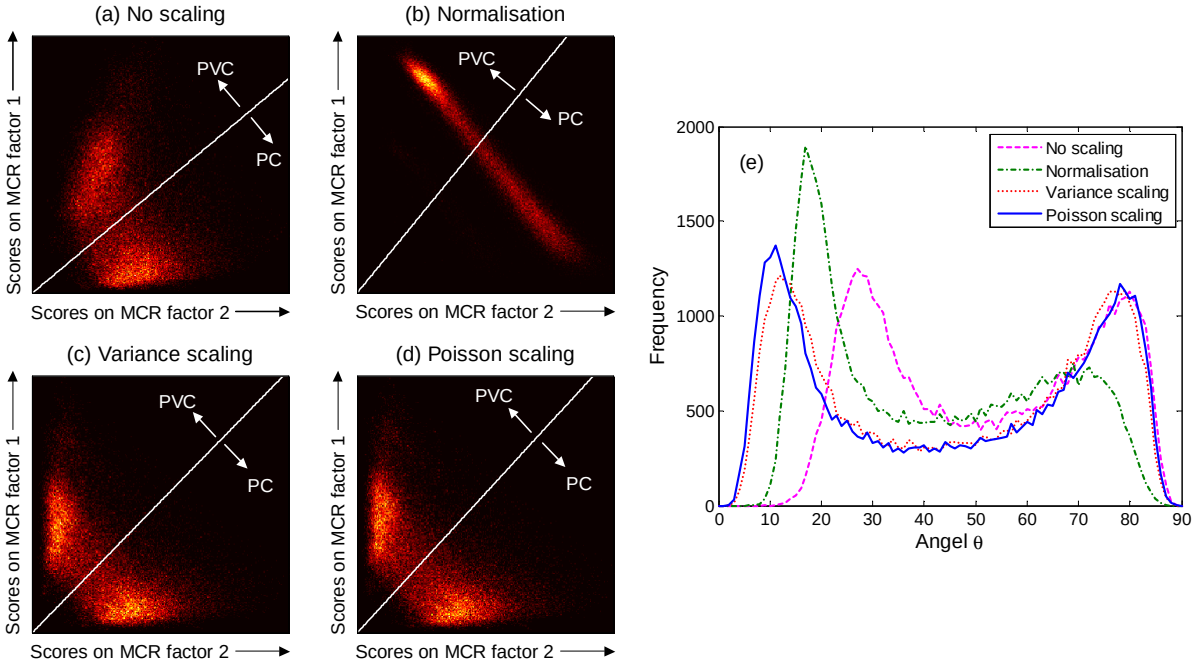

Figure 5.7 Scatter plot of the intensities of the MCR scores images, after (a) no scaling (b) normalisation (c) variance scaling (d) Poisson scaling. (e) Polar plots generated from the scatter plots, showing the angular frequency occurrence of pixels as a function of angle on the scatter plot, for different data preprocessing methods.

plot showing the frequency of occurrence of image pixels as a function of their angle on the scatter plots is given in Figure 5.7e. The width of the peaks, their angular separation, the ratio of the total width to the angular separation, and the number of pixels within 5° of the bisector, are obtained for each preprocessing method. All results are summarised in Table 5.1.

Regardless of data preprocessing, the domain maps produced by MCR are similar to manual analysis and are unaffected by the intensity variations down the image, due to the use of a bisector for quantification rather than a threshold value. Quantification is therefore improved, with errors below 6% in all cases. Using the scatter and polar plots produced, the effects of data preprocessing on the resolution of the two chemical phases using MCR are analysed.

No scaling

Without scaling, MCR produces a skewed scatter plot as shown in Figure 5.7a. MCR has difficulties resolving the weaker contribution of PC from the unscaled data dominated by strong PVC intensity variations, and low contrast is observed in the scores image associated with PC. Consequently, the scatter plot shows a large spread of pixels, and the ratio of peak widths to angular separation on the polar plot is large compared to manual analysis. Despite a good overall area quantification and a low quantification error, MCR without scaling is not optimal and does not effectively describe the chemical structure of the data.

Normalisation

After nrmalisation of the data to the total count per pixel, MCR produces a distinctly different scatter plot, as shown in Figure 5.7b. The scores on MCR factor 1 and 2 lie along a straight line and their sum is roughly constant for each pixel, in agreement with the normalisation procedure[11] and our understanding that only two chemical components are present in the system. Since the magnitudes of the scores are interdependent after normalisation, the separation of the phases on the scatter and polar plots is weak. The bisector method for quantification is therefore no longer appropriate and normalisation gives the highest width to

angular separation ratio. As observed previously and illustrated in Figure 5.5, normalisation also overestimates the surface area of PVC domains in MCR, giving PVC : PC = 51.5 : 48.5. Normalisation is therefore unsuitable for quantification in MCR and produces the largest error out of all data preprocessing methods investigated.

Variance scaling

As discussed earlier, variance scaling produces loadings containing a large number of uncharacteristic peaks that are unsuitable for chemical identification. Despite this, good contrast is seen in the MCR scores images, which gives a symmetrical scatter plot of intensities as shown in Figure 5.7c. Two separate distributions can be observed and the bisector method produces an excellent area quantification of PVC : PC = 47.3 : 52.7 with a small quantification error of 2.0%. Good statistics are also obtained with the polar plot, and the widths of the peaks and their angular separation are comparable with manual analysis results. Variance scaling is therefore suitable for area quantification using MCR.

Poisson scaling

Figure 5.6 shows the MCR loadings and scores obtained after Poisson scaling. The loadings strongly resemble ToF-SIMS spectra of pure PVC and PC, allowing straightforward identification of the species. Poisson scaling produces a symmetrical scatter plot, shown in Figure 5.7d, that gives an excellent area quantification of PVC : PC = 47.1 : 52.9. This is in perfect agreement with the results obtained manually, with the lowest quantification error of 1.5% out of all methods. Using the polar plot in Figure 5.7e, Poisson scaling is easily identified as the best data preprocessing method. It gives the smallest widths to angular separation ratio as well as the lowest number of pixels within 5º of the bisector, therefore the bisector method for quantification is very effective. Poisson scaling also provides the greatest noise rejection in MCR, since the alternating least squares fitting of MCR loadings and scores are carried out on the PCA reproduced data. This conclusion is that Poisson scaling is the most appropriate preprocessing method for MCR, and it is shown to be useful for accurate

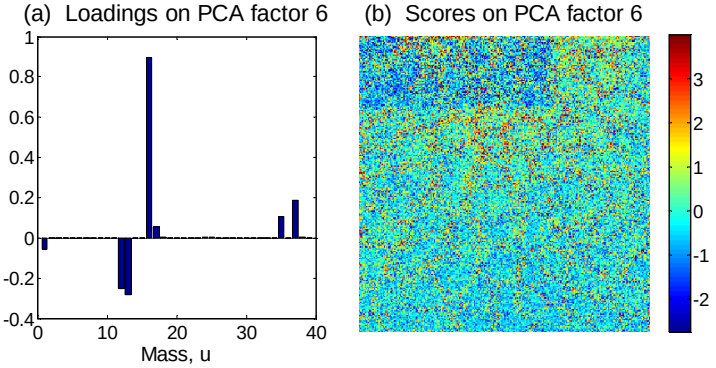

Figure 5.8 Results from PCA of the full frame image, without data scaling. (a) The loadings on PCA factor 6, and (b) the scores on PCA factor 6, showing small changes in relative ion intensities in the pre-sputtered area on the top left corner of the image. Image contrast was enhanced by removing a small number of extreme values from the scores.

identification, localisation and quantification of surface chemicals, without any prior knowledge of the system.

5.3.4 Investigation of the excluded area

Next we return to the top 25% of the polymer blend image which was excluded in the above analysis. In the full frame ToF-SIMS image shown in Figure 5.1, brighter PVC domains are observed on the left hand side of the excluded region. It is not clear if this is caused by edge, charging, topography, contamination or other effects. Figure 5.8 shows the loadings and scores on factor 6 of the PCA model on the full frame image without scaling. A dark rectangular area is clearly visible on the top left corner of the scores image. This region corresponds to an area where a separate ToF-SIMS image was acquired previously, and therefore it has received a higher primary ion dose than the rest of the image. The chemical differences between the two regions can be studied by comparing their average spectra. The pre-sputtered region shows an overall increase in secondary ion yields and small changes in the relative intensities of key peaks. In the pre-sputtered region, a reduction in ratio of $^{35}Cl^-$ to $^{37}Cl^-$ indicates saturation of the more intense $^{35}Cl^-$ peak, and the ratio of (C^- + CH^-) to (O^- + OH^-) is increased, indicating changes due to damage. These effects are small compared to dominant features such as chemical differences between polymers and charging effects.

Therefore, they are not obvious upon inspection of individual ion images, and would be overlooked in manual analysis. With PCA, the damaged area can be clearly distinguished using the higher factors. PCA analysis thus allows for rapid and unambiguous detection of the problem, and this illustrates a key benefit of multivariate analysis over traditional analysis.

5.4 Simulated data

So far recommendations for the optimum use of multivariate analysis and guidance on data preprocessing methods have been discussed using a simple model system consisting of a PVC–PC polymer blend. To demonstrate the benefits of multivariate analysis over manual analysis for a more complex data set, the methodology developed is applied to a computer simulated image of an immiscible polymer blend, composed of two structurally similar polymers, poly(methyl methacrylate) (PMMA) and poly(ethyl methacrylate) (PEMA). Positive ion ToF-SIMS spectra for PMMA and PEMA are acquired experimentally and binned to 1 u, for masses between 1 and 400 u. The chemical structures of the polymers and their spectra are shown in Figure 5.9. To generate a multivariate image data set, the spectra are scaled to their respective total ion intensity, and assigned to the domain map obtained manually from the PVC–PC data, which is shown in Figure 5.3b. PEMA is assigned as the discrete phase (white areas) and PMMA is assigned as the continuous phase (black areas). To reduce the computational time required, I focus only on a 64×64 pixel area on the bottom left of the simulated image. The resulting image has an area coverage of PMMA : PEMA = 49.5 : 50.5, and this will be compared with quantification results obtained using manual analysis, PCA and MCR. To simulate the blurring at the phase boundaries due to limited ion beam resolution, the image is smoothed by convolution with a circular averaging (top hat) filter with a radius of two pixels. Noise is then added to the data set using a Poisson random number generator, so that the average intensity for each unit mass between 1 u and 400 u at each pixel is only 10 counts. This replicates the extremely low signal to noise ratio typically obtained in a high resolution ToF-SIMS image. Manual analysis, PCA and MCR methods are then evaluated on the simulated data. All results from the following analyses are summarised in Table 5.2.

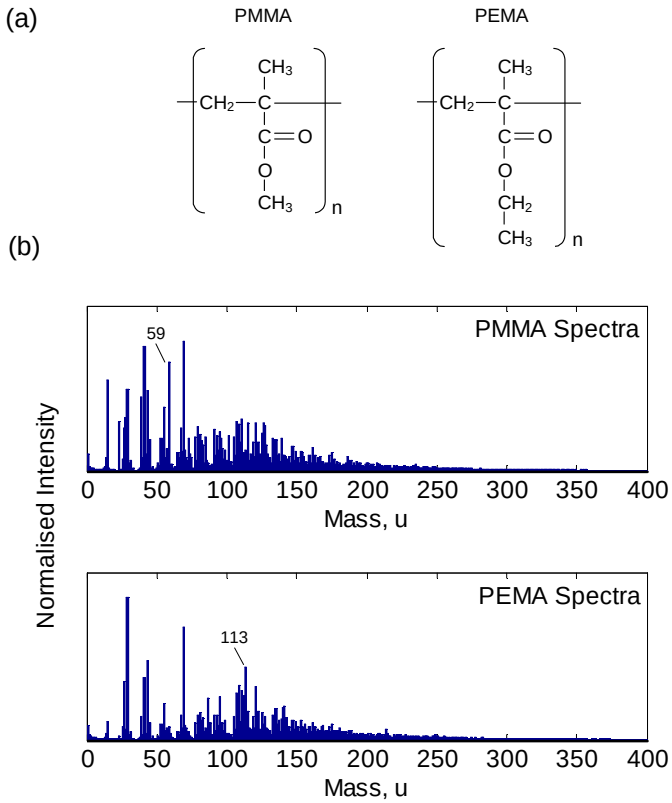

Figure 5.9 Two structurally similar polymers, poly(methyl methacrylate) (PMMA) and poly(ethyl methacrylate) (PEMA), used in the computer simulated polymer blend, showing their respective (a) chemical structures and (b) experimental ToF-SIMS spectra.

	Original data	Manual analysis	PCA with Poisson scaling	MCR with Poisson scaling
Quantification PMMA : PEMA	49.5 : 50.5	50.3 : 49.7	49.8 : 50.2	49.8 : 50.2
Quantification error (%)	-	1.9	1.1	1.1
PMMA width (°)	-	8	-	4
PEMA width (°)	-	6	-	4
Angular separation (°)	-	69	-	78
Total width / Angular separation	-	0.20	-	0.10
Pixels within 5° of bisector (%)	-	3.4	-	2.7

Table 5.2 Summary of simulated PMMA–PEMA polymer blend quantification results using PCA and MCR.

5.4.1 Manual analysis

Manual analysis of the polymer blend can be carried out using known characteristic peaks of the polymers. Due to the similarities between their structures, unique peaks are difficult to find. Here, the fragment peak $(COOCH_3)^+$ (59 u) is used for PMMA, and the $(M-H)^+$

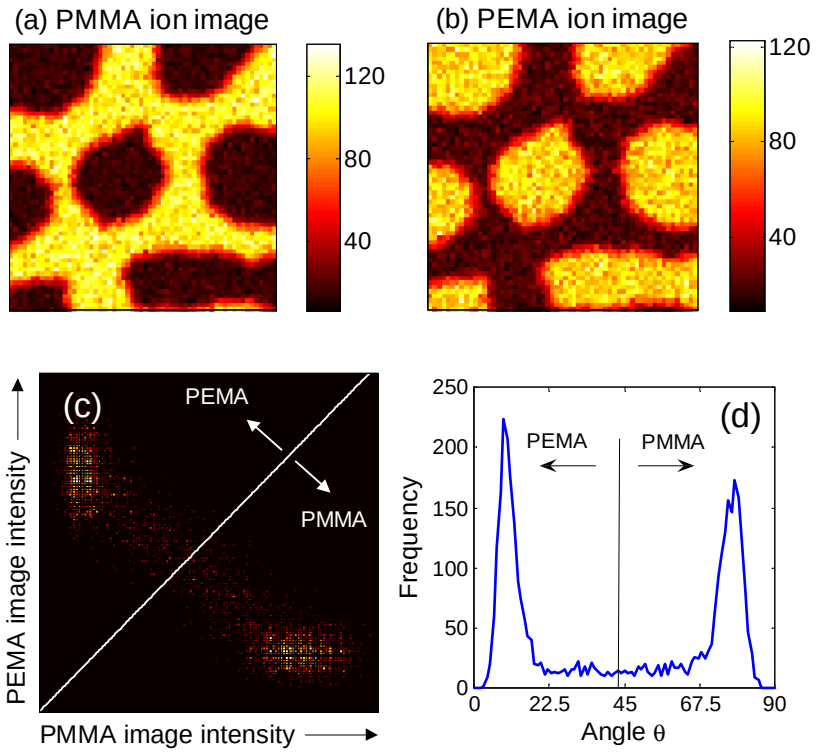

Figure 5.10 Manual analysis results obtained for the computer simulated PMMA–PEMA polymer blend using only two characteristic peaks. (a) PMMA ion image, using $COOCH_3^+$ peak. (b) PEMA ion image, using $(M-H)^+$ peak. (c) Scatter plot of the scaled image intensities. (d) Polar plot generated from the scatter plot.

monomer peak (113 u) is used for PEMA. The ion images for PMMA and PEMA, and the resulting scatter and polar plots are shown in Figure 5.10. These images are noisy since manual analysis uses information from only two ion peaks out of a total of 400 available in the data. Consequently there is a large spread on the scatter plot, resulting in large widths on the polar plot and a large number of pixels in the vicinity of the bisector. Using the bisector method as before, a surface area of PMMA : PEMA = 50.3 : 49.7 is obtained with a quantification error of 1.9%.

5.4.2 Principal component analysis

Using PCA with Poisson scaling, factor 1 successfully distinguishes the chemical differences between the polymers, with the loadings given in Figure 5.11a showing a number of peaks

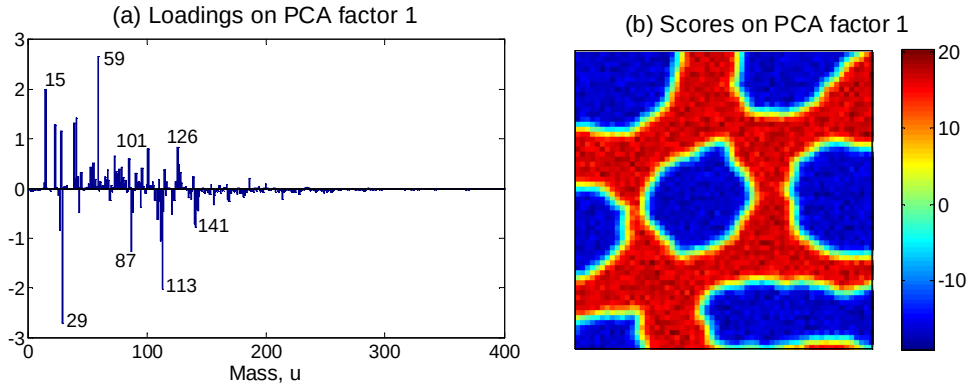

Figure 5.11 PCA results obtained for the computer simulated PMMA-PEMA polymer blend image, after Poisson scaling. (a) Loadings on PCA factor 1. PCA successfully distinguishes the two chemical phases. Positive peaks are associated with PMMA while negative peaks are associated with PEMA. (b) Scores on PCA factor 1.

most characteristic to each phase. This provides valuable information about the image that is not available in manual analysis. The associated scores image in Figure 5.11b has a higher signal to noise ratio than the ion images generated by manual analysis. By assigning pixels with positive scores to PMMA and negative scores to PEMA, a surface area quantification of PMMA : PEMA = 49.8 : 50.2 is obtained, in excellent agreement with the original image. Using PCA, the quantification error is reduced to 1.1%.

5.4.3 Multivariate curve resolution

MCR with Poisson scaling is also applied to the data set, and the results are shown in Figure 5.12. Two factors are resolved, and the loadings and scores correspond to the spectra and distributions of PMMA and PEMA respectively. Since MCR correlates information from multiple peaks in the data, the signal to noise ratio and contrast of the scores images are greatly improved compared to manual analysis. Two dense clusters can be seen on the scatter plot, corresponding to pure PMMA and PEMA areas in the image. The weak linear distribution between the two clusters corresponds to pixels near the phase boundary due to image blurring. The polar plot obtained from MCR shows a marked improvement compared to manual analysis, with smaller peak widths, larger angular separation and smaller number of pixels near of the bisector. Using MCR, a surface area quantification of PMMA : PEMA =

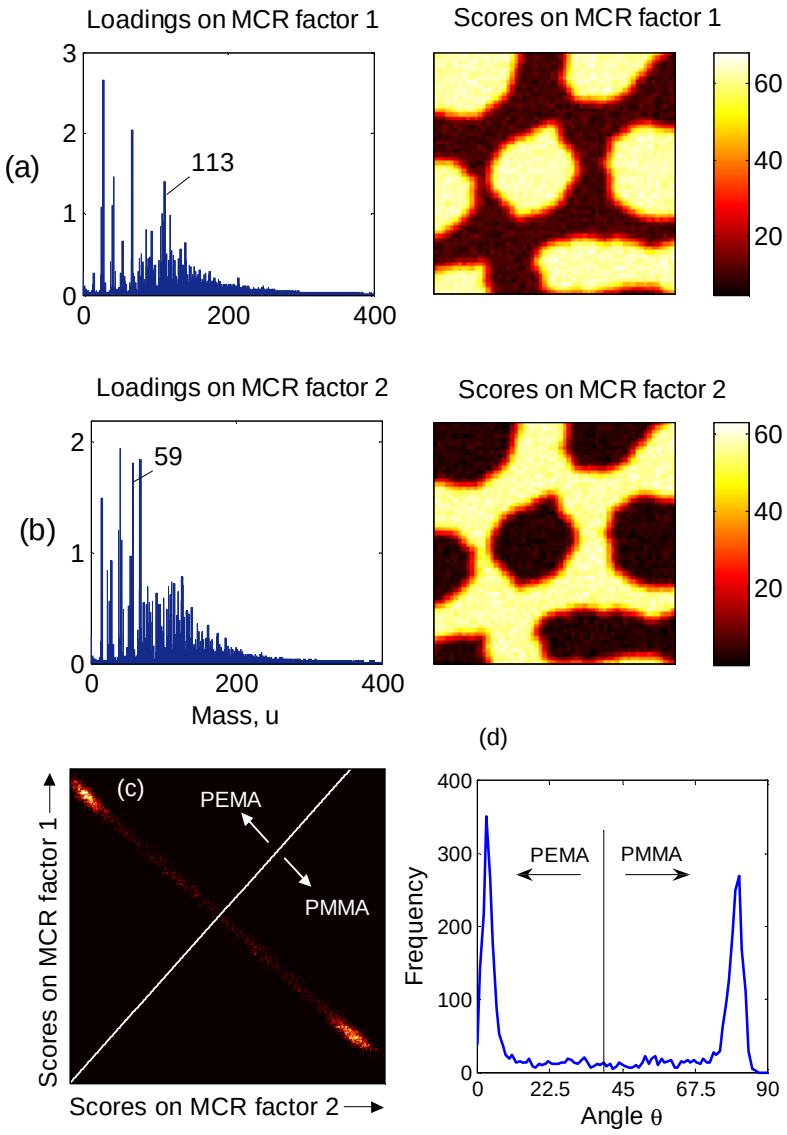

Figure 5.12 MCR results obtained for the computer simulated PMMA-PEMA polymer blend image, after Poisson scaling. (a) MCR factor 1, corresponding to PEMA. (b) MCR factor 2, corresponding to PMMA. (c) Scatter plot of the scaled scores image intensities. (d) Polar plot generated from the scatter plot.

49.8 : 50.2 is obtained, in excellent agreement with the original image. The correlations between MCR loadings and experimental polymer spectra are found to be $R^2 = 0.986$ and $R^2 = 0.999$ for PMMA and PEMA, respectively, where R^2 is the coefficient of determination. Therefore, MCR allows for unambiguous identification of the species even in the case of a complex data set where chemical constituents share a large number of common peaks. Using the simulated system above, MCR is shown to be advantageous compared to manual analysis for the analysis of complex data sets involving large number of peaks, and

	Manual	PCA	MCR
Speed	Slow	Fast	Medium
Identification	Difficult	Medium	Easy
Quantification	–	Poisson scaling recommended	
Most Suitable For	Simple data sets	Discrimination of similar phases	Identification of unknown mixtures

Table 5.3 Comparison of multivariate analysis methods.

allows for accurate identification and quantification without any prior knowledge of the system.

5.5 Conclusions

From this study of an immiscible polymer blend, the multivariate techniques of PCA and MCR are shown to be suitable for identification and accurate quantification of ToF-SIMS image data sets. While simple identification is often straightforward, the method of data preprocessing can greatly affect any quantification results obtained and therefore great care is needed in its application. It is found that normalisation potentially distorts quantification, and variance scaling is not recommended due to its tendency to obtain factors that are noisy. Poisson scaling is demonstrated to be the most suitable data preprocessing method for both PCA and MCR. Using this, the recommendations for the optimum use of multivariate analysis are presented in Table 5.3. This study has demonstrated the capability of multivariate analysis for obtaining information that would be difficult to extract with traditional analysis. The speed, automation and accuracy of multivariate analysis, even in the absence of prior knowledge of the system, make it advantageous to traditional analysis methods. However, multivariate analysis cannot diminish the importance of an experienced analyst, who is required to provide an interpretation of the computed results that is in agreement with the experimental data as well as the physical and chemical properties of the system. Using the above approach, multivariate analysis is very powerful in the analysis of ToF-SIMS spectra

and images. It is fast, unbiased and extracts the maximum information, required in the study of increasingly complex multi-organic surfaces and biomaterials.

References

1 J. L. S. Lee and I. S. Gilmore, in *Surface Analysis – The Principal Techniques*, 2nd ed., edited by J. C. Vickerman and I. S. Gilmore (Wiley, Chichester, 2008), p. 563.

2 J. L. S. Lee, B. J. Tyler, M. S. Wagner, I. S. Gilmore, and M. P. Seah, Surface and Interface Analysis **41,** 76 (2009).

3 M. P. Seah, Surface and Interface Analysis **27,** 693 (1999).

4 I. S. Gilmore, M. P. Seah, and J. E. Johnstone, Surface and Interface Analysis **35,** 888 (2003).

5 J. Schwieters, H. G. Cramer, T. Heller, U. Jurgens, E. Niehuis, J. Zehnpfenning, and A. Benninghoven, Journal of Vacuum Science & Technology a-Vacuum Surfaces and Films **9,** 2864 (1991).

6 R. Tauler, J. de Juan. Multivariate Curve Resolution Graphic User-Friendly Interface. <http://www.ub.edu/mcr/als2004.htm> (2006).

7 J. Jaumot, R. Gargallo, A. de Juan, and R. Tauler, Chemometrics and Intelligent Laboratory Systems **76,** 101 (2005).

8 R. Bro and S. DeJong, Journal of Chemometrics **11,** 393 (1997).

9 B. M. Wise, N. B. Gallagher. DataSet Standard Data Object for Use with MATLAB. <http://software.eigenvector.com/DataSet/> (2005).

10 H. F. Kaiser, Psychometrika **23,** 187 (1958).

11 S. N. Deming, J. A. Palasota, and J. M. Nocerino, Journal of Chemometrics **7,** 393 (1993).

Chapter 6 – Multivariate image analysis strategies for ToF-SIMS images with topography

6.1 Introduction

Surface properties are crucial to the development of hair shampoos and conditioners for the personal care industry. For example, hair conditioner modifies the surface friction of hairs as they slide against each other. A typical shampoo or conditioner formulation contains many chemical ingredients, including surfactants, foaming agents and foam stabilizers, moisturisers, anti-static agents, thickeners, amino acids, emulsifiers, preservatives, buffering agents, water softening agents and perfumes.[1] The localisation, quantification and identification of these components on the hair fibres, both initially and as a function of the effects of washing and other processes, is critically important for formulators to understand the chemical mechanisms such as migration, competitive segregation, penetration and desorption which influence product performance. As a result, ToF-SIMS has been applied successfully to investigate the effect of surface treatments on human hair.[2-6] It is clear that robust industry measurement methods are crucial for this purpose. However, several barriers exist to the wider uptake of ToF-SIMS in general industrial analyses. Firstly, quantitative characterisation of surfaces with topography remains a significant challenge due to the lack of systematic and validated measurement and data analysis methods. Secondly, the increased power and throughput of modern ToF-SIMS instruments, as well as the increasing chemical complexity of real-life industrial samples, necessitate new data analysis methodologies which are capable of exploiting the wealth of information obtained from ToF-SIMS in a robust and speedy manner. This is especially important for many commercial analytical laboratories, where data analysis rather than acquisition is currently the major bottleneck in providing fast turnaround analytical services. This impacts upon the cost of such analyses and restricts the wider uptake of ToF-SIMS in industry, despite the obvious advantages of this powerful technique for many applications.

Owing to the complexity of ToF-SIMS data sets, multivariate analysis methods are often employed. An introduction to multivariate analysis methods is given in Chapter 4 and in the previous chapter, the quantification and methodology issues in multivariate analysis are investigated using an immiscible polymer blend as a model system. However, while multivariate analysis has been widely evaluated on model patterned surfaces[7-11] or synthetic data,[11,12] fewer studies have been published on their applications in industry.[13,14] Many challenges remain here, due to surface topography as well as detector saturation, which is common since a large primary ion current is needed to maximize the detection sensitivity for low abundance or low yield ion species and reduce the total acquisition time required for a sufficient signal to noise ratio. The effects of topography are discussed in detail in Chapters 2 and 3 for conducting and insulating samples respectively. The aim of this study is to explore the robust application of principal component analysis (PCA) and multivariate curve resolution (MCR) to more complex ToF-SIMS images, with the aim of providing a robust analysis strategy for images obtained in practical analyses where sample topography and detector saturation may be important, and to provide further guidance on the advantages, limitations and caveats of different multivariate techniques and data scaling methods.

6.2 Experimental

ToF-SIMS raw data consisting of an image of hair fibres treated with a multi-component formulation was kindly provided by Dr Ian Fletcher (Intertek MSG). The sample preparation and data acquisition was carried out by Dr Fletcher, as follows. Clean, virgin human hairs (i.e. hair with no history of chemical treatment) were rinsed in running tap water, treated with a multi-component hair formulation for 1 minute and then rinsed and dried at room temperature. The treated hair samples were mounted carefully between a 1 cm × 1 cm molybdenum grid and a stainless steel plate of the same size. Reference SIMS spectra of the major ingredients of the formulation were acquired using a dilute coating of each ingredient on small pieces of PET film. Static SIMS analyses were made using an ION-TOF TOF-SIMS IV instrument (ION-TOF GmbH., Münster, Germany) of single-stage reflectron design.[15] Positive ion images of the hair fibres after treatment were obtained using a Bi_3^{2+} focused

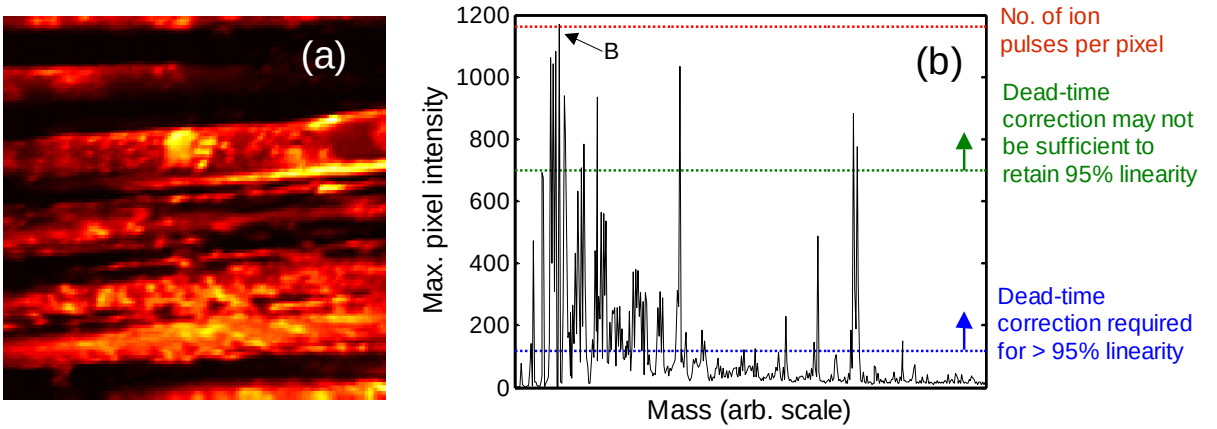

Figure 6.1 ToF-SIMS image of hair fibres treated with a multi-component formulation. (a) Total ion image. (b) A spectrum showing the maximum ion intensity in any pixel as a function of unit mass, before dead-time correction. An example of a highly saturated peak (peak B) is marked on the spectrum.

liquid metal ion gun at 40 keV energy, incident at 45° to the surface normal and operated in bunched mode. Charge compensation was effected by low-energy (20 eV) electrons provided by a flood gun. Raw data containing the secondary ions recorded at each pixel were acquired with a 128 × 128 pixel raster and a field of view of 500 μm × 500 μm, using 1 primary ion pulse per pixel in each scan and a total of 1164 image scans. The total ion dose was 1×10^{16} ions m^{-2} and the total acquisition time was 48 minutes. Due to the topography of the sample surface, the mass resolving power achieved over the entire image was limited to $m/\Delta m$ = 1500. The resulting total ion image is shown in Figure 6.1a.

All data analyses were carried out by myself. First, the data were calibrated for masses and binned to 1 u using the instrument software (TOF-SIMS Software v4.1), since the poor mass resolution renders the use of a high mass resolution peak list unfeasible. The data were then exported from the instrument software as a binary image file (.BIF) and imported into Matlab v7.3 (The MathWorks, Inc., Natwick, MA, USA) using the CAMECARD routine provided in MIA Toolbox v1.0 (Eigenvector Research, Inc., Wenatchee, WA, USA). PCA was conducted using PLS Toolbox v4.0 (Eigenvector Research) with MIA Toolbox v1.0 (Eigenvector Research) add-on for multivariate image analysis. MCR was conducted using a

freely available MCR-ALS Toolbox.[16,17] Initial estimates for MCR were obtained using a Varimax rotation[18] of PCA factors, inverting the sign if necessary so that each rotated factor contains mostly positive peaks. This is to ensure good initial estimates for MCR due to the non-negativity constraints. To increase the stability of the MCR algorithm, the alternating least-squares fitting is carried out on the noise-filtered PCA reproduced data matrix rather than the original data matrix. Convergence is achieved when the percentage change of the standard deviation of the residuals between two consecutive iterations reduces below 1%. All other operations, including dead time correction and data scaling, were performed in Matlab using custom routines. Typical computation times for PCA and MCR are approximately 7 s and 300 s respectively, using a 32 bit desktop PC with a 3 GHz processor and 3 GB of RAM. Finally, due to the commercial nature of this sample, the identities of the original ingredients in the formulation were disguised by removing the mass scale and shifting the mass position of each peak by up to ± 25 u in the figures shown. This procedure is done consistently for all spectra and eliminates the possibility of identifying the actual mass of the peaks from the printed figures, but it does not in any way affect the data analysis and the interpretation of the results.

6.3 Data pretreatment

In this section, data pretreatment for the ToF-SIMS image prior to multivariate analysis is investigated. The total ion image of the hair fibres pre-treated with a multi-component formulation is shown in Figure 6.1a. This is a challenging sample to analyse due to the extreme topography, evident from the large number of pixels where the total ion intensity is close to zero. These dark background areas, covering approximately 20% of the image, are caused by geometrical and ion shadowing effects from topography, explained in Chapters 2 and 3, as well as space between individual hair fibres. The maximum intensity spectrum is shown in Figure 6.1b. This shows the maximum ion intensity in any pixel as a function of unit mass, before dead time correction. The maximum intensity spectrum is displayed in preference to the total ion spectrum (not shown) here, since it highlights localised chemical features that may otherwise be overlooked using the total ion spectrum, where intensities of

ions are also dependent on their spatial coverage. It is evident there are a large number of unknown chemical components on the surface of the hair, and their distributions are highly localised.

6.3.1 Detector saturation

Prior to multivariate analysis, it is important to ascertain the source and extent of non-linearities in the data and minimise them if possible so that linear multivariate models such as PCA and MCR can provide a good physical description of the data. For example, in PCA, non-linear intensity variations caused by detector saturation frequently appear as extra factors.[19] Linearity and dead time correction routines are studied in detail in References 20 and 21. Although there are a number of causes of non-linearities in TOF-SIMS instrumentation, the most significant is intensity saturation caused by the effective dead time of the detector system.[20] This arises since only one secondary ion count per primary ion pulse can be detected within a dead time interval τ, regardless of the actual number of secondary ions arriving at the detector. Since typically the time width of a peak is much smaller than the effective dead time (around 50 ns for most instruments),[20] the detection system is said to be "single ion counting" and a maximum of 1 count per primary ion pulse might be detected for any peak, assuming it is not preceded by another peak within the dead time. For the hair image, this condition is reasonable for each nominal mass, which may contain several unresolved peaks due to poor mass resolution. The maximum detectable count per pixel for each unit mass is therefore equal to the total number of ion pulses impacting each pixel. This is marked as a red dotted line on the maximum intensity spectrum on Figure 6.1b. The single ion counting assumption is extremely well satisfied for most of the data, with the minor exception of the intense peak B (marked on the figure) belonging to a major chemical component where the detected intensities of 7 pixels are up to 8 counts larger than the total number of ion pulses, i.e. they are 'fully saturated'.

It is clear that detector saturation is an issue in the hair image. Stephan *et al* proposed a method for intensity correction based on the Poissonian nature of SIMS data. This procedure,

commonly referred to as “dead time correction”, scales the measured secondary ion counts so that the corrected counts is proportional to the actual number of secondary ions impinging on the detector. It is routinely applied to SIMS data and has been demonstrated to be very successful for many data sets.[20-22] To maintain 95% linearity between the detected intensity and true intensity, dead time correction is required when the average detected counts per ion pulse for a single peak exceed 0.1 (blue dotted line on Figure 6.1b). In a recent interlaboratory study,[21] it was found that for 15% of instruments studied, dead time correction was not sufficient to retain 95% linearity when the average detected counts per ion pulse for a single peak exceeds 0.6 (green dotted line on Figure 6.1b). The maximum intensity spectrum in Figure 6.1b therefore enables the rapid diagnosis of detector saturation for different secondary ions, which is impossible using the total ion spectrum where ion intensities are also dependent on the spatial coverage.

Consequently, dead time correction is applied to the hair image to minimise non-linearities before multivariate analysis, using Equation 8 from Reference 22, which is rewritten in matrix notation as follows

$$\mathbf{X} = -m \ln\left(1 - \hat{\mathbf{X}} / m\right) \tag{6.1}$$

where $\mathbf{X}$ is the dead time corrected data matrix, $\hat{\mathbf{X}}$ is the raw data matrix and m is the number of primary ion pulses per pixel. As the detected counts per ion pulse for a single peak approach 1, the corrected intensity approaches infinity, which causes a problem for the 7 fully-saturated pixels for peak B. Several solutions exist for this,[22] and here the peak B intensities in the fully-saturated pixels are simply set to be the value of their most intense nearest neighbour that is non fully-saturated.

Figure 6.2 illustrates the effect and benefit of dead time correction. The intensities of two low mass fragment ions, X and Y, are plotted against each other for each of the 16384 pixels, after the ion images were smoothed by a 3 × 3 averaging (top hat) filter to improve the signal to

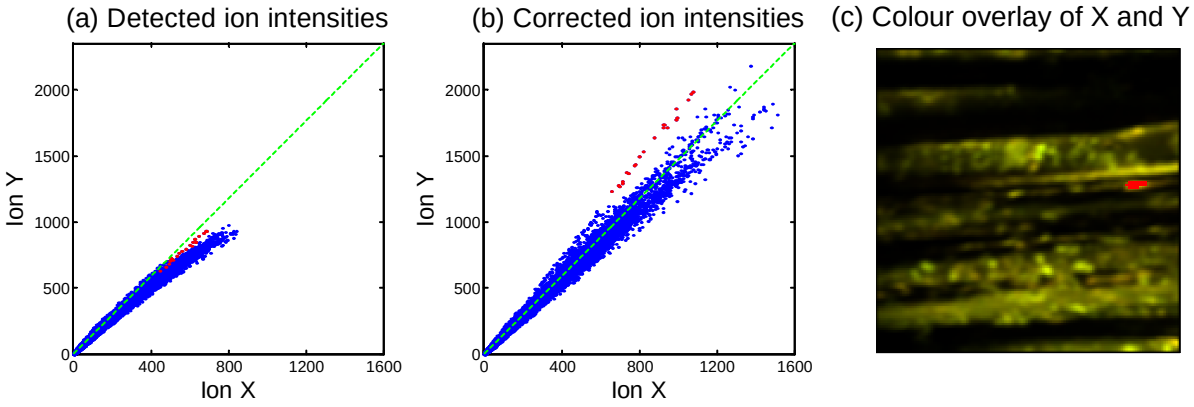

Figure 6.2 Scatter diagrams showing the intensities of ions X and Y for each of the image pixels (a) before and (b) after dead-time correction. The dotted green line shows the general proportionality between the two ions. (c) Overlay of the ion images after dead time correction. A small, localised variation (pixels highlighted in red), which results in a larger Y/X ratio, is difficult to detect without dead-time correction.

noise ratio. Figure 6.2a shows the resulting scatter diagram before dead time correction. Y varies proportionally with X at low intensities (dotted green line), but becomes saturated relative to X at higher intensities. It is difficult to discern any further detail from this plot. Figure 6.2b shows the scatter diagram obtained after dead time correction, plotted on the same scale. Y varies linearly with X throughout the range of intensities along the line of proportionality. Smaller features in the data can now be discerned, for example, a noticeably larger Y/X ratio exists for a group of pixels which are highlighted in red. These pixels are also displayed in red in the colour overlay of the two ion images on Figure 6.2c, and correspond to a localised variation in the image. The different fragment ratio obtained therefore reflects a real feature of the data, which could arise due to surface chemistry (e.g. the existence of extra components producing the same ions in different ratios) or topographical effects. The same pixels are highlighted on Figure 6.2a without dead time correction, where they are masked by the effect of saturation. Figure 6.2 therefore illustrates a dramatic improvement in the detection of a small, localised chemical variation, which would not be possible without dead time correction.

6.3.2 Data scaling

Multivariate analysis seeks to describe the underlying structure of the data and is therefore sensitive to data scaling and transformations.[9,10,23] This is explored in Chapter 5 for a polymer blend system. Conventional multivariate methods assume uniform uncertainty in the data, which is not true in SIMS.[11] Suitable data scaling is therefore required to provide improved noise rejection for multivariate analysis. In this study, three data scaling methods are compared using the hair fibre image – no scaling, Poisson scaling[11] and binomial scaling.[22] These are described in more detail in Chapter 4. In Chapter 5, Poisson scaling is demonstrated to provide superior results for image analysis compared to no scaling, normalisation and variance scaling. This is echoed by other studies in literature.[9,11] However, it is suggested that when dead time correction is required, the corrected data follow a binomial distribution instead of Poissonian distribution, and binomial scaling should be employed.[22]

Conventionally, Poisson scaling and binomial scaling operate in both the image and spectral domains of the data. This means each data point (i.e. the intensity of a particular peak in a particular image pixel) is divided by the product of two values, one containing the uncertainty associated with the sample (i.e. pixel) and one containing the uncertainty associated with the variable (i.e. mass peak). However, due to the extreme topography of the hair sample, a large number of pixels exist with near zero intensities, leading to associated uncertainties that are also close to zero. This causes considerable problems with data scaling, enhancing noise in the analysis and producing inferior PCA results where image noise is interspersed with real chemical features. Here, Poisson and binomial scaling are therefore modified so that they operate in the spectral domain only, that is, each data point is only scaled by the uncertainty associated with the variable concerned. In this case, Poisson scaling is commonly referred to as 'root mean scaling'.[10] Thus, for each column (variable) *k* of the scaled data $\tilde{\mathbf{X}}$ (denoted by $\tilde{\mathbf{x}}_k$),

$$\tilde{\mathbf{x}}_k = \frac{1}{\sqrt{\bar{v}_k}} \times \mathbf{x}_k \tag{6.2}$$

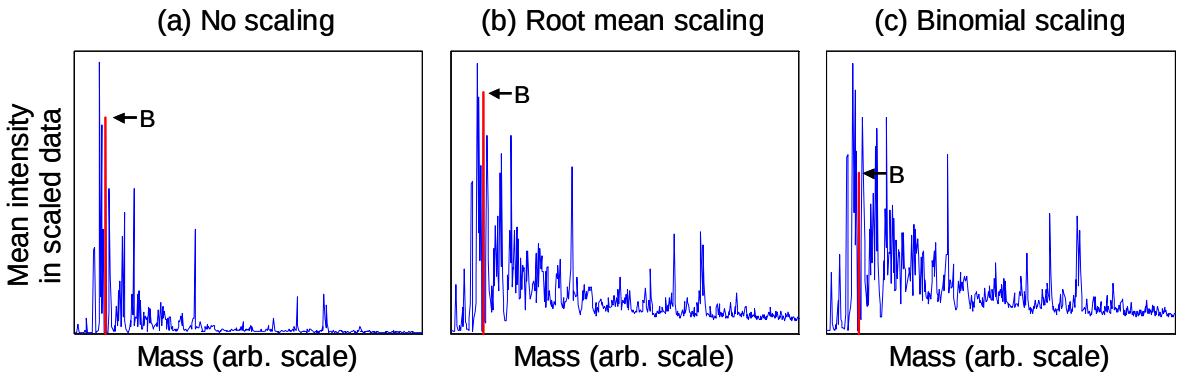

Figure 6.3 Mean spectrum of the dead-time corrected data matrix, after (a) no scaling, (b) root mean scaling and (c) binomial scaling, applied to the spectral domain only. This shows the enhancement of weak peaks using root mean scaling, and the additional suppression of saturated peaks using binomial scaling, e.g. peak B which is highlighted in red and marked with an arrow.

where $\bar{v}_k$ is the k^{th} column mean of the variance matrix $\mathbf{V}$, and $\mathbf{x}_k$ is the k^{th} column of the dead time corrected data matrix **X**. For root mean scaling, $\mathbf{V}$ is simply given by

$$\mathbf{V} = \mathbf{X} \tag{6.3}$$

And for binomial scaling, **V** can be calculated element by element as follows[22]

$$\mathbf{V} = \frac{\hat{\mathbf{X}}}{1 - \hat{\mathbf{X}}/m} = m\left(\exp\left(\frac{\mathbf{X}}{m}\right) - 1\right) \tag{6.4}$$

The effects of data scaling on the data are now discussed. At very low intensities, the uncertainty estimates for Poisson and binomial scaling are equal. However, at higher intensities, the uncertainties estimated using binomial scaling are increased beyond the Poissonian estimates, due to the additional error in extrapolating the detected intensities to account for increasing numbers of lost counts due to detector saturation. Figure 6.3 shows the mean spectrum of the dead time corrected data after no scaling, root mean scaling and binomial scaling in the spectral domain (i.e. the mean spectrum of $\tilde{\mathbf{X}}$). Without scaling, the

data are dominated by intense low mass peaks. Root mean scaling enhances the importance of high mass, low intensity peaks, which are associated with smaller uncertainty from Poisson counting statistics. Binomial scaling produces very similar results to root mean scaling, except for strongly saturated peaks which are associated with large uncertainty after dead time correction and are consequently suppressed, for example the highly saturated peak B highlighted in red. Binomial scaling thus prevents highly saturated, noisy peaks from unduly influencing multivariate analysis over weaker peaks that may describe more chemically meaningful variations.

Finally, the use of data scaling in multivariate analysis is associated with several important subtleties. It is important to distinguish between the description of the scaled data $\tilde{\mathbf{X}}$ (which is said to be in 'scaled space' or 'weighted space') and the original unscaled data $\mathbf{X}$ (which is said to be in 'physical space'). This is explained in more detail in Reference 11. Here, the popular convention is followed and the loadings obtained from the multivariate analysis of the scaled data are back transformed, so that they reflect variations in the original data prior to data scaling.[11,22] Thus, for the k^{th} column of the loadings matrix $\tilde{\mathbf{P}}$ (denoted by $\tilde{\mathbf{p}}_k$) in scaled space, which is obtained from the multivariate analysis of the scaled data $\tilde{\mathbf{X}}$,

$$\mathbf{p}_k = \sqrt{\bar{v}_k} \times \tilde{\mathbf{p}}_k \tag{6.5}$$

where $\mathbf{P}$ with columns given by $\mathbf{p}_k$ is now the loadings in physical space, reflecting the variations in the original dead time corrected data $\mathbf{X}$. After back transformation, the loadings and scores are then renormalized so that the squares of the loading peaks sum to one, i.e. the loadings become unit length vectors, as is usual in PCA.

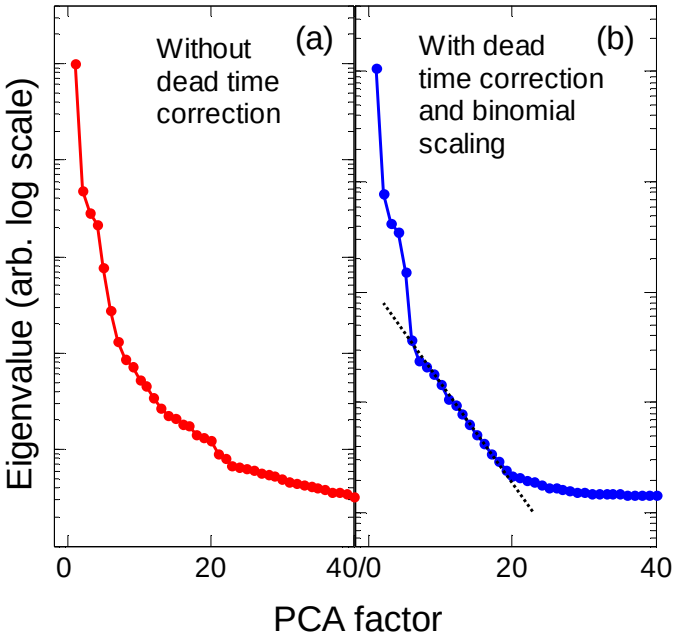

Figure 6.4 Eigenvalue diagrams obtained for PCA (a) without dead time correction and (b) with dead-time correction and binomial scaling. The dotted line shows the line used for the scree test.

6.4 Results and discussion

6.4.1 Principal component analysis

PCA is applied to the hair image after no scaling, root mean scaling and binomial scaling, without mean centering. Although mean centering is commonly used in PCA to describe the differences between samples rather than their variations from zero intensities, it is not helpful here since the mean of the hair data is very close to the origin because of large background areas with nearly zero counts. Mean centering therefore does not produce substantially different PCA results. Examples of eigenvalue diagrams obtained in PCA are shown in Figure 6.4. Without dead time correction (Figure 6.4a), no clear turn-off can be observed for the scree test due to the large non-linear intensity variations in the data. In contrast, for all scaling methods applied after dead time correction, clear eigenvalue diagrams are obtained, as can be seen for binomial scaling in Figure 6.4b. The scree test (dotted line) shows 5 major factors in the data above the “scree”, although minor variations can be observed up to around

PCA factor	Fraction of variance captured, %			
	No dead time correction	With dead time correction		
	No scaling	No scaling	Root mean scaling	Binomial scaling
1	89.37	85.32	84.42	83.80
2	4.33	8.49	6.55	4.58
3	2.59	2.51	4.39	4.92
4	1.93	2.02	2.34	2.90
5	0.71	1.01	1.39	2.25
Total	**98.93**	**99.36**	**99.08**	**98.44**

Table 6.1 The fraction of variance (%) captured by the first five PCA factors for different data scaling methods, with and without dead time correction. For PCA applied after data scaling, the variance captured in the physical space is shown.

PCA factor 30. The minor variations could arise from sample topography, which introduces severe artefacts in SIMS images and spectra caused by the shadowing of the secondary ions, primary ions scattering and differential sample charging, which are discussed in Chapters 2 and 3. It may also arise from severe detector saturation that cannot be compensated by dead time correction, minor chemical variations or other sources of non-linearity. These effects are complex and generally very difficult to interpret. This study therefore concentrates on the identification and localisation of the major chemical constituents on the hair surface, focusing on the first 5 major PCA factors only.

The percentage variance captured for each scaling method, with and without dead time correction, is shown in Table 6.1. For PCA applied after data scaling, the variance captured in the physical space is calculated, following Smentkowski *et al.*,[24]

$$\text{Variance captured in factor } n = \mathbf{p}_n \mathbf{p}'_n \mathbf{t}_n \mathbf{t}'_n \tag{6.6}$$

where $\mathbf{p}_n$ and $\mathbf{t}_n$ are row vectors containing the n^{th} row of the loadings and scores in the physical space, **P** and **T**. For all methods, the first 5 PCA factors account for over 98% of the total variance in the data. First, we can compare the variance captured before and after dead time correction, without data scaling. Since dead time correction increases the linearity of the data, a larger percentage of variance can be described using a linear combination of the first 5

PCA factors. However, the difference is small since the level of detector saturation is in fact reasonably low for the majority of the data points. Next, we can compare the variance captured after dead time correction, with or without scaling. PCA after data scaling captures less variance in the first five PCA factors, since PCA without data scaling gives the best possible fit to the total variance of the data, while PCA with data scaling may be fitted to chemically relevant variance only and is therefore a poorer fit to the original noisy data.[11] Here, the small differences observed result from the high signal to noise ratio of the data due to the large number of image scans used. It is interesting to observe that, for binomial scaling, PCA factor 3 captures more variance in the physical space compared to PCA factor 2. By employing root mean scaling and binomial scaling, a factor capturing more variance in the scaled data reflects more chemically relevant (less noisy) information, even though this may be equivalent to less variance captured in the original (physical) data, which is noisy. PCA factors are therefore sorted by their variance captured in the scaled space rather than variance captured in the physical space, causing the observed discrepancy.

We can now move onto the discussion of the PCA results. For all scaling methods, the scores and loadings obtained for the first 5 PCA factors are similar. An example is shown in Figure 6.5 for binomial scaling. The loadings have been back transformed to represent variations in the physical space. Scores are plotted on a two-way colour scale, where pixels with positive and negative scores are displayed on a red (‘hot’) and blue (‘cold’) colour scale, respectively.[13] The advantage of this is that pixels with zero scores, which do not contribute to the variance described in that factor, are conveniently displayed in black.

Regardless of data scaling methods, PCA successfully highlights major trends and variations in the scores images, as well as important peaks in the loadings. The first PCA factor describes the overall intensity variation throughout the image arising from the differences between the hair sample and the background area, which represents the largest source of variance in the data. PCA factors 2 – 5 describe the chemical variations on different areas of the

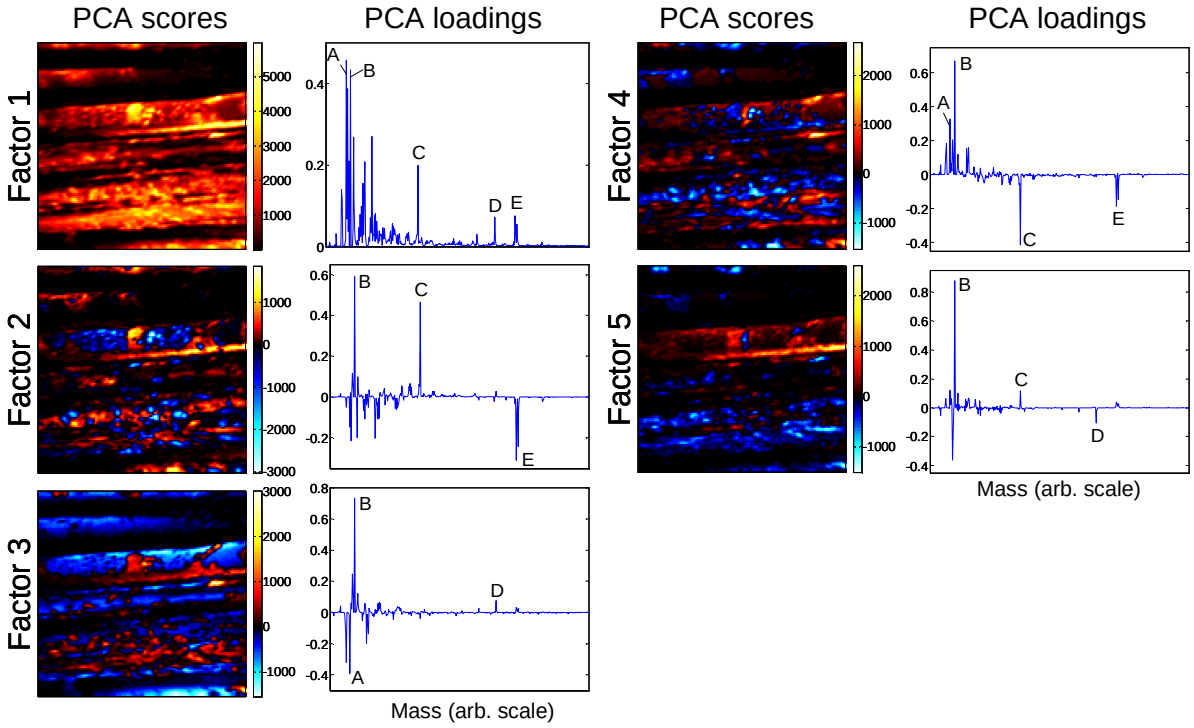

Figure 6.5 PCA results for the hair fibre data after binomial scaling in the spectral domain, showing loadings and scores on the first 5 factors. The loadings have been back transformed to represent variations in the physical space.

hair surface, which are driven by chemical components with characteristic peaks A to E. However, despite identifying these peaks that contribute strongly to the chemistry of the sample, PCA loadings do not provide full fingerprint spectra of the chemical components by which they can be identified directly. Similarly, although PCA scores images show enhanced chemical contrast between different regions of the sample, they do not facilitate a direct interpretation of the surface coverage of different chemical components. In addition, characteristic peaks arising from each of the chemical components appear in more than one PCA factor, and peaks that are anti-correlated in one factor are correlated in another (e.g. peaks C and E in factor 2 and 4), making it virtually impossible to localise individual chemical components using the scores images. These problems arise because PCA factors are constrained to be orthogonal and optimally capture the largest variance in the data. The PCA loadings are therefore abstract combinations of chemical spectra that reflect the largest correlation and anti-correlation of various components on different areas of the image. As a

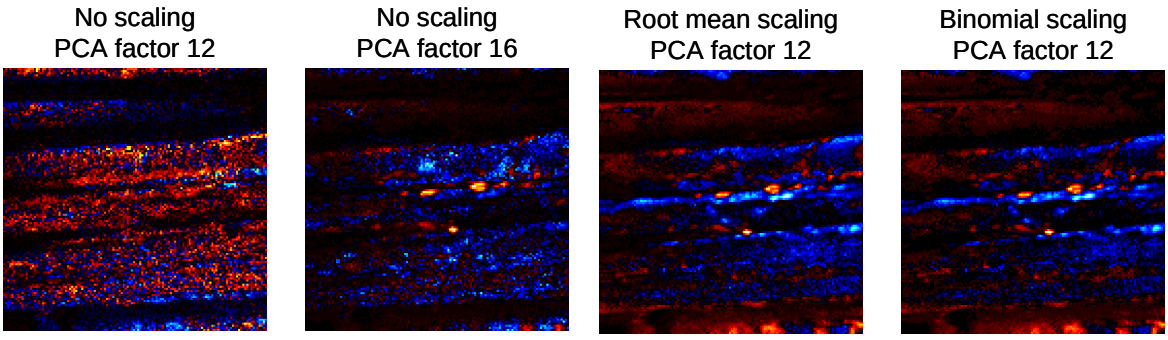

Figure 6.6 Selected PCA scores images using different data scaling methods. A localised feature is identified in PCA factor 12 using root mean scaling and binomial scaling. This is not apparent without data scaling until PCA factor 16, while factor 12 describes larger but less chemically meaningful variations due to noise.

result, information relating to the identity and distribution of individual chemical components is spread over several factors, hindering the direct and rapid chemical interpretation of the PCA results.

6.4.2 Comparison of data scaling using principal component analysis

While root mean scaling and binomial scaling produce very similar results, the comparison of higher PCA factors obtained using different data scaling methods reveals that both methods are superior to PCA with no scaling, especially for the discrimination of minor variations in the data (i.e. features beyond PCA factor 5) from noise. Meaningful minor variations tend to be spatially localised, whether they are caused by topography, detector saturation or small chemical features. In contrast, noise due to counting statistics and dead time correction is typified by pixel-to-pixel variations. An example of this is shown in Figure 6.6. A localised feature is identified in PCA factor 12 using root mean scaling and binomial scaling. This is not apparent without data scaling until PCA factor 16, while factor 12 describes larger but less chemically meaningful variations due to noise. With scaling, localised variations are observed for all of the first 20 PCA factors, whilst without scaling factors that describe noise features are interspersed between factors that describe localised variations. Data scaling is therefore

essential for identifying minor features in the presence of noise, although it is very difficult from this to determine whether root mean scaling or binomial scaling produces better PCA results.

6.4.3 Multivariate curve resolution

MCR with non-negativity constraints is also applied to the hair image. The number of factors to be resolved is fixed at five, as identified earlier as the number of major components accounting for more than 98% of the total variance in the data. It is important to note that the number of factors in MCR has a large effect on the results obtained. In PCA, the factors are computed sequentially and a unique solution is produced for each data set regardless of the number of factors the user chooses to retain for study, whilst in MCR, the factors are resolved simultaneously using an iterative algorithm and different results are obtained depending on the number of factors chosen. From the study of a simple mixed organic system in Chapter 5, MCR was found to be the most suitable for the identification of unknown mixtures rather than the detection of small variations in the data. Here, the focus is therefore on the identification and localisation of the five major chemical constituents on the surface of the hair without attempting to identify minor features such as those shown in Figure 6.6. In the following, MCR results are ordered by the relative importance of each factor as calculated using Equation 6.6. However, since MCR factors are not orthogonal, these are not equal to the variance captured on each factor, which cannot be easily defined.[24]

For all data scaling methods applied (no scaling, root mean scaling and binomial scaling), the MCR results obtained are extremely similar. MCR is therefore robust to data scaling. Results for binomial scaling are shown in Figure 6.7. Four chemical components are identified clearly on the hair surface (MCR factor 1 and 3 – 5), in addition to one component (MCR factor 2) characteristic of the hair substrate itself. The MCR loadings on each factor resemble the complete SIMS spectrum of the component, showing its characteristic peaks (A – E) along

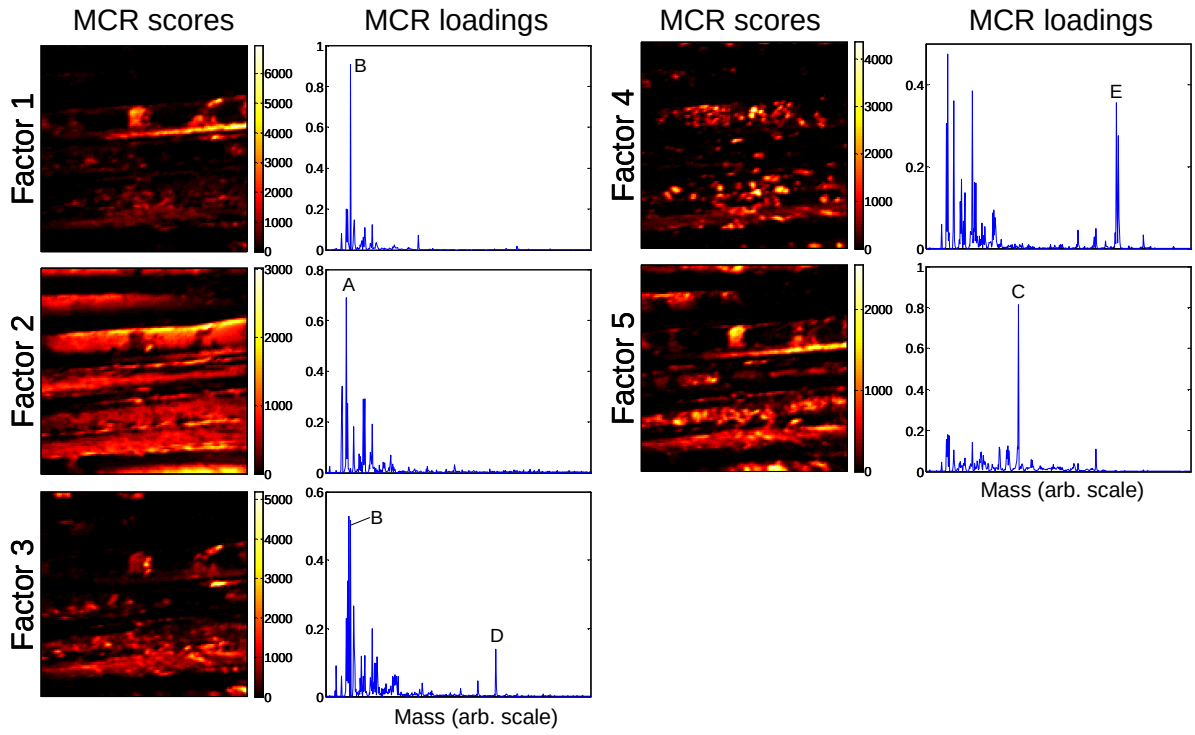

Figure 6.7 MCR results for the hair fibre data after binomial scaling in the spectral domain, showing loadings and scores on 5 factors. The loadings have been back transformed to represent variations in the physical space.

with a full fragmentation pattern in the low mass region, and the scores reveal directly and unambiguously the distribution of the components on the surface. This represents a significant improvement from manual analysis and PCA, where identification is often based on the correlation of key ions only. In particular, using manual analysis or PCA it is very difficult, if not impossible, to obtain the full spectra of individual chemical components using only the known characteristic peaks of each component. This can be demonstrated using the hair fibre image, as follows. Using the characteristic peaks A – E identified by PCA, an attempt is made to regenerate the chemical spectrum of each of these components manually from the raw data by selecting the pixels where each characteristic peak is most intense (i.e. more than 50% of its maximum value in the image) and summing the spectra from these pixels. The result for this analysis is shown in Figure 6.8. In total, less than 6% of the image pixels are used in the regeneration of spectra, and of these pixels, less than 16% are used for more than one chemical component. Despite this, due to the complexity of the sample and the spatial overlap

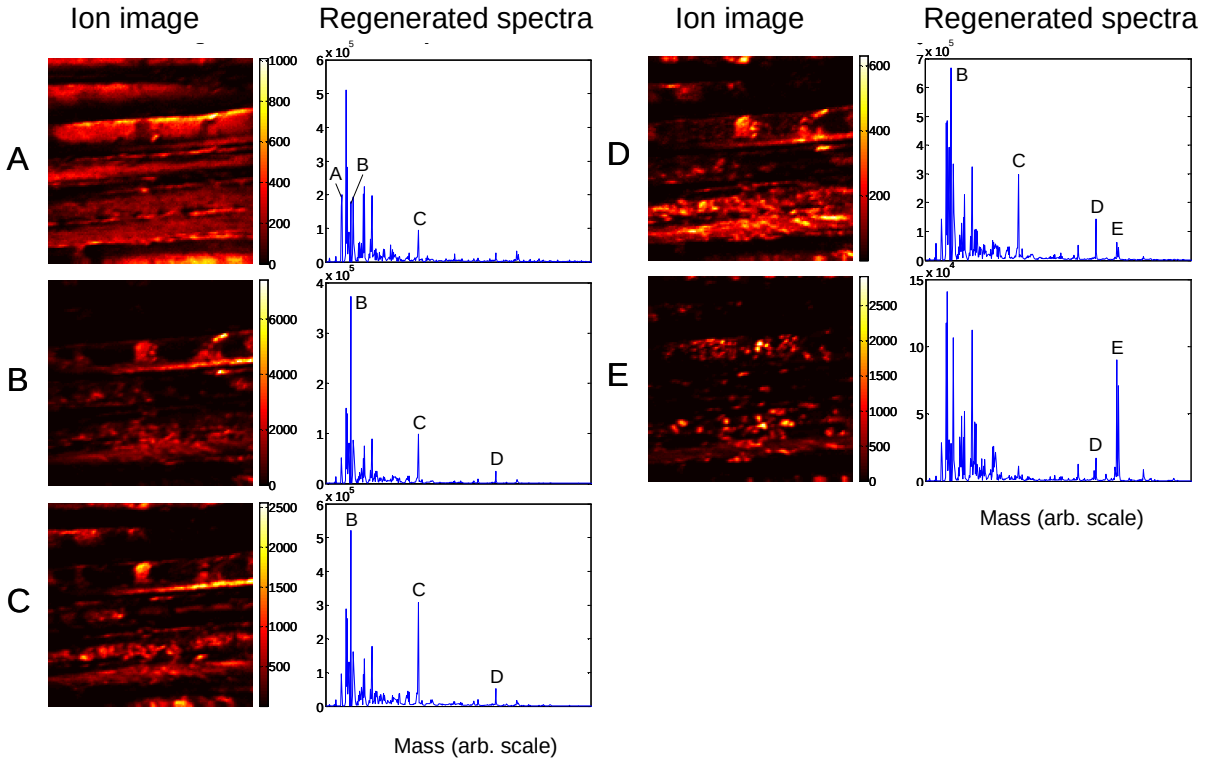

Figure 6.8 Ion images of the characteristic peaks A – E, identified from PCA, and spectra of individual chemical components generated manually from the raw data, using the pixels where the intensities of the characteristic peaks are more than 50% of their maximum values in the image.

of chemical components on the surface of the hair, the regenerated spectra are strongly mixed (containing characteristic peaks from more than one component) and therefore do not represent the pure spectra of these components. In contrast, the MCR results shown in Figure 6.7 enables the straightforward identification and localisation of the chemical components using their complete resolved spectra without any prior knowledge of the system, and therefore provides superior results compared to manual analysis methods.

Using MCR results, the analyst can draw important conclusions about the multi-component hair surface treatment that would be extremely difficult to obtain with manual analysis. In this case, the multi-component formulation is chemically complex and comprises of a number of major ingredients, which may themselves be comprised of a number of chemical constituents. For traditional manual analysis, the pure spectra of each ingredient had been obtained to facilitate the interpretation of the complex hair image. Characteristic peaks D and E were both

found to originate from the same three ingredients, which are chemically similar and difficult to distinguish using their SIMS spectra. An analyst must therefore treat these three ingredients as one and study only the combined intensities of D and E peaks. However, MCR results of the hair data reveal that important in-situ surface interactions have occurred between the complex ingredients, leading to the complete segregation of chemical components D and E on the surface of the hair, thereby giving different spatial distribution for the two ions. This information is tremendously important to scientists formulating the hair treatments, and is immediately obvious from MCR results. It would be easily missed in manual analysis, where the two chemical components are identified as one using *a priori* information from the spectra of the original ingredients. This illustrates the power of multivariate approaches, which allow analysts to focus on the sample of interest without being restricted by the type of reference data or spectra available, especially since reference spectra obtained from individual ingredients may not be representative of the surface chemistry on the sample of interest, and may therefore give misleading or incomplete results.

6.4.4 Comparison of data scaling using multivariate curve resolution

Although MCR is robust and is largely unaffected by data scaling, important insights can be gained by the careful, detailed study of the small differences which arise with different data scaling methods. Since MCR loadings and scores are fitted to the PCA reproduced data, it is advantageous to employ root mean scaling or binomial scaling to ensure the best noise rejection in the analysis. In effect, MCR transforms the PCA factors with the constraints that the new factors must be non-negative while still explaining the maximum variance possible in the PCA reproduced data. As a result, MCR factors are no longer orthogonal and MCR scores and loadings on different factors can be correlated. This correlation is usually manifest as increased similarities between the scores images on different factors, or the mixing of spectra in the MCR loadings, which leads to the characteristic peaks from one chemical component being observed in more than one factor. This can be seen, for example, for peak B in the binomially scaled data (Figure 6.7), which is observed strongly in MCR factors 1 and 3.

MCR results	Average correlation coefficient, *r*		
	No scaling	Root mean scaling	Binomial scaling
Scores	0.369	0.328	0.303
Loadings	0.292	0.355	0.379

Lower correlation coefficient for scores
Higher correlation coefficient for loadings

Table 6.2 The average correlation coefficient *r* between loadings or scores on different MCR factors. The loadings have been back transformed to represent variations in the physical space.

Similarly, peak D, which is characteristic of MCR factor 3, is also weakly present in MCR factors 4 and 5.

For the polymer blend study in Chapter 5, the correlations between MCR scores on different factors are explored in detail using scatter and polar plots. Here, for simplicity, the correlation coefficient *r* is used, which is obtained by dividing the covariance of two scores or loadings vectors by the product of their standard deviations. A correlation coefficient of zero indicates orthogonality (as would be the case for PCA loadings and scores on different factors), while a coefficient of +1 indicates collinearity and a coefficient of –1 indicates anti-collinearity. Table 6.2 shows the average correlation coefficient *r* between loadings or scores on different factors, for MCR models with different scaling methods. A weak but significant positive correlation is found between each pair of MCR scores and loadings. The average correlation of the loadings is found to be the largest for binomial scaling, reduces for root mean scaling and is the smallest for no scaling. Interestingly, the reverse trend is observed for the average correlation of the scores. It is apparent that the correlations of the scores and loadings in MCR analysis are fundamentally related.

This relationship between loadings and scores is illustrated graphically in Figure 6.9, for different MCR models of the same data. This shows two MCR models for 15 arbitrary samples (circles) measured over two variables, m_1 and m_2. Figure 6.9a and 6.9c show the

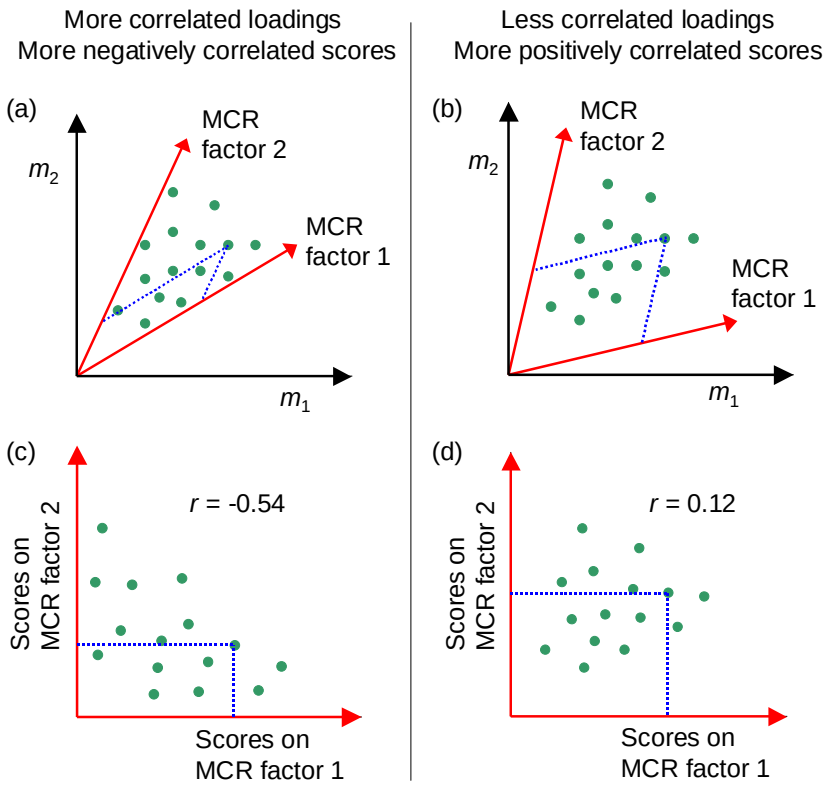

Figure 6.9 An illustration showing two different MCR models of the same data, for 15 samples (circles) measured over two variables. (a) and (b) show the data plotted in the original variable space. Red arrows show the directions of the MCR factors, and dashed lines show the oblique projection of a sample onto the MCR factors, which give the MCR scores. (c) and (d) show the scores on MCR factor 2 against MCR factor 1 for the two MCR models. The model with more correlated loadings (smaller angle between MCR factors) gives more negatively correlated scores, while the model with less correlated loadings (larger angle between MCR factors) give more positively correlated scores.

MCR model with more correlated loadings (smaller angle between the MCR factors), while Figure 6.9b and 6.9d show the MCR model with less correlated loadings (larger angle between the MCR factors). In Figure 6.9a and 6.9b, the data are plotted in the original variable space, with red arrows denoting the directions of the MCR factors. The MCR scores are given by the oblique projection of the sample onto the factors, which are shown in dashed lines for one sample as an example. In Figure 6.9c and 6.9d, we plot the scores on the two MCR factors against each other in an approach similar to that in Chapter 5. The correlation coefficient r between the scores on the two MCR factors are computed for each model and

displayed on the figure. It is clear that an increased correlation of the loadings results in a decreased correlation coefficient of the scores. This does not merely reduce the correlation of the scores towards zero but can cause a negative correlation coefficient, i.e. anti-correlation between the score images.

This result has important consequences for identifying the data scaling method which provides the best description of the data. The trend observed in the average correlations for different scaling methods, displayed in Table 6.2, is found to be generally true for all SIMS data, real or computer simulated, and is unrelated to topography or chemical complexity. A decision must therefore be made to select the method that gives either the lowest average correlation in the scores (i.e. most dissimilar spatial distribution for resolved components), or the lowest average correlation in the loadings (i.e. least mixing of the resolved spectra). Here, we can argue that for SIMS data the best MCR model of the data is the one giving the largest anti-correlation of the scores (i.e. an average correlation coefficient closest to –1). Since SIMS is extremely surface sensitive, typically only the topmost monolayer could be observed regardless of any physical overlap of the different chemical components. As a result, for chemical components that are segregated, only one component could be detected from any one location except when the diameter of the primary ion beam is larger than the spatial extent of the surface chemical features, for example if small islands of different components exist alongside each other. Although this is a very simplified argument, it is helpful in selecting the most appropriate data scaling method. The consequence of the surface sensitivity in SIMS is that for spatially resolved features, their observed distributions must show the maximum spatial distinction, and the relevant images must therefore be maximally anti-correlated with each other. Hence, the most realistic description of the data is obtained by having the lowest (most negative) average correlation coefficient r between the different scores images, as they directly reflect the localisation of different chemical components. This is consistent with the results in Chapter 5, where the largest angular separation on a polar plot was used to indicate the best MCR model.

Perhaps somewhat counter-intuitively, one can also explain why the increased positive correlation (or mixing) of the loadings spectra, which is associated with more anti-correlated scores images, can also be the result of a more physically realistic MCR model. Naively, we might prefer less mixing in the resolved spectra, for example if characteristic peak D from Figure 6.7 is observed only in MCR factor 3 and is absent from factor 4 and 5, as is the case without data scaling. However, SIMS data are complex and noisy, and therefore attempts to obtain simpler and less correlated loadings spectra may in fact result in spectra that are less faithful to the real experimental data. This may be explained as follows. Firstly, for a complex organic mixture, it is clear that the fragments associated with common functional groups should not be assigned to either one factor or another, but instead should be shared amongst different factors. This would result in loadings that are more correlated. Secondly, it is very possible that the mixing of spectra, such as those observed in Figure 6.7, may be real features. For the complex multi-component hair treatment explored here, the ingredients interact on the surface of the hair, causing important segregation effects seen earlier. It is therefore likely that chemical mixing can also occur, where small amounts of one component can be dissolved within another during the surface treatment, resulting in chemical mixing in the experimental data obtained. Thirdly, it is widely known that the noise on different variables in SIMS are uncorrelated.[11] Thus, it is reasonable to expect that, for an MCR model describing meaningful chemical variations, the loadings may be more correlated compared to an MCR model describing noisy (but uncorrelated) features of the data. Finally, we can see from Figure 6.9 that model (a), which has loadings that are more correlated, is a more effective and unique description of the data compared to model (b), which has loadings that are less correlated. The increased correlation in the loadings spectra is therefore consistent with a physically realistic MCR model.

Using these arguments, the best data scaling method for the MCR analysis of the hair data can finally be identified using Table 6.2. For all scaling methods, positive correlations are found between the scores on different MCR factors, due to the topography of the sample which means the different chemical components are all spatially co-located on the fibre surface

rather than the background area. Nevertheless, binomial scaling gives the lowest average correlation coefficient *r* between scores on different MCR factors, and is therefore the best description of the data out of the scaling methods studied here. The result is not unsurprising, due to the strong detector saturation in the data and the need to account for increased noise variances arising from the dead time correction. At lower count rates, binomial scaling converges towards Poisson scaling (or root mean scaling, in the case where it is applied to the spectral domain only), which has been demonstrated to be an excellent data scaling method for unsaturated data.[9,11]

6.5 Conclusions

In this study, the detailed application of multivariate analysis methods has been demonstrated on a complex multi-component hair fibre image with topography. Detector saturation is an important issue and the use of dead time correction combined with suitable data scaling is essential for the optimal discrimination of chemical features from image noise. For samples with severe topography, it is also important that data scaling methods are modified to operate in the spectral domain only. PCA successfully highlights important trends and variations in the data, but cannot provide direct information relating to the identities and distributions of chemical components, while MCR provides factors that resemble the complete SIMS spectra and distribution images of chemical components, making it more intuitive and easier to interpret than PCA. Binomial scaling is identified as the most appropriate data scaling method, giving the most distinct chemical distribution images using MCR. Using these results, an important surface interaction is revealed, which occurred between multiple ingredients in a complex multi-component hair treatment, and caused chemical segregation that would be difficult to identify with manual analysis. With a careful approach and suitable data scaling, the speed, automation and accuracy of multivariate analysis make it superior to traditional analysis methods, even in the presence of *a priori* knowledge of the system.

References

1 C. Zvial, The Science of Hair Care (Marcel Dekker, New York, 1986).

2 J. A. Staudgel, K. Bunasky, C. J. Gamsky, M. S. Wagner, K. J. Stump, J. M. Baker, R. L. Marple, and J. H. Thomas, Journal of Cosmetic Science **58,** 637 (2007).

3 B. A. Bernard, A. Franbourg, A. M. François, B. Gautier, and P. Hallegot, International journal of cosmetic science **24,** 1 (2002).

4 S. B. Ruetsch, Y. K. Kamath, A. S. Rele, and R. B. Mohile, Journal of Cosmetic Science **52,** 169 (2001).

5 J. S. Dalton, G. C. Allen, P. J. Heard, K. R. Hallam, N. J. Elton, M. J. Walker, and G. Matz, Journal of Cosmetic Science **51,** 275 (2000).

6 G. Gillen, S. Roberson, C. Ng, and M. Stranick, Scanning **21,** 173 (1999).

7 B. T. Wickes, Y. Kim, and D. G. Castner, Surface and Interface Analysis **35,** 640 (2003).

8 L. A. Klerk, A. Broersen, I. W. Fletcher, R. van Liere, and R. M. A. Heeren, International Journal of Mass Spectrometry **260,** 222 (2007).

9 M. S. Wagner, D. J. Graharn, and D. G. Castner, Applied Surface Science **252,** 6575 (2006).

10 B. J. Tyler, G. Rayal, and D. G. Castner, Biomaterials **28,** 2412 (2007).

11 M. R. Keenan and P. G. Kotula, Surface and Interface Analysis **36,** 203 (2004).

12 B. J. Tyler, Applied Surface Science **252,** 6875 (2006).

13 S. J. Pachuta, Applied Surface Science **231-2,** 217 (2004).

14 M. L. Pacholski, Applied Surface Science **231-2,** 235 (2004).

15 J. Schwieters, H. G. Cramer, T. Heller, U. Jurgens, E. Niehuis, J. Zehnpfenning, and A. Benninghoven, Journal of Vacuum Science & Technology a-Vacuum Surfaces and Films **9,** 2864 (1991).

16 R. Tauler, A. de Juan, Multivariate Curve Resolution Homepage <http://www.ub.edu/mcr/> (2008).

17 J. Jaumot, R. Gargallo, A. de Juan, and R. Tauler, Chemometrics and Intelligent Laboratory Systems **76,** 101 (2005).

18 H. F. Kaiser, Psychometrika **23,** 187 (1958).

19 J. L. S. Lee and I. S. Gilmore, in *Surface Analysis – The Principal Techniques*, 2nd ed., edited by J. C. Vickerman and I. S. Gilmore (Wiley, Chichester, 2008), p. 563.

20 T. Stephan, J. Zehnpfenning, and A. Benninghoven, Journal of Vacuum Science & Technology a-Vacuum Surfaces and Films **12,** 405 (1994).

21 J. L. S. Lee, I. S. Gilmore, and M. P. Seah, Surface and Interface Analysis**,** in press (2011).

22 M. R. Keenan, V. S. Smentkowski, J. A. Ohlhausen, and P. G. Kotula, Surface and Interface Analysis **40,** 97 (2008).

23 M. S. Wagner, D. J. Graham, B. D. Ratner, and D. G. Castner, Surface Science **570,** 78 (2004).

24 V. S. Smentkowski, S. G. Ostrowski, and M. R. Keenan, Surface and Interface Analysis **41,** 88 (2009).

Chapter 7 – Artefacts in the sputtering of inorganics by C_{60}^{n+}

7.1 Introduction

New cluster primary ion beams, such as C_{60}^{n+}, have revolutionised the capability for the analysis of complex molecular and organic surfaces by SIMS and opened up new analytical potentials in the molecular depth profiling of organic materials. This is critical in important areas of technological developments, such as organic electronics,[1] drug delivery systems,[2-4] tissue engineering[5,6] and biological analysis.[7-9] However, despite major efforts in the field, the mechanism behind sputtering using cluster ion beams in secondary ion mass spectrometry (SIMS) is not yet well understood. The traditional linear cascade theory for sputtering using monatomic ions[10,11] no longer applies. Several mechanisms have been proposed for sputtering using cluster ion beams, such as thermal evaporation from the area where a dense collision cascade is propagating ('thermal spike'),[12-14] free expansion of super-critically heated subsurface volume ('jet explosion')[15,16] and mesoscale collective motion.[17] There are also practical issues that require resolution, for example sputter induced surface topography, which degrades the depth resolution obtainable in SIMS depth profiling.[18-21] In addition, the usage of C_{60}^{n+} cluster ion beam is associated with the deposition of carbon on the sample surface.[22,23] This is shown to be both time and fluence dependent.[19,22] There is as yet no explanation for why C_{60}^{n+} is able to sputter through some material but not others. In the present study, silicon, gold and platinum samples are used to understand the basic issues in C_{60}^{n+} sputtering, focusing on sputtering yields, topography formation and carbon deposition. The use of bulk elemental targets removes effects associated with complex sample chemistry and allows the comparison of data with sputtering theories.[14] This is of fundamental and practical importance, and a quantitative understanding of C_{60}^{n+} sputtering is urgently required if its potential analytical capabilities in organic SIMS depth profiling for novel systems, such as organic electronics and drug delivery, are to be realised.

7.2 Experimental

The silicon sample used here was obtained from a cleaned (100) wafer, and gold and platinum were polished polycrystalline samples from a previous study.[11] These were obtained from Geller Micro Analytical (Geller Micro Analytical Laboratory, Topsfield, MA, USA) and were commercially polished with 1 μm diamond paste. No further sample preparation was carried out on these samples. Sputtering and SIMS analysis were carried out using an ION-TOF TOF-SIMS IV instrument (ION-TOF GmbH, Muenster, Germany). The instrument is equipped with C_{60}^{n+} and Bi_m^{n+} primary ion guns, mounted on opposite azimuths and at 45° to the surface normal. Sputtering was carried out with the C_{60}^{n+} (n = 1 – 3) ion source. A range of ion energies of 5 – 30 keV were achieved by combining the selection of singly, doubly and triply charged ions with varying source voltages from 5 – 10 kV. Accurate sputter yields on the silicon, gold and platinum samples are determined using the methodology developed in Reference 11. Micrometre sized craters are sputtered into the surface of flat clean samples before measuring their volume using atomic force microscopy (AFM). For the reliable measurement of the volumes of sputter craters using AFM, which has a maximum raster area of 100 μm × 100 μm, a good C_{60}^{n+} beam focus of < 15 μm is required. This is achieved by defocusing the ion beam prior to an aperture before refocusing it onto the sample target. This reduces the ion current incident on the target such that an average value of 0.27 nA is achieved. Two or three craters are sputtered on each sample at each energy to check for consistency. Using an average primary ion dose of 1.3×10^{11} ions, the average dimension of the craters obtained is 8.1 μm by 10.7 μm wide, with a depth of 0.71 μm.

The volumes of the sputtered craters were measured using a Park Autoprobe CP AFM instrument (Park Systems Inc., Santa Clara, CA, USA) operating in contact mode in air. The *x*- and *y*-axes of this instrument were calibrated stably to 0.1% and the *z*-axis to < 0.7% for the silicon sample. The Geller samples (gold and platinum) have different sample heights, causing a further error of ~ 2.8% in the *x* and *y*-axes calibrations. This is approximately corrected using a previous calibration curve obtained as a function of sample height. AFM images of 100 μm × 100 μm are acquired over the sputtered craters and the *z* detector signal is

used to give topographic maps of the surface. A roughly parabolic curvature is present in all the images due to the *z* movement of the AFM scanner. The crater volumes were measured by transferring the raw topography data onto a custom program in MATLAB (The MathWorks, Inc., Natick, MA, USA). The original flat surface is still represented by ~ 80% of the field of view and this is used to reference the original position of the surface in the region of the crater. The image can therefore be 'flattened' using a second order plane correction excluding the crater region. The sputtered volume is then deduced from the summation of the height differences in each pixel within the crater region. In addition to the sputter yield measurements, high-resolution AFM images are obtained with areas of 10 μm × 10 μm of the crater bottoms to measure the extent of topography formation caused by sputtering.

To study the chemical composition of the crater bottoms, SIMS analyses were also carried out on freshly sputtered 12 keV craters on silicon. Secondary ion images were obtained over the sputtered craters using a high-resolution Bi^+ liquid metal ion gun in high current bunched mode, operated at 25 keV energy. Images were acquired with a field of view of 250 μm × 250 μm over a raster of 128 × 128 pixels. Finally, depth profiles were obtained on a 10 μm × 10 μm area on the bottom of 12 keV craters on silicon, using Bi^+ ions at 25 keV. Sputtering and analysis were done simultaneously using the imaging mode with a total ion dose of 9.36×10^9 ions over 500 seconds, and the depth profiles were subsequently reconstructed from the raw data.

7.3 Results and discussion

7.3.1 Sputtering yields of inorganics by C_{60}^{n+}

Figure 7.1 shows the flattened AFM images of silicon wafers, after bombardment by C_{60}^{n+} at various energies. Figure 7.2 shows example line profiles obtained from the flattened AFM images of gold after bombardment. From these images, the sputtering yields are calculated and these are plotted in Figure 7.3 for silicon, gold and platinum for $5 \leq E \leq 30$ keV.

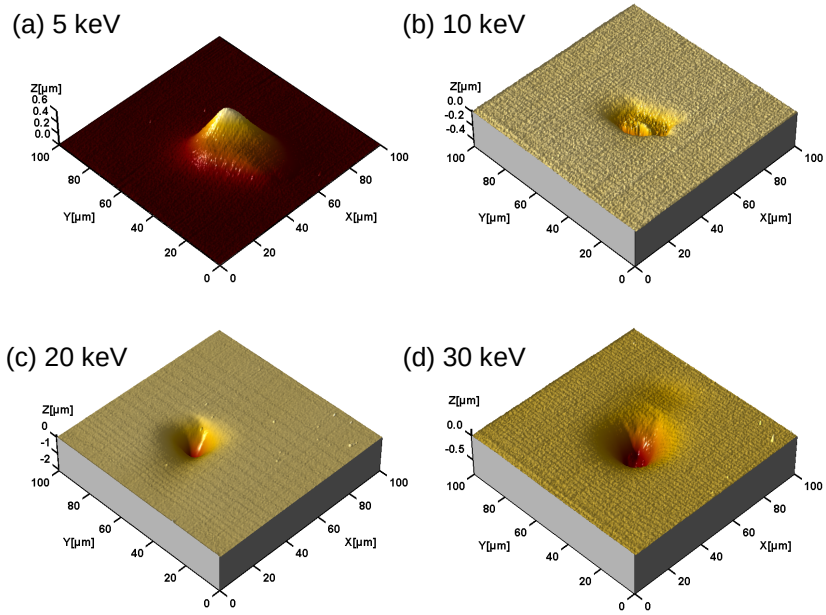

Figure 7.1 AFM images of silicon wafers, after bombardment by (a) C_{60}^{+} at 5 keV, (b) C_{60}^{+} at 10 keV, (c) C_{60}^{2+} at 20 keV, and (d) C_{60}^{3+} at 30 keV.

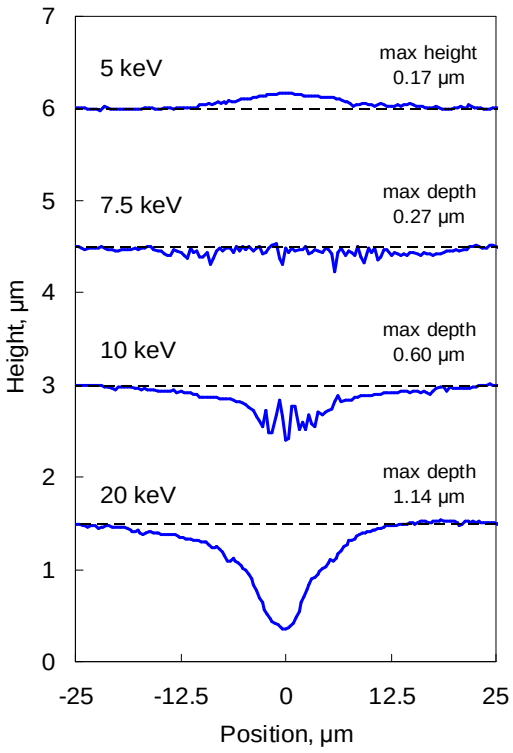

Figure 7.2 AFM line profiles of gold, after bombardment by C_{60}^{n+} at various bombardment energies, displayed here with an offset. The original surfaces are indicated by the dotted lines. This shows carbon deposition at 5 keV, the balance between sputtering and deposition at 7.5 keV, sputtering beginning to dominate at 10 keV and sputter removal dominating at 20 keV.

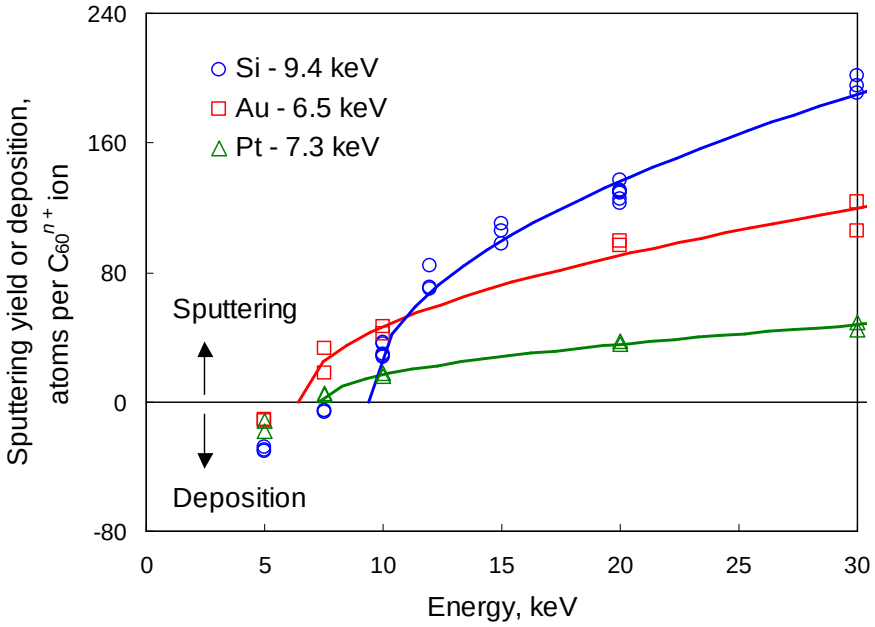

Figure 7.3 Measured sputtering yields of C_{60}^{n+} on silicon, gold and platinum at various energies. Where the sputtering yield is positive, the data are fitted to an empirical model $Y = a\,(E - b)^{0.5}$, which gives the threshold energy for net sputtering for each material (shown in the legend). At low energies, net carbon deposition occurs for all materials. This is plotted here by the number of carbon atoms deposited per C_{60}^{n+} ion.

As previously reported by other researchers,[22,23] carbon deposition occurs at low energy, resulting in the formation of hills, rather than craters, on the surface of the bombarded samples (for example on Figure 7.1a). The number of carbon atoms deposited per C_{60}^{n+} ion is calculated and plotted with a negative value in Figure 7.3. Conflicting theories exist on the identity of the deposited material during bombardment of silicon by C_{60}, with evidence suggesting it may be amorphous carbon[22] or silicon carbide.[23,24] The data here shows that carbon deposition is a general phenomenon for many materials, including gold and platinum, and is not specific to silicon which forms a carbide.

Figure 7.3 shows that the transition between net sputtering and deposition occurs between 5 – 10 keV for the materials studied. For data where the sputtering yield is positive, they are fitted to an empirical model $Y = a\,(E - b)^{0.5}$, where Y is the sputtering yield, E is the primary ion energy, and a and b are fitting parameters. The threshold energy for net sputtering is given by the value of b, and is 9.4 keV, 6.5 keV and 7.3 keV for silicon, gold and platinum,

respectively. It is important to note that this is different from the conventional threshold energy for the sputtering of bulk materials in the absence of carbon deposition. Near the threshold energy for net sputtering, the situation is complex. Here the surface no longer consists of pure material. Net deposition occurs when the total volume of material sputtered (both the sample material and any carbon deposited) becomes lower than the total volume of carbon deposited. Since gold has a higher sputtering yield than platinum, it has a lower threshold energy for net sputtering, as shown in Figure 7.3. However, silicon is observed to have the highest threshold energy despite its high yields. It has been suggested previously[23] that the strength of the Si–C bond may enhance the retention of carbon atoms in silicon, thereby increasing its threshold energy. However, it is found that the result may also be attributed to the lower nuclear stopping power of silicon compared to gold or platinum, which reduces the fraction of incoming energy deposited near the surface. This causes poorer sputtering of the deposited carbon on silicon in the case of marginal deposition near the threshold energy, and thereby increasing the energy required for net sputtering.

At higher energies where sputtering dominates, the sputtering yields shown in Figure 7.3 are far higher than the values predicted by a linear cascade model. Linear cascade assumes that each carbon atom in the primary ion causes an independent collisional cascade, and sputtering yield using C_{60} at an impact energy of E is equal to 60 times the sputtering yield using C at an impact energy of E/60. The sputtering yield assuming linear cascade theory can be estimated using SRIM (SRIM 2006, http://www.srim.org). SRIM calculates a sputtering yield of 80 atoms/ion for the C_{60} bombardment of silicon at 30 keV, which is only 40% of the actual value measured experimentally. Thus, the data in Figure 7.3 clearly displays the non-linear yield enhancements expected for cluster primary ions. It is shown elsewhere[25] that the data can be well described by Sigmund and Claussen's thermal spike model,[12-14] especially at high energies, where we are concerned mainly with the sputtering of pure materials.

7.3.2 Topography formation at low energies

AFM images and line profiles of the sputter craters, such as those shown in Figure 7.1 and Figure 7.2, reveal that the formation of surface topography is critical around the transition region between net sputtering and net deposition. At these energies, topography may develop due to the differences in sputter volumes between areas with exposed substrate material and areas where carbon has been deposited. This is suppressed at higher energies due to the increase in sputter yields which lead to more efficient removal of material.

To study this further, high-resolution AFM images over areas of 10 μm × 10 μm are acquired at the bottom of sputter craters on gold. These are shown in Figure 7.4a and 7.4b for ion bombardment energies of 7.5 keV and 10 keV, respectively. Figure 7.4a agrees with the 'grain' structure observed on sputtered silicon by Gillen *et al*,[22] although much greater heights of ~ 0.1 μm are observed here. Figure 7.4b shows the topographic structures in 10 keV craters, which are bigger and more widely dispersed than those in 7.5 keV craters. There is a clear relationship between the size of these structures and the sputter depth, which is plotted in Figure 7.4c. Since the sputter depth is directly related to the primary ion dose received locally, our results agree with Gillen's observation that topographic features gradually grow in size during the sputtering process, and this growth is demonstrated to be linear with primary ion dose up to a sputter depth of 0.6 μm. In both craters, the formation of topographic features is enhanced along scratches and defects on the gold surface. This causes the apparent orientation of topographic features along the diagonal direction in Figure 7.4a, due to numerous parallel micro-scratches on the polished gold surface, which are observed in scanning electron microscopy (SEM) images of the crater shown in Figure 7.4d. It is worth noting that the mechanism of topography formation here is different from that usually encountered in silicon sputtering[26,27] and also from the sputtering of bulk organic materials, where sample chemistry such as ion beam damage, relaxation and mobility of the target material also play a significant role.[18,20,28]

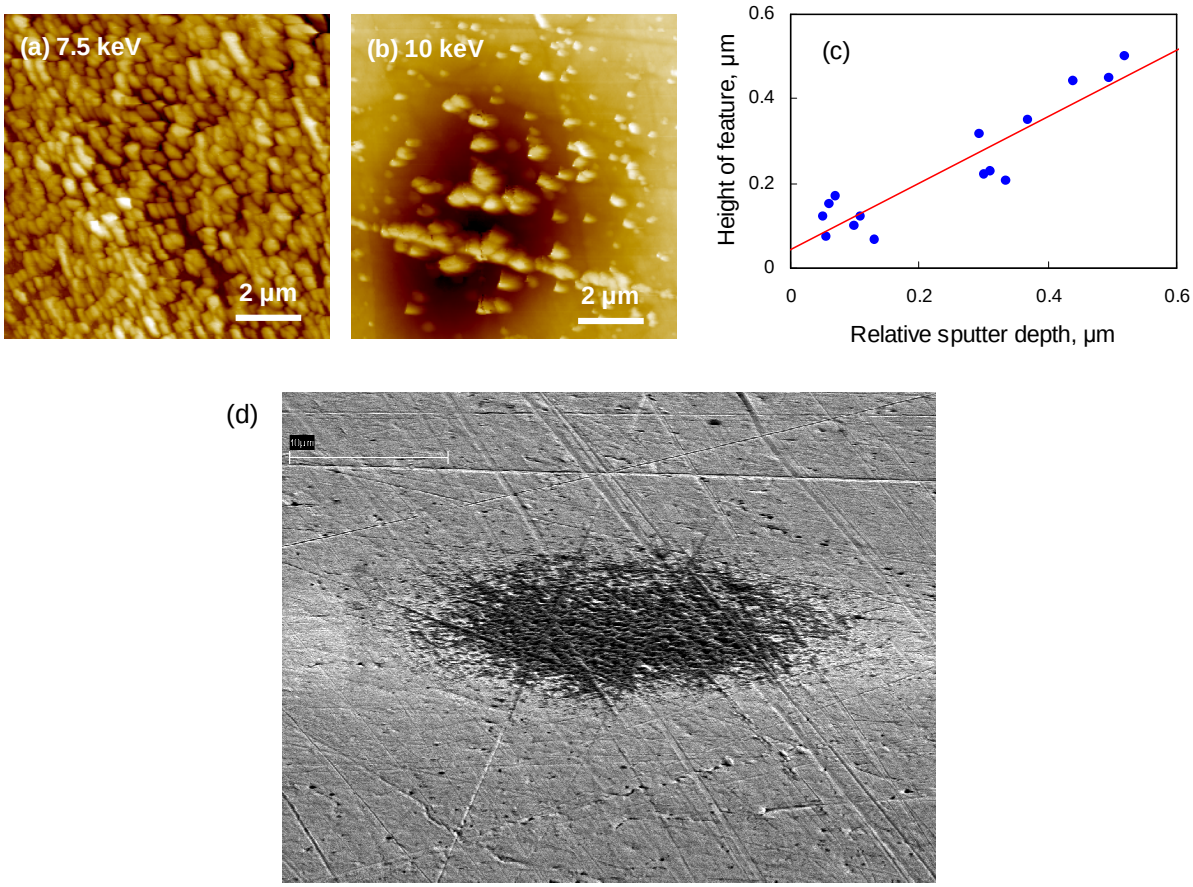

Figure 7.4 AFM image of gold after bombardment by C_{60}^{+} at (a) 7.5 keV (b) 10 keV. Image dimensions are 10 μm × 10 μm. C_{60}^{+} ions are incident from the right hand side. (c) Peak-to-peak heights of topographic features as a function of the sputter depths in the 10 keV gold crater, relative to the top right corner of the image. (d) SEM image of the 7.5 keV gold crater, acquired at a 70° tilt angle. The field of view is approximately 40 μm × 60 μm. This shows the orientation of topographic features along micro-scratches on the polished gold surface.

7.3.3 SIMS analysis of crater bottoms

In order to study the extent of carbon deposition and implantation at primary ion energies above the threshold for net sputtering, SIMS analysis is carried out on fresh craters sputtered on silicon at 12 keV, which show a smooth profile using AFM. Spectra and images acquired using Bi^{+} primary ions show significant enhancements of carbon clusters C_n^{-} as well as the various silicon-carbon groups $Si_nC_m^{-}$ after sputtering. This is shown in Figure 7.5. This shows the importance of deposition and implantation at an interface layer formed during sputtering.

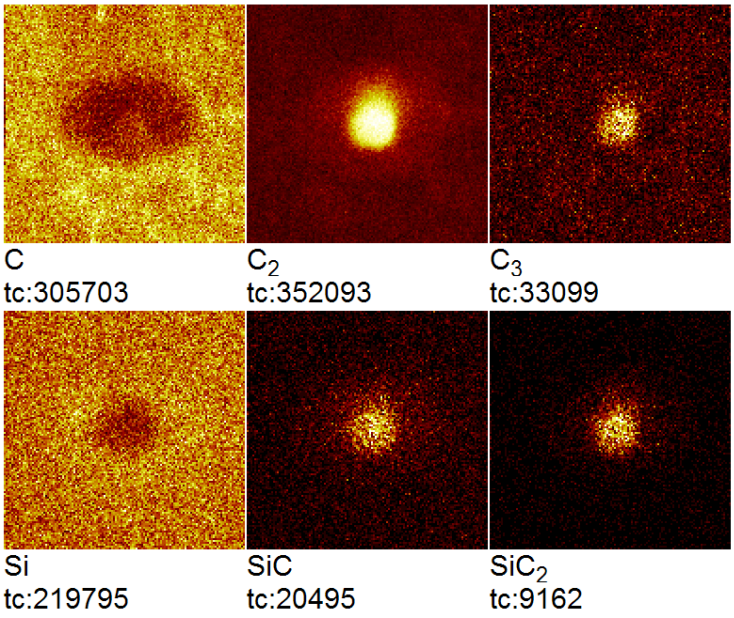

Figure 7.5 SIMS negative ion image of crater formed after 12 keV C_{60}^{2+} bombardment on silicon, showing significant intensities of C_n^- as well as $Si_nC_m^-$.

To study the composition of this mixed layer, depth profiling of the crater bottom is performed using a Bi^+ primary ion beam at 10 keV for both sputtering and analysis. The results are shown in Figure 7.6a for positive ions, and the depth scale is calibrated assuming the sputtering yield of Bi^+ on silicon. The data is fitted to a sum of two exponential functions to guide the eye and define the point of maximum intensity for each ion. This shows the intensity of C^+ secondary ions reducing with depth, while $Si_nC_m^+$ secondary ions reach a maximum at depths depending on fraction of carbon atoms in the ions, as shown in Figure 7.6b. This agrees with a gradual, mixed layer on the surface of sputtered craters such that the amount of implanted carbon reduces with depth. The implantation depth can be estimated by SRIM, assuming that the projected range of carbon in silicon from a C_{60} molecule at bombardment energy of 12 keV is the same as the range of a single carbon atom at $1/60^{th}$ of the energy (200eV). This gives an implantation depth of 1.7 nm, in agreement with the experimental results. From Figure 7.6b, the maximum thickness of the interface layer is found to be approximately 5 nm.

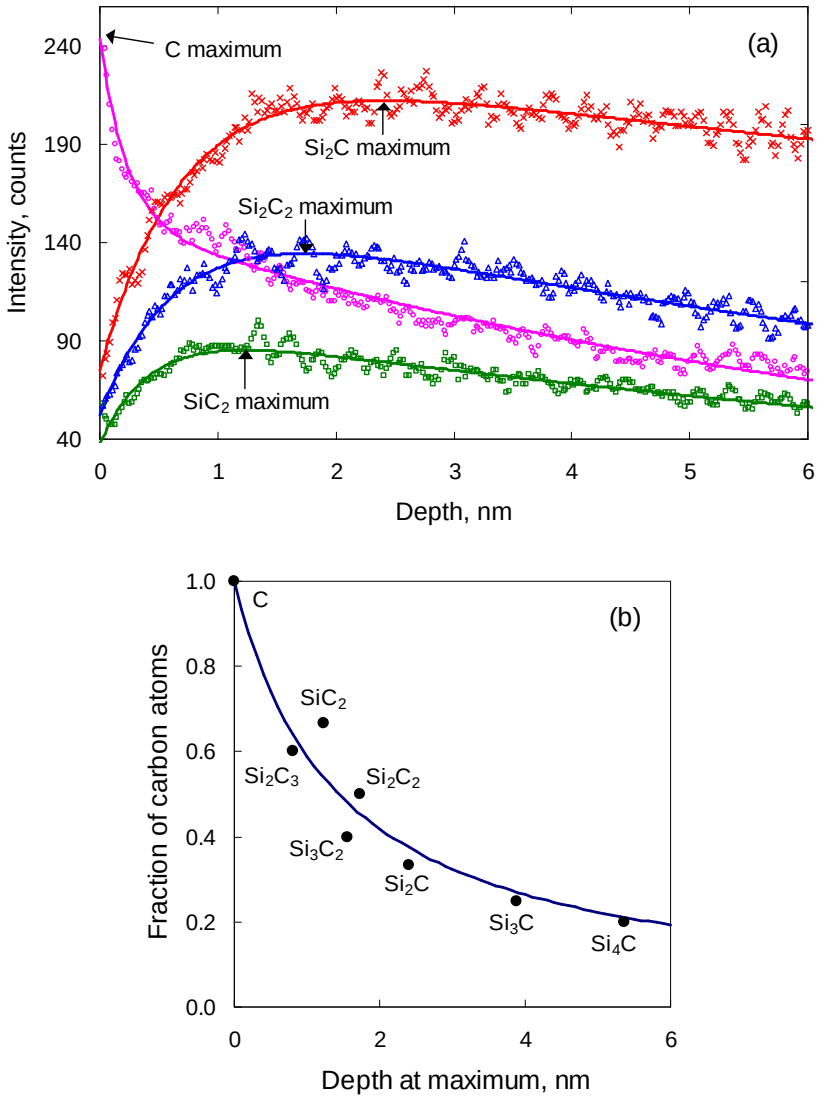

Figure 7.6 (a) SIMS positive ion depth profile of crater formed after 12 keV C_{60}^{2+} bombardment on silicon, showing the intensities of four secondary ions, C^+, SiC_2^+, Si_2C^+ and $Si_2C_2^+$. The depth scale is calibrated assuming the sputtering yield of Bi^+ on silicon. Solid lines show the fit to a sum of two exponential functions to guide the eye. (b) The fraction of carbon atoms in the secondary ions against the depth at which their maximum intensity occurs in (a), using the fitted curves.

7.4 Conclusions

A short study was conducted of the sputtering of silicon, gold and platinum samples with C_{60}^{n+}, over a range of energies from 5 to 30 keV. The high sputtering yields measured require

the non-linear enhancement of, for instance, Sigmund and Claussen's thermal spike model. At low energies carbon deposition occurs for all three materials, independent of carbide formation and target chemistry. The development of sputter-induced topography is observed to be fluence dependent, and is especially critical at the transition region between sputtering and deposition. This is suppressed at higher energies due to more efficient removal of material, suggesting a direct link between sputtering yield, carbon deposition and topography development. Above the energy required for net sputtering, deposition and implantation of carbon is important in an interface layer on the bottom of sputtered craters, covering a depth of ~ 5 nm. Finally, all the results shown above for the sputtering of inorganic materials by a C_{60}^{n+} cluster ion beam can be explained in terms of physical, rather than chemical, effects. In the development of a coherent metrology framework for the cluster sputtering of organic materials, it will be increasingly important to understand and distinguish between universal physical features associated with cluster sputtering and effects due to individual sample chemistry and sputtering conditions.

References

1 R. Pinna, F. Jamme, F. J. M. Rutten, E. F. Smith, M. R. Willis, D. Briggs, and M. R. S. McCoustra, Applied Surface Science **252,** 6672 (2006).

2 E. A. Jones, N. P. Lockyer, and J. C. Vickerman, International Journal of Mass Spectrometry **260,** 146 (2007).

3 C. A. Prestidge, T. J. Barnes, and W. Skinner, Journal of pharmacy and pharmacology **59,** 251 (2007).

4 C. M. Mahoney, J. X. Yu, A. Fahey, and J. A. Gardella, Applied Surface Science **252,** 6609 (2006).

5 R. Michel and D. G. Castner, Surface and Interface Analysis **38,** 1386 (2006).

6 G. Tsourapas, F. J. M. Rutten, D. Briggs, M. C. Davies, and K. M. Shakesheff, Applied Surface Science **252,** 6693 (2006).

7 J. S. Fletcher, N. P. Lockyer, and J. C. Vickerman, Surface and Interface Analysis **38,** 1393 (2006).

8 B. Johansson, Surface and Interface Analysis **38,** 1401 (2006).

9 J. Kozole, C. Szakal, M. Kurczy, and N. Winograd, Applied Surface Science **252,** 6789 (2006).

10 P. Sigmund, Physical Review **184,** 383 (1969).

11 M. P. Seah, C. A. Clifford, F. M. Green, and I. S. Gilmore, Surface and Interface Analysis **37,** 444 (2005).

12 P. Sigmund and C. Claussen, Journal of Applied Physics **52,** 990 (1981).

13 H. H. Andersen, A. Johansen, and V. S. Touboltsev, Nuclear Instruments and Methods in Physics Research Section B: Beam Interactions with Materials and Atoms **164,** 727 (2000).

14 M. P. Seah, Surface and Interface Analysis **39,** 634 (2007).

15 S. X. Sun, C. Szakal, N. Winograd, and A. Wucher, Journal of the American Society for Mass Spectrometry **16,** 1677 (2005).

16 A. V. Samartsev, A. Duvenbeck, and A. Wucher, Physical Review B **72,** 115417 (2005).

17 Z. Postawa, B. Czerwinski, N. Winograd, and B. J. Garrison, The Journal of Physical Chemistry B **109,** 11973 (2005).

18 C. M. Mahoney, A. J. Fahey, G. Gillen, C. Xu, and J. D. Batteas, Analytical Chemistry **79,** 837 (2007).

19 A. G. Shard, P. J. Brewer, F. M. Green, and I. S. Gilmore, Surface and Interface Analysis **39,** 294 (2007).

20 A. G. Shard, F. M. Green, P. J. Brewer, M. P. Seah, and I. S. Gilmore, Journal of Physical Chemistry B **112,** 2596 (2008).

21 F. M. Green, A. G. Shard, I. S. Gilmore, and M. P. Seah, Analytical Chemistry **81,** 75 (2009).

22 G. Gillen, J. Batteas, C. A. Michaels, P. Chi, J. Small, E. Windsor, A. Fahey, J. Verkouteren, and K. J. Kim, Applied Surface Science **252,** 6521 (2006).

23 K. D. Krantzman, D. B. Kingsbury, and B. J. Garrison, Applied Surface Science **252,** 6463 (2006).

24 K. D. Krantzman, D. B. Kingsbury, and B. J. Garrison, Nuclear Instruments & Methods in Physics Research Section B-Beam Interactions with Materials and Atoms **255,** 238 (2007).

25 J. L. S. Lee, M. P. Seah, and I. S. Gilmore, Applied Surface Science **255,** 934 (2008).

26 B. Fares, B. Gautier, N. Baboux, G. Prudon, P. Holliger, and J. C. Dupuy, Applied Surface Science **231,** 678 (2004).

27 Y. Kataoka, K. Yamazaki, M. Shigeno, Y. Tada, and K. Wittmaack, Applied Surface Science **203,** 43 (2003).

28 J. Cheng, A. Wucher, and N. Winograd, Journal of Physical Chemistry B **110,** 8329 (2006).

Chapter 8 – Organic depth profiling of a nanostructured delta layer reference material using large argon cluster ions

8.1 Introduction

The use of cluster primary ions in time-of-flight secondary ion mass spectrometry (SIMS) has provided a step-change in the capability of SIMS for high-resolution biomolecular imaging[1] and the potential to generate 3D molecular depth profiles through organic materials such as drug delivery systems[2] and cells.[3,4] It is clear that for organic depth profiling to be a routine analytical tool for SIMS and XPS, the primary ions must be able to sputter through a range of sample chemistries without inducing severe surface topography or chemical damage. This is especially important if organic depth profiling is to be a useful tool for the chemical characterisation of many emerging technologies reliant on thin molecular or polymeric multilayers, including drug delivery systems, and organic electronics such as organic photovoltaics and organic light emitting diodes (OLEDs). Improved depth resolution and reduced damage would enable greater definition of layers and interfaces as well as offer access to deeper layers.

Most studies for cluster ion beams use commercially available ion sources, for example Au_3^+, Bi_3^+, SF_5^+ and C_{60}^{n+}. As a result of the wealth of studies devoted to these ion beams, their strength and weaknesses are now becoming clearer. For organic depth profiling, SF_5^+ and C_{60}^{n+} are favored over metal clusters such as Au_3^+ and Bi_3^+ due to reduced damage cross sections and damage accumulation.[5-8] Studies have shown that C_{60}^{n+} causes lower sub-surface damage compared to SF_5^+,[8] and is extremely successful for the depth profiling of some organic materials such as polylactide (PLA),[9] poly(methyl methacrylate) (PMMA)[10] and trehalose.[11] Consequently, C_{60}^{n+} is generally the ion beam of choice in organic depth profiling. However, several important issues remain with C_{60}^{n+} sputtering. This includes significant accumulation of damage for some materials, which results in a failure to obtain

steady-state secondary ion intensities and sputtering yields during depth profiling.[12,13] The depth resolution is currently limited to approximately 10 nm at best,[14] although significantly poorer resolution (35 nm) has been obtained after sputtering to depths of 350 nm.[12] At lower energies where the depth resolution improves, C_{60}^{n+} may cause carbon deposition[15,16] and abrupt loss of secondary ion signal.[12] Much effort has recently been devoted to alleviate these issues, for example, via sample cooling[14,17,18] or the use of a grazing incidence angle.[19] On the other hand, there has been a recent increase in studies devoted to novel cluster ion sources, including $C_{24}H_{12}^{+}$ and C_{80}^{+},[20] $Ir_4(CO)_7^{+}$,[21] Au_{400}^{4+},[22] and Ar_{1500}^{+}.[23] There is a general consensus in the community that the optimal choice of primary ion for organic depth profiling is complex and dependent on the sample under study.[7,22-25,26] It is likely that different primary ion beams would be optimal for different applications. Nevertheless, new cluster ion sources offer the potential for novel sputtering and ionisation mechanisms, which may expand the range of samples that can be profiled as well as improving the depth resolution achievable.

Preliminary studies using gas cluster ion beams such as Ar_{1500}^{+} have shown promising results for SIMS. Ar cluster ions have been demonstrated to successfully yield secondary ion spectra of a peptide, GlyGlyGly, and an amino acid, arginine, with little molecular fragmentation.[27] They have been shown to sputter through leucine at a constant rate, up to a sputtered depth of 1.5 μm, without observable chemical changes in the subsequent spectra.[28] Successful organic depth profiles have been demonstrated on polycarbonate,[29] polystyrene[29] and Alq_3,[30] all of which have been shown to be very difficult with C_{60}^{n+} due to damage accumulation.[9,13] Since each Ar cluster ion consists of hundreds or thousands of atoms, the energy per constituent atom is of the order of 10 eV, which is typically below the threshold energy for sputtering by atomic ions.[31] Molecular dynamics (MD) simulations have shown that different sputtering and desorption mechanisms may be possible,[32-35] which may lead to the large sputtering yields and reduced molecular fragmentation observed experimentally. Although the technology is still in its infancy, studies so far have shown excellent potential for organic depth profiling. It is therefore important that the fundamental aspects of Ar cluster sputtering are evaluated

rapidly, and the basic metrology developed, in order to facilitate the development of the technology and increase analytical capabilities.

In this study, the depth profiling of an organic delta layer sample using an Ar cluster ion beam, with mean cluster sizes of 500, 700 and 1000 atoms, is explored. The sample consists of ultra-thin "delta" layers of Irganox 3114 (~ 2.4 nm) embedded between thick layers of Irganox 1010 (~ 46 nm for the first two layers and ~ 93 nm for the subsequent three layers). The sample is very similar to those used in a previous study[12] and employed in a VAMAS interlaboratory study on organic depth profiling.[17,36] Both studies have shown that the delta layer reference material is an excellent model system, exhibiting very consistent behavior regardless of the production batch or construction, i.e. the number and spacing of the layers. The thicknesses and positions of the layers are well characterised, allowing important parameters such as the sputtering yield, the constancy of the sputtering yield and the achievable depth resolution to be determined consistently as a function of sputtered depth, beam energy and Ar cluster size. This provides valuable insights which can help elucidate the sputtering mechanisms using Ar gas cluster primary ion beams. Direct comparisons will be made with previous data from the sputtering of similar layers using C_{60}^{n+},[12] obtained at 45° incidence angle for 5 – 30 keV impact energy at room temperature. This is the most common analytical set-up, although further improvements may be possible by optimising the angle of incidence, energy or sample temperature.[14,19]

This study is the result of collaboration with Kyoto University who pioneered the development of Ar cluster ion guns for SIMS. The study is conducted on a prototype and unique instrument. Although there is much need to improve its performance for general analytical purposes, the present work using well-characterised reference materials indicates the benefits of the approach using Ar cluster ions. It also highlights important aspects for future development, such as the need to improve the mass and spatial resolutions obtainable, which could be achieved by improving the mass filtration of the ion beam or, more readily, by the use of a dual beam configuration for depth profiling.

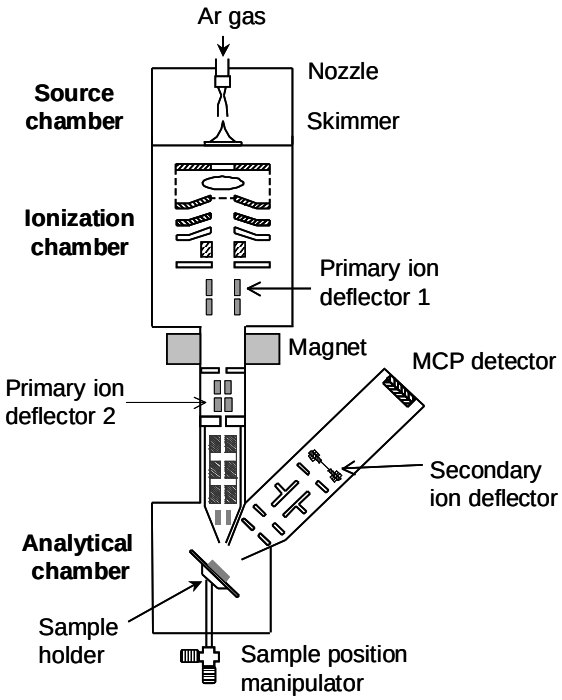

Figure 8.1 A schematic diagram of the argon cluster ion SIMS instrument at Kyoto University.

8.2 Experimental

8.2.1 Instrumentation

A review of gas cluster ion beam theory, instrumentation and application can be found in References 37-39. Details of the Ar cluster SIMS instrument can be found in Reference 40. A schematic diagram of the instrument is shown in Figure 8.1. The instrument is equipped with an Ar gas cluster ion gun and a linear time-of-flight (TOF) mass analyser, mounted at 45° and perpendicular to the sample surface, respectively. Both the ion gun and the mass analyser were designed and constructed in Kyoto University by Prof Jiro Matsuo and his research group. Neutral Ar clusters are formed by the supersonic expansion of the Ar source gas, injected into a vacuum at high pressure (5 atmospheres) through a small nozzle. The neutral beam is ionised by electron impact and accelerated by up to 20 kV. Magnets situated between the ionisation and analytical chambers remove Ar monomer ions and small clusters. This gives a broad cluster size distribution, which can be tuned to mean cluster sizes of 500 – 1000

Ar atoms by adjusting the ionisation voltage.[41] The full width at half maximum of the cluster size distribution is typically of the order of the mean cluster size.[41,42] A DC beam current of 8 nA can be readily obtained with a spot size < 0.5 mm. The beam current is found to vary by < 3% during the course of a typical depth profiling experiment, which takes on average 100 minutes.

In this study, data acquisition using the prototype instrument was carried out by Dr Satoshi Ninomiya (Kyoto University). All data analysis was carried out by myself. Depth profiles were acquired at room temperature by alternating between 1 s sputtering (DC) and 1.5 s analysis (pulsed) cycles, using automated software that controls the ion beam raster and data acquisition. The mean cluster size (Ar_{500}^+ to Ar_{1000}^+) and impact energies (8 to 17 keV) are varied and one profile is obtained for each ion beam setting. For the sputtering cycles, the DC beam is rastered to give an average dimension of 4.7 mm × 3.6 mm for the sputtered craters, depending on the ion energy and the raster voltages. The estimated standard uncertainty of the ion dose is 10%. This is dominated by systematic uncertainties in the measured current (due to the lack of a suitable Faraday cup on the sample holder)[43] and the sputtered crater size, with an estimated random uncertainty contribution of < 5%. For the acquisition of secondary ion spectra during the analysis cycle, the primary ion beam is pulsed at 1 kHz using an ion deflector with a time width of 5 μs. Initial mass filtering is carried out using a second primary ion deflector, operated at the same time width and located further down the ion beam column where the ion pulse has broadened due to the spread in cluster sizes and hence velocity. This considerably narrows the range of Ar cluster sizes incident on the sample during the analysis cycle.[44] After the impact, secondary ions are extracted into the TOF analyser by the use of a sample bias (+2 kV for positive ions and –2 kV for negative ions), where they are further chopped using a secondary ion deflector[40] with a pulse width of 200 ns. Since the primary ions have a spread of arrival times on the sample due to the cluster size distribution, the time delay between the first primary ion deflector and the secondary ion deflector is used to accept only secondary ions that are generated by Ar_{700}^+ primary ions (with an approximate distribution of ± 50 atoms),[29] regardless of the mean cluster size of the DC sputtering beam.

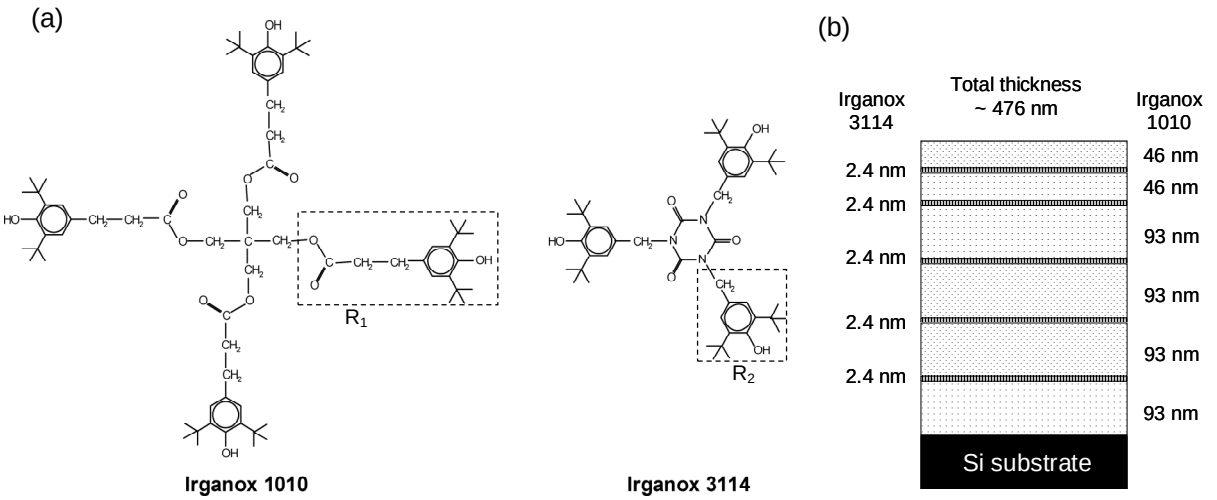

Figure 8.2 (a) The chemical structure of Irganox 1010 and Irganox 3114. The major fragment units, R_1 for Irganox 1010 and R_2 for Irganox 3114, are shown within the dashed boxes. (b) The multilayer structure of the Irganox organic delta layer sample.

This is necessary for obtaining good quality secondary ion spectra, and also improves the comparability between depth profiles. Finally, the secondary ions are measured using a microchannel plate (MCP) detector at the end of the linear TOF analyser. During analysis, the beam raster is restricted to the centre of the sputtered crater and has a width equal to a third of the crater size to avoid the effects of uneven dose at the crater edges. The ion dose delivered during the analysis cycle is three orders of magnitude lower than the sputtering cycle, and can be considered negligible. No charge compensation is applied during the sputtering or analysis cycles, and all depth profiles reach the silicon substrate successfully.

8.2.2 Organic delta layer reference material

Full details on the preparation of the organic delta layer sample can be found in Reference 12. The sample preparation and initial characterisation before sputtering were carried out by Radleigh Foster and Dr Alex Shard (National Physical Laboratory). Irganox 1010 and Irganox 3114 (CIBA, Macclesfield, UK), placed in separate crucibles, are alternately evaporated onto initially clean silicon wafers measuring 1 cm × 1 cm using an Edwards

AUTO306 vacuum coater (Edwards Ltd., Crawley, UK). The chemical structure of the two Irganox materials and the multilayer structure of the sample are shown in Figure 8.2. Each sample consists of five ultra thin "delta" layers of Irganox 3114 (~ 2.4 nm), separated by thick layers of Irganox 1010 (~ 46 nm for the first two layers and ~ 93 nm for the subsequent three layers). The thickness of each layer is measured using an *in situ* quartz crystal microbalance (QCM) combined with an *ex situ* spectroscopic ellipsometer (Woollam M2000, NE, USA), assuming the QCM mass response to be linear over the range of thicknesses deposited and identical for the two different materials. Five samples are prepared in a single batch, and one depth profile is obtained in the middle of each sample with the exception of one sample where two profiles are obtained in adjacent areas. Typically thickness variations of less than 5% can be obtained across the width of the wafer, corresponding to ~ 2% over the analysis area.

8.2.3 AFM measurements

The development of sputter induced surface roughness is measured using thick evaporated pure Irganox 1010 layers (~ 475 nm), prepared by Tara Salter (National Physical Laboratory). The samples are sputtered to different depths using a range of Ar cluster sizes and energies. AFM images close to the centre of the sputtered craters are acquired by myself using a SPM-9500 J2 instrument (Shimadzu, Japan) in a.c. "tapping" mode, over a scan area of 10 μm × 10 μm. The images are used to calculate the root mean square roughness (R_q) values. The non-irradiated surface of Irganox 1010 is invariably found to be extremely smooth, with R_q ~ 0.3 nm.

8.3 Results and discussion

Figure 8.3 shows the negative secondary ion spectra obtained from pure Irganox 1010 and Irganox 3114 samples using Ar_{700}^+ primary ions at 12 keV. Strong nitrogen-containing fragment ions can be observed in the negative ion spectra for Irganox 3114, for example CN^- and CNO^-, as well as higher mass ions characteristic of the original structures of Irganox 1010 and Irganox 3114, for example $C_{17}H_{25}O_3^-$ for Irganox 1010 R_1^- and

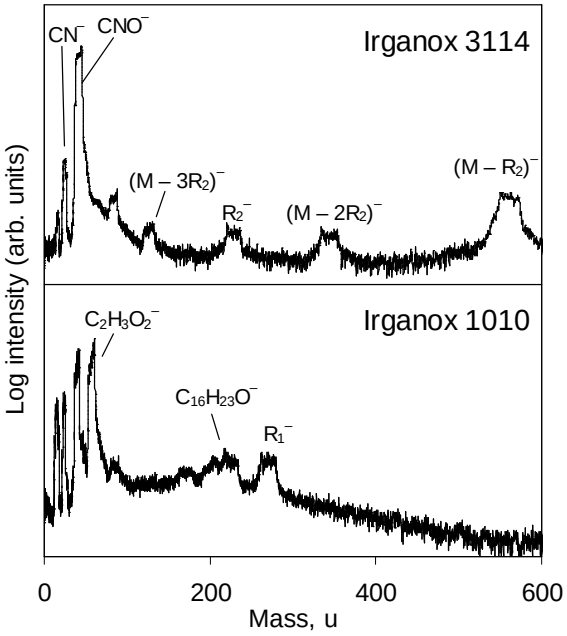

Figure 8.3 Negative ion spectra of pure Irganox 3114 and Irganox 1010 layers obtained using Ar_{700}^{+} at 12 keV. Secondary ions characteristic of each of the molecules are labeled.

$C_{33}H_{46}N_3O_5^-$ for Irganox 3114 $(M - R_2)^-$. The positive secondary ion spectra are also obtained, but they show no characteristic peaks that can be used to discriminate sufficiently between Irganox 3114 and Irganox 1010, due to their similar chemical structures. In this prototype cluster SIMS instrument several issues exist for monitoring negative ion intensities, mainly owing to the simple mass analyser system used at the time of this study. Firstly, the sensitivity is very low for high mass characteristic ions, due to the low impact energy of the secondary ions onto the detector.[45] This limits the analysis here to smaller fragment ions. Secondly, the mass resolution of the linear TOF instrument is very poor in the negative ion mode, and low mass fragments cannot be resolved from other peaks within ± 5 u. Fortunately, the two Irganox materials can be clearly distinguished using the broad peaks centered around 45 u and 60 u. By comparison with the high mass resolution spectra obtained using Bi_3^+ primary ions in an ION-TOF TOF-SIMS IV instrument, these peaks are identified to be dominated by the intense characteristic fragments CNO^- (41.9980 u) for Irganox 3114 and $C_2H_3O_2^-$ (59.0133 u) for Irganox 1010. From TOF-SIMS IV depth profiling studies of similar delta layer samples, the major intensity change for Irganox 3114 is in the CNO^- peak, which

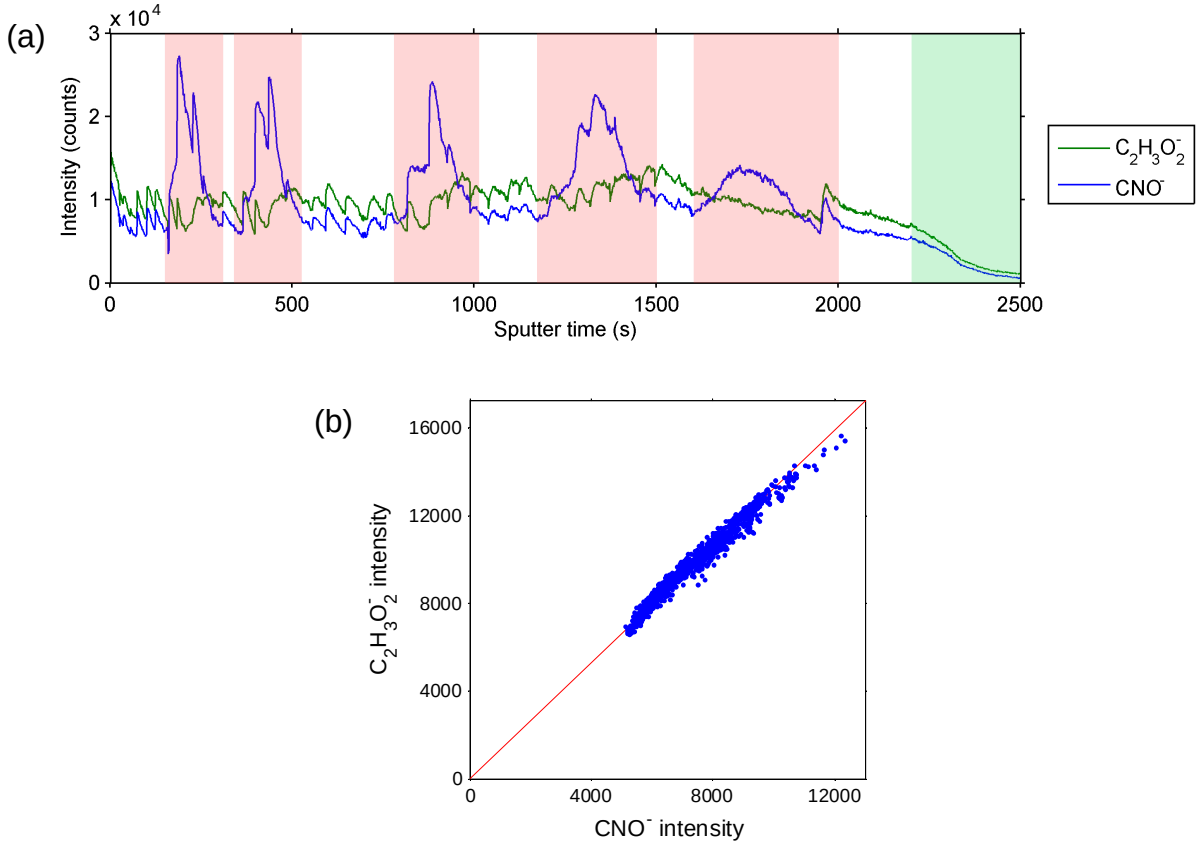

Figure 8.4 (a) Raw intensities measured during the depth profiling of the Irganox delta layer reference material using Ar_{500}^+ at 12 keV. This shows CNO^- (characteristic of Irganox 3114) and $C_2H_3O_2^-$ (characteristic of Irganox 1010), plotted against the sputter time. The red shaded regions indicate the appearance of Irganox 3114 delta layers and the green shaded region indicate the substrate. (b) A plot of $C_2H_3O_2^-$ against CNO^- intensities for the white regions in (a) which consists of pure Irganox 1010. The red line shows the proportionality between the two peaks despite the fluctuations in absolute intensities. The peak ratio $CNO^- / C_2H_3O_2^-$ is therefore well behaved and is constant for Irganox 1010 with a scatter standard deviation of 3%.

tracks the intensity of $(M-R_2)^-$ but is 25 times more intense. Within the mass ranges of the broad peaks identified on the Ar_{700}^+ spectrum, contributions from non-characteristic fragments and contamination are weak, and these peaks therefore provide sufficient selectivity for monitoring the relative amount of Irganox 1010 and Irganox 3114 on the surface, despite the limited mass resolution. Finally, some fluctuations are observed in the secondary ion intensities, which may be caused by intermittent instabilities of the detector or by some charging effect. Figure 8.4a shows the effect of this on an example depth profile

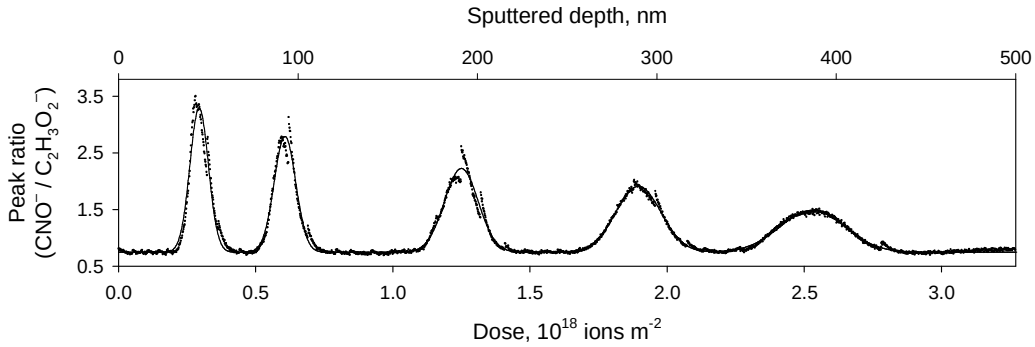

Figure 8.5 Depth profiles of the Irganox delta layer sample, obtained using Ar_{500}^+ primary ions at 12 keV. Dots show the measured peak ratio ($CNO^- / C_2H_3O_2^-$) as a function of the primary ion dose and sputtered depth, and the solid line shows a fit using a sum of five Gaussian functions.

obtained on the delta layer sample. The fluctuation is observed to affect different peaks similarly (Figure 8.4b), and may be corrected by using the ratios of the two peaks ($CNO^- / C_2H_3O_2^-$) in the subsequent analysis. This reduces fluctuations of ~ 20% to a scatter standard deviation of ~ 3%. This approach is found to provide a good description for all depth profiles.

8.3.1 Depth profiles

In total, six depth profiles of the delta layer reference material were obtained using a range of Ar cluster sizes (Ar_{500}^+ to Ar_{1000}^+) and impact energies (8 keV to 17 keV). The depth profile obtained using Ar_{500}^+ primary ions at 12 keV is shown in Figure 8.5, and the raw intensities are given in Figure 8.4a for reference. The peak ratio ($CNO^- / C_2H_3O_2^-$), plotted as a function of Ar_{500}^+ ion dose, clearly shows the Irganox 3114 delta layers with the depth resolution degrading with increasing ion dose. For all energies and cluster sizes, successful depth profiles are obtained through the ~ 480 nm multilayer structure, showing the five delta layers distinctly followed by the rise of the SiO_3^- ion characteristic of the substrate surface. The results are a considerable improvement upon previous data from C_{60}^{n+} sputtering, where a minimum of 20 keV is needed to profile completely through the delta layer satisfactorily. This is due to the rapid, non-recoverable loss of secondary ion intensities at 5 keV after a

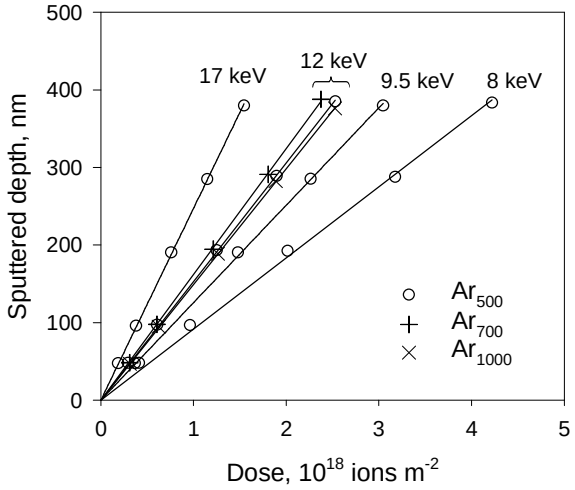

Figure 8.6 The sputtered depth as a function of the primary ion dose, for a range of Ar cluster sizes and energies (symbols). The solid lines show linear fits to the data, which are constrained to go through the origin.

sputtering depth of 250 nm, and the loss of useful depth resolution at 10 keV before the silicon interface is reached.[12] This necessitates the use of higher energies with C_{60}^{n+}, which degrades the intrinsic depth resolution.[14]

The use of the peak ratio in Figure 8.5 minimises, but cannot completely remove, the effect of intensity fluctuations, which can be observed for example during the third delta layer. The data are fitted to a sum of five Gaussian functions, which are shown as solid lines. This is a good description despite a small asymmetry observed in the delta layer responses, especially for the first delta layer. The integrals of the Gaussian functions are roughly constant for different delta layers, indicating that the peak ratio can be used as a reasonable estimate of the amount of Irganox 3114. Here, the centroids of the Gaussian functions are used to determine the ion dose required to reach each delta layer, whose depths have been determined independently using QCM and ellipsometry. The resulting sputtered depths plotted as a function of the primary ion dose for all depth profiles are shown in Figure 8.6. For clarity, the error bars associated with the ion dose on this figure are omitted, since the uncertainties are dominated by systematic contributions as discussed earlier. The systematic contributions have the effect of changing the dose scale a few percent but do not alter the appearance of the figure.

For all depth profiles, a constant sputtering yield is obtained, resulting in a sputtered depth that is linear with the primary ion dose throughout a depth of 390 nm. The points scatter randomly about the linear fits in Figure 8.6 with a standard deviation of 3.5 nm in the delta layer positions. The constant sputtering rate is important for the reliable depth profiling of thicker layers and for the ability to quantify or estimate the sputtered depths during the analysis of unknown samples. It also implies very low accumulated damage during depth profiling using Ar gas cluster ions since, as damage accumulates, the material changes and is likely to have a different sputtering yield. These results are in contrast with C_{60}^{n+} sputtering,[12] where the sputtering yield diminishes with ion dose, owing to chemical changes in the Irganox material caused by ion-induced damage. Ar cluster ions therefore present a major improvement compared to C_{60}^{n+}.

8.3.2 Sputtering yields

It is straightforward to obtain the sputtering yield volume, i.e. the volume of Irganox 1010 material removed per impacting Ar cluster ion, using the gradient of the linear fit in Figure 8.6, assuming the change in yield volume is negligible between the thin Irganox 3114 delta layer and the Irganox 1010 matrix. Figure 8.7 shows the yield volume as a function of ion energy, along with a linear fit. The estimated uncertainties of 10%, dominated by systematic uncertainties, are shown in the error bars. The data fall neatly along the linear fit, indicating that the random uncertainties are indeed small. The yield volume at this energy range is linear with the ion energy, and this behavior is very similar to the C_{60}^{n+} sputtering of Irganox,[9] PLA,[9] and trehalose,[11] as well as Ar_{2000}^{+} sputtering of leucine.[28] The yield volumes are higher than C_{60}^{n+} sputtering of Irganox 1010, for example 250 nm^3 of material is removed per impacting Ar cluster ion at 17 keV compared to 163 nm^3 of material per C_{60}^{2+} ion at 20 keV.[9,12] Interestingly, no clear dependence can be seen between the Ar cluster size and the sputtering yield at 12 keV. The total impact energy, rather than the energy per constituent atom, appears to be the dominating factor in the sputtering yield. This is very different to the sputtering of inorganic materials with large Ar clusters,[41,46-48] which shows a rapid reduction of the sputtering yield when the cluster size is increased for the same energy, as the energy

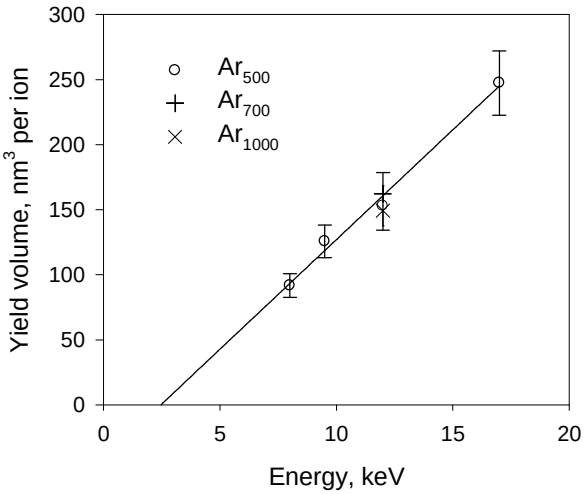

Figure 8.7 The sputtering yield volume of Irganox 1010 as a function of ion energy, with a linear fit. An estimated uncertainty of ± 10%, owing mainly to measurement of the primary ion current and crater size, is shown on the error bars.

per atom approaches the threshold of sputtering by cluster ion beams (around several eV per atom)[46].

The data may be explained by the range of energies used in this experiment (12 – 34 eV per atom), which is well above the energies of the inter- and intra-molecular bonds and therefore away from threshold effects. If all the energies are deposited near the surface and available for sputtering, and the yield per atom is roughly proportional to the energy per atom in this range, then we should expect the sputtering yield to be dependent on the total available energy rather than the cluster size. Delcorte *et al.* have observed similar behaviors above a threshold of 1 eV per nucleon in recent MD simulations of the bombardment of organic targets using large C_xH_y organic cluster projectiles.[32] For Ar cluster sputtering, the threshold may be significantly lower, since much lower energies are needed to break the primary projectile apart on impact. Finally, since the cluster size distributions associated with each mean cluster size may overlap, further experiments using cluster ion beams with improved size selection may provide valuable information.

8.3.3 Depth resolution

The depth resolution as a function of Ar cluster size, beam energy and sputtered depth can also be studied in detail using the depth profiles. If we assume that the Irganox 3114 delta layers are negligibly thin compared to the depth resolution response function, then the signal from the delta layer is a direct representation of the depth resolution function. The use of the peak ratio ($CNO^- / C_2H_3O_2^-$) for depth resolution requires some consideration. Since Irganox 1010 intensities drop slightly as the Irganox 3114 delta layers are reached,[12] the peak ratio could lead to an apparently improved depth resolution compared to using Irganox 3114 intensities only. To estimate the extent of this effect, here it is assumed that the SIMS intensities are directly proportional to the exposed surface area of each material during the depth profile, and the depth resolution function solely reflects the sputter-induced topography which causes different areas of the thin Irganox 3114 delta layer to be revealed at slightly different doses. Figure 2 in Reference 49 provides a nice visualisation of this effect. The maximum total exposed surface area of Irganox 3114, obtained during depth profiling of the first delta layer when the depth resolution is best, can be estimated to be < 20% of the total surface area. For a Gaussian response function, this may give rise to 6% improvement in the depth resolution obtained using peak ratios. This error is reduced for deeper delta layers, where the exposed surface area of Irganox 3114 is lower due to the poorer depth resolution. The peak ratio therefore provides a reasonably good estimate of the depth resolution achievable with Ar cluster sputtering in the present experiment.

Figure 8.8a shows the depth resolution as a function of sputtered depth for different Ar cluster sizes and energies, obtained from the Gaussian fits to the data. Since the depths of the delta layers are known *a priori*, the depth resolution is independent of the ion dose measurements and unaffected by the associated uncertainty. Here the depth resolution is expressed as the full width at half maximum (FWHM) of the measured response function. For a Gaussian response function, σ, the standard deviation of the response function, is equal to the FWHM divided by 2.35. Figure 8.8a also shows the depth resolution obtained using C_{60}^+ at 10 keV.[12] The values for C_{60}^{2+} at 20 keV (not shown) are typically 20% worse. For reference, the respective depth

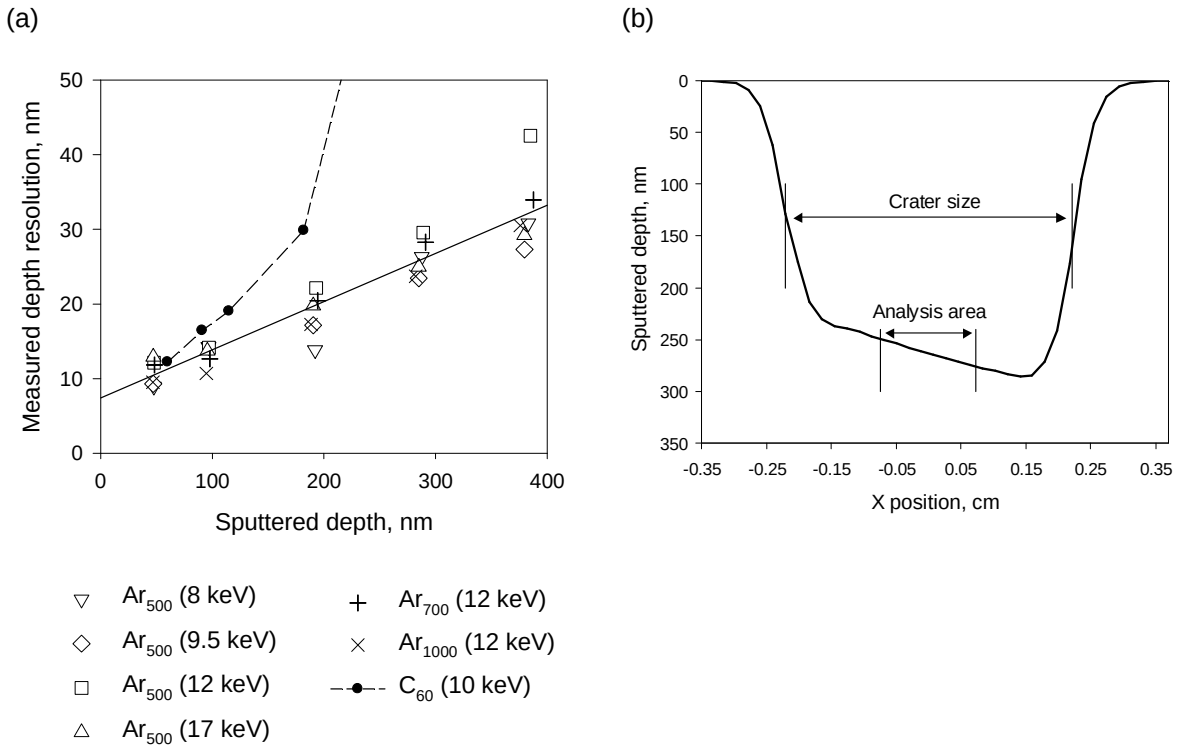

Figure 8.8 (a) The measured depth resolution (FWHM) as a function of sputtered depth, for a range of Ar cluster sizes and energies. The solid line shows a linear fit to the data. For comparison, the values for C_{60}^{+} sputtering at 10 keV are also plotted as solid circles.[12] (b) An example profile of the sputtered crater before the silicon substrate has been reached, measured using spectroscopic ellipsometry. This gives rise to ~ 10% difference in the sputtered depth over the analysis area, accounting largely for the measured depth resolution.

profiles obtained from Ar_{500}^{+} (at 12 keV) and C_{60}^{n+} (at 10 and 20 keV)[12] are plotted on the same scale in Figure 8.9. This shows that Ar cluster ions offer improved depth resolution compared to C_{60}^{n+} at the same impact energy and experimental conditions. Clear and distinct delta layers are observed throughout the depth profiles with Ar cluster ions, whereas the C_{60}^{n+} results show poorer depth resolution and the overlap of response functions between adjacent delta layers with spacings of 90 nm, after a sputtered depth of only 300 nm.

It can be seen from Figure 8.8a that very similar depth resolutions are currently obtained using different Ar cluster ions, which degrades with increased sputtered depth. The best depth resolution, obtained by extrapolation to zero sputtered depth, is estimated to be about 7 nm. A

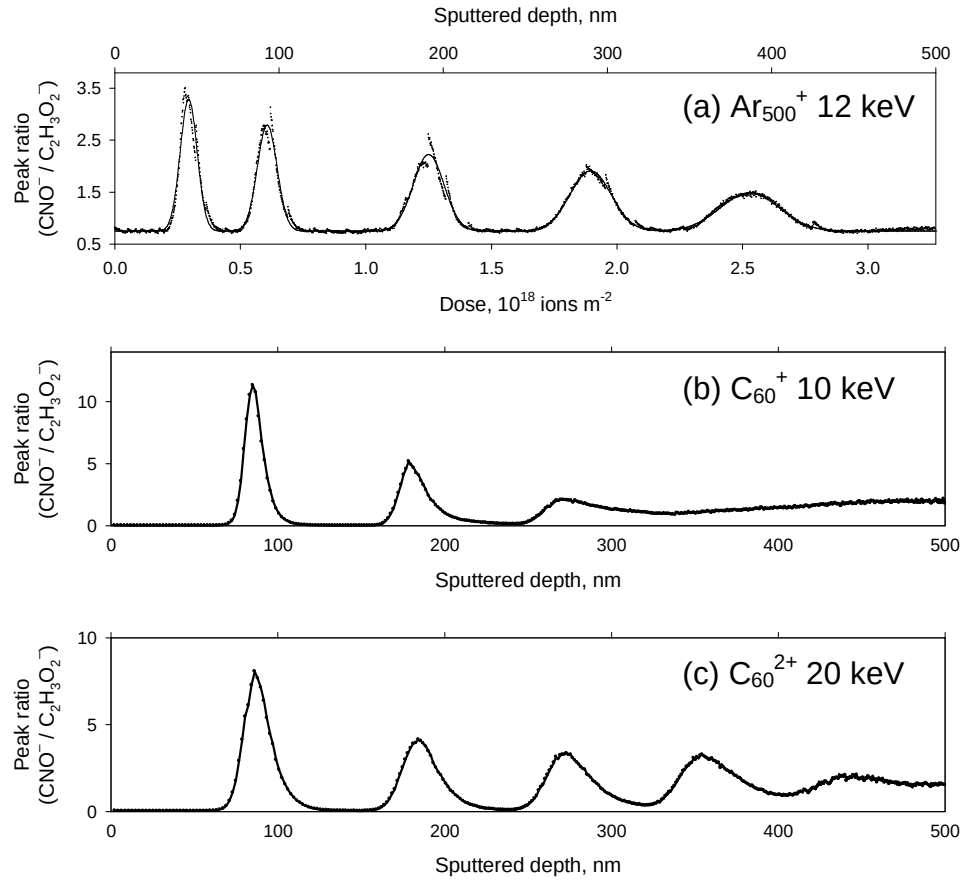

Figure 8.9 Example depth profiles obtained on the Irganox delta layer reference materials using (a) Ar_{500}^+ at 12 keV (b) C_{60}^+ at 10 keV and (c) C_{60}^{2+} at 20 keV. The C_{60}^{n+} data are from a previous study[12] using reference materials with 6 layers of thin Irganox 3114 embedded between ~ 90 nm of Irganox 1010, and are replotted to show the peak ratio $CNO^- / C_2H_3O_2^-$ on the same depth scale.

small improvement can be seen as the cluster size is increased from Ar_{500}^+ to Ar_{1000}^+ at a fixed energy of 12 keV. However, the depth resolution has no clear dependence on the ion beam energy for Ar_{500}^+ clusters. This is contrary to existing data showing poorer depth resolution with higher beam energies.[11,12,14] Unfortunately, this is because the depth resolution achieved in this study largely arises from an instrumental artefact related to the ion beam raster. Using ellipsometry mapping, which has a precision of < 1 nm, the crater shape of sputtered films where the silicon substrate has not yet been reached were characterised. An example crater profile is shown in Figure 8.8b. This shows a sloping crater floor, giving rise to ~ 10% difference in the sputtered depth over the analysis area. A similar shape is observed for all

craters at all energies and depths, which probably arises from a systematic variation of the ion dose over the sputtered area caused by a non-ideal rastering system. This would cause a linear contribution to the depth resolution with the sputtered depth, which is consistent with the observation in Figure 8.8a. It is clear that the depth resolution currently obtained is severely limited by crater uniformity in the prototype instrument. In further developments of the instrumentation, it will be important to improve the crater shapes, as this is expected to offer significantly improved depth resolution than currently obtained in this study.

8.3.4 Surface roughness

We can further characterise the potential best depth resolution achievable with Ar cluster primary ions, using AFM measurements of the sputter-induced topography. If the depth resolution was dominated by the development of topography, then the standard deviation of the response function σ obtained in SIMS would be equal to the root-mean-square roughness R_q obtained from AFM.[12,49] AFM measurements were obtained on pure Irganox 1010 layers sputtered to a range of depths (35 to 420 nm) using a range of Ar cluster sizes (Ar_{500}^+ to Ar_{1000}^+) and energies (5.5 to 17 keV). Care must be taken in measuring the surface roughness at this scale for a soft material, for example, Irganox 1010 films are known to undergo gradual surface relaxation.[49] However, previously we have shown that for Irganox materials, the R_q values measured within several hours of sputtering do show remarkable agreement with σ,[12,49] indicating the validity of this method. Example AFM images are shown in Figure 8.10, with comparison to C_{60}^+ results from Reference 49. The AFM results show very low sputter-induced roughness R_q of < 5 nm for all Ar cluster sizes and energies, with typical values of 1 – 2 nm, while the roughness of unsputtered films is around 0.3 nm. A general increase in R_q is observed for increasing sputtered depth, increasing beam energy and decreasing cluster size. These values are significantly better than C_{60}^{n+} sputtering, for example a roughness of 1.6 nm is obtained with Ar_{500}^+ compared to 10 nm with C_{60}^{n+} after sputtering to a depth of ~ 180 nm at ~ 10 keV (Figure 8.10).[49] These preliminary results agree with the low surface roughness measured on polystyrene after Ar cluster sputtering,[29] and are in the order of the lower limit imposed by the finite crater size upon cluster ion impact of organic materials.

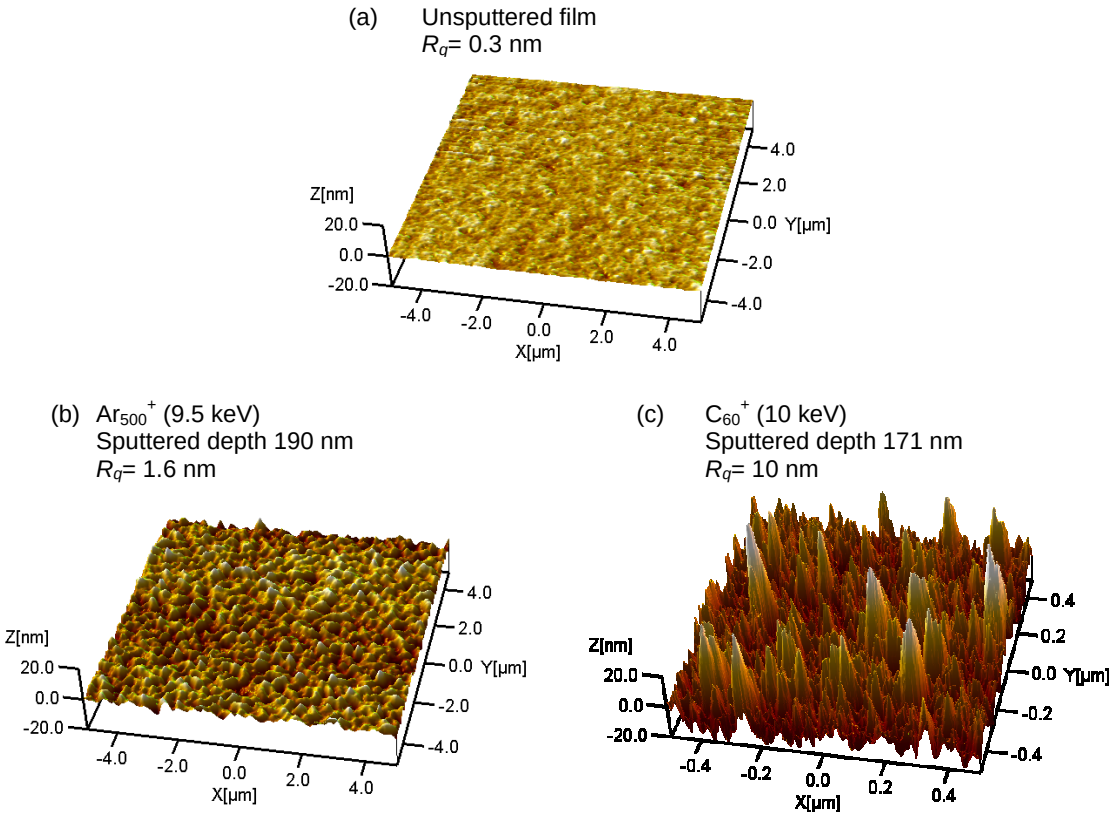

Figure 8.10 Example AFM images obtained on Irganox 1010 films after bombardment by Ar_{500}^+ and C_{60}^+, showing the sputter induced surface roughness. The data for C_{60}^+ is redrawn from Reference 49. For optimal comparison, the same height scale is used for all images. (a) The unsputtered surface has an initial roughness of R_q = 0.3 nm. (b) Using Ar_{500}^+ at 9.5 keV, the roughness has increased to R_q = 1.6 nm after sputtering to a depth of 190 nm. (c) Using C_{60}^+ at 10 keV, the roughness has increased to R_q = 10 nm after sputtering to a depth of 171 nm.

According to MD simulations the crater size is around 10 nm,[32,50] which for a single hemispherical crater give rise to an R_q of ~ 2.5 nm. The above results are very promising and indicate the very high depth resolution that may be achievable using Ar cluster ion depth profiling. It is interesting to note that Ar cluster ion beams have been widely studied for nanoscale surface smoothing of a variety of inorganic surfaces, including copper and silicon,[37,39] usually at normal incidence. Further studies are needed with improved instrumentation to clarify the mechanism of massive cluster sputtering and roughness development for a wider range of organic materials.

8.4 Conclusions

This study demonstrates the potential benefits of using novel argon cluster ion beam Ar_{500}^+ to Ar_{1000}^+ in the depth profiling of organic materials, using a well-characterised Irganox delta layer reference material. Although more work is required before widespread and general conclusions can be drawn, it is shown that, for the reference material investigated here, high sputter yields are obtained (up to 250 nm^3 per cluster ion) which are constant over a large sputtered depth scale of 390 nm. This is of practical importance and also implies very low accumulated chemical damage. The potential depth resolution achievable is thought to be limited by the development of surface topography during sputtering, which is of the order of R_q = 5 nm even after prolonged sputtering. These results are significantly better than the performance of C_{60}^{n+} reported previously for this material under identical analysis conditions. These results are highly comparable with the best currently achievable with organic depth profiling, which was demonstrated in the recent VAMAS interlaboratory study.[17,18,36] This shows that by employing special experimental conditions such as sample rotation, sample cooling and grazing incidence angle, the performance of C_{60}^{n+} depth profiling can be significantly improved to give a constant sputtering yield and good depth resolution (around 10 – 15 nm) throughout a sputtered depth of 300 nm. The results using Ar cluster ions agree with the conclusion in the VAMAS study that sample roughening is related to a decline in the sputtering yield.[18] It is likely that sample rotation, sample cooling and grazing incidence angle will also prove advantageous for Ar cluster ions. The use of Ar clusters provides a promising route for the development of organic depth profiling alongside these existing efforts using C_{60}^{n+}, and it is important that further fundamental and experimental studies on a wider range of samples are carried out alongside developments of the ion source and instrumentation, in order to fully realise the potential of this emerging technology.

References

1 A. V. Walker, Analytical Chemistry **80,** 8865 (2008).

2 C. M. Mahoney and A. J. Fahey, Analytical Chemistry **80,** 624 (2008).

3 D. Breitenstein, C. E. Rommel, R. Mollers, J. Wegener, and B. Hagenhoff, Angewandte Chemie-International Edition **46,** 5332 (2007).

4 P. Malmberg, C. Kriegeskotte, H. F. Arlinghaus, B. Hagenhoff, J. Holmgren, M. Nilsson, and H. Nygren, Applied Surface Science **255,** 926 (2008).

5 X. A. Conlan, I. S. Gilmore, A. Henderson, N. P. Lockyer, and J. C. Vickerman, Applied Surface Science **252,** 6562 (2006).

6 F. Kollmer, Applied Surface Science **231,** 153 (2004).

7 A. Delcorte, Applied Surface Science **255,** 954 (2008).

8 J. S. Fletcher, X. A. Conlan, N. P. Lockyer, and J. C. Vickerman, Applied Surface Science **252,** 6513 (2006).

9 A. G. Shard, P. J. Brewer, F. M. Green, and I. S. Gilmore, Surface and Interface Analysis **39,** 294 (2007).

10 R. Mollers, N. Tuccitto, V. Torrisi, E. Niehuis, and A. Licciardello, Applied Surface Science **252,** 6509 (2006).

11 A. Wucher, J. Cheng, and N. Winograd, Journal of Physical Chemistry C **112,** 16550 (2008).

12 A. G. Shard, F. M. Green, P. J. Brewer, M. P. Seah, and I. S. Gilmore, Journal of Physical Chemistry B **112,** 2596 (2008).

13 N. Nieuwjaer, C. Poleunis, A. Delcorte, and P. Bertrand, Surface and Interface Analysis **41,** 6 (2009).

14 L. L. Zheng, A. Wucher, and N. Winograd, Analytical Chemistry **80,** 7363 (2008).

15 G. Gillen, J. Batteas, C. A. Michaels, P. Chi, J. Small, E. Windsor, A. Fahey, J. Verkouteren, and K. J. Kim, Applied Surface Science **252,** 6521 (2006).

16 J. L. S. Lee, M. P. Seah, and I. S. Gilmore, Applied Surface Science **255,** 934 (2008).

17 A. G. Shard, R. Foster, I. S. Gilmore, J. L. S. Lee, S. Ray, and L. Yang, Surface and Interface Analysis **43,** 510 (2011).

18 P. Sjovall, D. Rading, S. Ray, L. Yang, and A. G. Shard, Journal of Physical Chemistry B **114,** 769 (2010).

19 J. Kozole, A. Wucher, and N. Winograd, Analytical Chemistry **80,** 5293 (2008).

20 G. X. Biddulph, A. M. Piwowar, J. S. Fletcher, N. P. Lockyer, and J. C. Vickerman, Analytical Chemistry **79,** 7259 (2007).

21 Y. Fujiwara, K. Kondou, Y. Teranishi, K. Watanabe, H. Nonaka, N. Saito, H. Itoh, T. Fujimoto, A. Kurokawa, S. Ichimura, and M. Tomita, Applied Surface Science **255,** 916 (2008).

22 C. Guillermier, S. Della Negra, R. D. Rickman, V. Pinnick, and E. A. Schweikert, Applied Surface Science **252,** 6529 (2006).

23 J. Matsuo, S. Ninomiya, Y. Nakata, Y. Honda, K. Ichiki, T. Seki, and T. Aoki, Applied Surface Science **255,** 1235 (2008).

24 N. Winograd, Z. Postawa, J. Cheng, C. Szakal, J. Kozole, and B. J. Garrison, Applied Surface Science **252,** 6836 (2006).

25 H. G. Cramer, T. Grehl, F. Kollmer, R. Moellers, E. Niehuis, and D. Rading, Applied Surface Science **255,** 966 (2008).

26 Extended discussion in the 44th IUVSTA Workshop on "Sputtering and Ion Emission by Cluster Ion Beams", Edinburgh, Scotland, 2007.

27 S. Ninomiya, Y. Nakata, Y. Honda, K. Ichiki, T. Seki, T. Aoki, and J. Matsuo, Applied Surface Science **255,** 1588 (2008).

28 K. Ichiki, S. Ninomiya, Y. Nakata, Y. Honda, T. Seki, T. Aoki, and J. Matsuo, Applied Surface Science **255,** 1148 (2008).

29 S. Ninomiya, K. Ichiki, H. Yamada, Y. Nakata, T. Seki, T. Aoki, and J. Matsuo, Rapid Communications in Mass Spectrometry **23,** 1601 (2009).

30 S. Ninomiya, K. Ichiki, H. Yamada, Y. Nakata, T. Seki, T. Aoki, and J. Matsuo, Rapid Communications in Mass Spectrometry **23,** 3264 (2009).

31 W. Eckstein, C. Garciarosales, J. Roth, and J. Laszlo, Nuclear Instruments & Methods in Physics Research Section B-Beam Interactions with Materials and Atoms **83,** 95 (1993).

32 A. Delcorte, B. J. Garrison, and K. Hamraoui, Analytical Chemistry **81,** 6676 (2009).

33 R. P. Webb and M. Ponomarev, Nuclear Instruments & Methods in Physics Research Section B-Beam Interactions with Materials and Atoms **255,** 229 (2007).

34 L. Rzeznik, B. Czerwinski, B. J. Garrison, N. Winograd, and Z. Postawa, Journal of Physical Chemistry C **112,** 521 (2008).

35 T. Aoki, T. Seki, S. Ninomiya, K. Ichiki, and J. Matsuo, Nuclear Instruments & Methods in Physics Research Section B-Beam Interactions with Materials and Atoms **267,** 1424 (2009).

36 A. G. Shard, S. Ray, M. P. Seah, and L. Yang, Surface and Interface Analysis **43,** 1240 (2011).

37 I. Yamada, J. Matsuo, N. Toyoda, and A. Kirkpatrick, Materials Science & Engineering R-Reports **34,** 231 (2001).

38 A. Kirkpatrick, Nuclear Instruments & Methods in Physics Research Section B-Beam Interactions with Materials and Atoms **206,** 830 (2003).

39 N. Toyoda and I. Yamada, Ieee Transactions on Plasma Science **36,** 1471 (2008).

40 S. Ninomiya, Y. Nakata, K. Ichiki, T. Seki, T. Aoki, and J. Matsuo, Nuclear Instruments & Methods in Physics Research Section B-Beam Interactions with Materials and Atoms **256,** 493 (2007).

41 T. Seki, T. Murase, and J. Matsuo, Nuclear Instruments & Methods in Physics Research Section B-Beam Interactions with Materials and Atoms **242,** 179 (2006).

42 T. Seki, J. Matsuo, G. H. Takaoka, and I. Yamada, Nuclear Instruments & Methods in Physics Research Section B-Beam Interactions with Materials and Atoms **206,** 902 (2003).

43 I. S. Gilmore and M. P. Seah, Surface and Interface Analysis **23,** 248 (1995).

44 K. Moritani, M. Hashinokuchi, J. Nakagawa, T. Kashiwagi, N. Toyoda, and K. Mochiji, Applied Surface Science **255,** 948 (2008).

45 I. S. Gilmore and M. P. Seah, International Journal of Mass Spectrometry **202,** 217 (2000).

46 J. Matsuo, S. Ninomiya, Y. Nakata, K. Ichiki, T. Aoki, and T. Seki, Nuclear Instruments & Methods in Physics Research Section B-Beam Interactions with Materials and Atoms **257,** 627 (2007).

47 K. Moritani, S. Houzumi, K. Takeshima, N. Toyoda, and K. Mochiji, Journal of Physical Chemistry C **112,** 11357 (2008).

48 K. Nakamura, S. Houzumi, N. Toyoda, K. Mochiji, T. Mitamura, and I. Yamada, Nuclear Instruments & Methods in Physics Research Section B-Beam Interactions with Materials and Atoms **261,** 660 (2007).

49 F. M. Green, A. G. Shard, I. S. Gilmore, and M. P. Seah, Analytical Chemistry **81,** 75 (2009).

50 B. J. Garrison and Z. Postawa, Mass Spectrometry Reviews **27,** 289 (2008).

Chapter 9 – Conclusions and suggestions for future work

The studies described in this thesis contribute towards the goal of tackling the growing measurement requirements of surfaces and interfaces in industry, by resolving three key challenges that are often encountered in the practical analysis of such samples using ToF-SIMS.

This work successfully identified a number of topographic field effects in ToF-SIMS and evaluated several promising approaches for their reduction, from optimising available instrumental parameters to alterative sample mounting methods. This is shown to be extremely beneficial in extending the measurement capabilities of ToF-SIMS. Inevitably, not all topographic effects can be eliminated, and the challenge remains for many real-life samples where alternative mounting is not feasible. It is clear that the development of ToF-SIMS analysers has lagged behind other developments such as high performance primary ion beams and growing industrial applications. Improved instrument and mass spectrometer designs for topographic samples are absolutely crucial to enable the application of ToF-SIMS to a wider range of samples.

In dealing with the large volumes of data generated by modern ToF-SIMS instruments, multivariate methods have been demonstrated to be successful in extracting relevant chemical information with minimal analyst input. The main challenge is in the interpretation of the multivariate results and this requires extensive understanding of both the multivariate methods as well as the nature of ToF-SIMS data. The studies here provide guidance and clear examples on a number of important aspects including the choice of method, data preprocessing and interpretation of results. However, for multivariate methods to be a widespread tool for ToF-SIMS analyses, a number of issues, both fundamental and practical, will need resolution. Multivariate methods need to be made more robust to instrumental influences such as the non-linear nature of ToF-SIMS data, whilst more efficient algorithms are urgently needed due to the significant computer memory constraints which do not allow the whole raw data set to be analysed without significant binning and peak selection. The

development of advanced informatics methods for complex mass spectra, which utilise recent progress in the exploding field of –omics (e.g. proteomics and metabolomics), would also bring considerable benefits to the ToF-SIMS community.

Finally, the preliminary study on organic depth profiling using argon cluster ions has helped launch the acceptance of the technology, which is now widely recognised as the way forward as attested by a number of instrument manufacturers developing commercial argon cluster guns. Data from these new instruments strongly support the conclusion that argon clusters give superior results to C_{60}. Further research is essential to develop the metrology and applications, including to elucidate the mechanism of sputtering, evaluate a wider range of organic materials, characterise the extent of damage and the ultimate depth resolution achievable, explore their application for low fragmentation surface mass spectrometry and investigate the use of argon clusters in combination with other improvements such as sample rotation, cooling and nitric oxide radical scavenging to achieve the best performance. With these developments, argon cluster ions have the exciting unique promise of 3D chemical imaging for organic materials with nanometre resolution, which will revolutionise product innovation and research for many industries.